COPPE
Instituto Alberto Luiz Coimbra de Pós-Graduação e Pesquisa de Engenharia
UFRJ

A STUDY ON GREEN WATER PROBLEM WITH DAM BREAK MODEL AND THE BIV TECHNIQUE

Qingfeng Duan

Tese de Doutorado apresentada ao Programa de Pós-graduação em Engenharia Oceânica, COPPE, da Universidade Federal do Rio de Janeiro, como parte dos requisitos necessários à obtenção do título de Doutor em Engenharia Oceânica.

Orientador: Sergio Hamilton Sphaier

Rio de Janeiro
Abril de 2017

A STUDY ON GREEN WATER PROBLEM WITH DAM BREAK MODEL AND THE BIV TECHNIQUE

Qingfeng Duan

TESE SUBMETIDA AO CORPO DOCENTE DO INSTITUTO ALBERTO LUIZ COIMBRA DE PÓS-GRADUAÇÃO E PESQUISA DE ENGENHARIA (COPPE) DA UNIVERSIDADE FEDERAL DO RIO DE JANEIRO COMO PARTE DOS REQUISITOS NECESSÁRIOS PARA A OBTENÇÃO DO GRAU DE DOUTOR EM CIÊNCIAS EM ENGENHARIA OCEÂNICA.

Examinada por:

Prof. Sergio Hamilton Sphaier, Dr.-Ing.

Dr. Marcelo de Araujo Vitola, D.Sc.

Prof. Paulo de Tarso Themístocles Esperança, D.Sc.

Prof. Claudio Alexis Rodriguez Castillo, D.Sc.

Prof. Su Jian, D.Sc.

Prof. Luis Fernando Alzuguir Azevedo, Ph.D.

RIO DE JANEIRO, RJ – BRASIL
ABRIL DE 2017

Duan, Qingfeng

A study on green water problem with dam break model and the BIV technique/Qingfeng Duan. – Rio de Janeiro: UFRJ/COPPE, 2017.

XVII, 136 p.: il.; 29, 7cm.

Orientador: Sergio Hamilton Sphaier

Tese (doutorado) – UFRJ/COPPE/Programa de Engenharia Oceânica, 2017.

Bibliografia: p. 111 – 119.

1. Green water. 2. Dam break. 3. BIV. I. Sphaier, Sergio Hamilton. II. Universidade Federal do Rio de Janeiro, COPPE, Programa de Engenharia Oceânica. III. Título.

To my dear family, who always
picked me up and encourage me
to go on every adventure,
especially this one.

Acknowledgement

Firstly, I would like to express my sincere gratitude to my advisor Prof. Sergio Hamilton Sphaier for the continuous support of my Ph.D. study and research, for his patience, motivation, and enthusiasm.

I would also like to express my special appreciation and thanks to Prof. Marcelo de Araujo Vitola for his precious critical comments in many aspects of my research. The door to his office was always open whenever I ran into a trouble spot or had a question about my research.

Many thanks to Prof. Paulo de Tarso T. Esperança and to the fellow mates in LabOceano: Jassiel Hernandez, Fabio Quintana, Alex Alves and all others. Very grateful for all the help in the experiment.

Special thanks to all my friends, especially for Dr. Guang Ming Fu and Prof. Su Jian. Thank you for listening, offering me advice, and supporting me through this entire process. It is all of you colored my life in Rio de Janeiro.

My thanks also go to the administrative staff in PENO for all the help during my Ph.D.

I also take this opportunity to record my sincere gratitude to one and all who, directly or indirectly, have lent their helping hands in this adventure.

Besides, financial supports from the China Scholarship Council (CSC), the Brazilian National Council for the Improvement of Higher Education (CAPES) and the Brazilian National Council for Scientific and Technological Development (CNPq) are gratefully acknowledged.

Resumo da Tese apresentada à COPPE/UFRJ como parte dos requisitos necessários para a obtenção do grau de Doutor em Ciências (D.Sc.)

UM ESTUDO SOBRE O PROBLEMA DA ÁGUA VERDE COM MODELO DE QUEBRA DE BARRAGEM E A TÉCNICA BIV

Qingfeng Duan

Abril/2017

Orientador: Sergio Hamilton Sphaier

Programa: Engenharia Oceânica

A água verde gerada por ondas extremas é principalmente uma mistura ar-água, que inclui uma fase contínua e uma fase dispersa.

A fase contínua é estudado principalmente com o modelo de quebra de barragem (QB) por três abordagens principais, a saber analítica, experimental e numérica. Analiticamente, as duas soluções de Stoker são introduzidas para estudar a onda de QB em um canal horizontal seco. Nas fases iniciais, o conceito de "ruptura repentina de barragens" é revisto. A barragem pode ser considerada quebra repentinamente quando o perodo de remoção adimensional é menor que $\frac{3t_1^*}{5} \approx 0.63$. Para incluírem os efeitos de atrito e de inclinação de fundo, propusemos uma solução fragmentada simplificada (PS). Numericamente, o modelo de dois fluidos com o método Volume of Fluid (VOF) implementado no solver interFoam é usado para simular a onda de QB. O solucionador interFoam resolve as equações de RANS com um modelo de turbulência $k-\varepsilon$. Experimentalmente, diferentes casos de são realizadas incluindo um leito horizontal e quatro leito como diferentes ângulo de inclinação (ascendente 10° e 5°, descendente 10° e 5°). Ao introduzir um fator de compensação de tempo $t_c^* = \frac{t_1^*}{3}$ em PS, a onda de downstream prevista concorda bem com os dados experimentais e os resultados numéricos.

Na fase dispersa, os casos presentes aplicaram principalmente a técnica BIV. Para melhorar a compreensão da técnica BIV, são consideradas as propriedades especiais das bolhas e é realizado um experimento BIV de teste para avaliar a capacidade do sistema BIV. Finalmente, a técnica é aplicada no experimento de ruptura da barragem.

Abstract of Thesis presented to COPPE/UFRJ as a partial fulfillment of the requirements for the degree of Doctor of Science (D.Sc.)

A STUDY ON GREEN WATER PROBLEM WITH DAM BREAK MODEL AND THE BIV TECHNIQUE

Qingfeng Duan

April/2017

Advisor: Sergio Hamilton Sphaier

Department: Ocean Engineering

The green water generated by extreme waves is primarily an air-water mixture, which includes a continuous phase and a dispersed phase.

The continuous phase is explored with the dam break model by three main approaches, namely analytical, experimental and numerical. Analytically, both the Eulerian and Lagrangian Stoker solutions are introduced to study the dam break wave in a dry horizontal channel. The two Stoker solutions have an intersection point at the dam section at instant $t_1^* = \frac{\sqrt{10}}{3}$. In the initial stages, the "sudden dam break" concept is revised. The dam may be considered break suddenly when the dimensionless gate removal period is smaller than $\frac{3t_1^*}{5} \approx 0.63$. To include the bottom friction effects and the bed slope effects for green water problem, we proposed a simplified piecewise solution (PS). Numerically, the two fluid model with the Volume of Fluid (VOF) method implemented in the interFoam solver is used to simulate the dam break wave. The interFoam solves the RANS equations with a $k - \varepsilon$ turbulence model. Experimentally, different dam break cases are carried out including one horizontal bed and four different downstream slope beds (upward 10° and 5°, downward 10° and 5°). Each bed is tested with two different water levels (110 mm and 220 mm). By introducing a time compensation factor $t_c^* = \frac{t_1^*}{3}$ into PS, the predicted downstream wave agree well with the experimental data and numerical results.

In the dispersed phase, the present study mainly focus on the BIV technique. The special properties of bubbles are taken into consideration and a test BIV experiment is carried out to evaluate the BIV system capacity. Finally, the BIV technique is applied to the dam break experiment.

Contents

List of Figures **xi**

List of Tables **xv**

1 Introduction **1**
1.1 Research objectives . . . 3
1.2 Outline of the thesis . . . 5

2 Literature review **7**
2.1 The green water phenomenon . . . 7
2.1.1 Scenarios of green water . . . 8
2.1.2 Green water impact on structures . . . 9
2.1.3 Green water loading on deck . . . 11
2.2 The BIV technique . . . 11
2.2.1 General Description of PIV . . . 12
2.2.2 Consideration for PIV in bubbly flow . . . 15
2.2.3 General description of BIV technique . . . 17

3 Analytical Dam Break Solutions **19**
3.1 Stoker solutions . . . 19
3.1.1 Eulerian Stoker solution . . . 19
3.1.2 Lagrangian Stoker solution . . . 20
3.2 Eulerian Stoker solution extensions . . . 24
3.2.1 Bottom friction effects . . . 24
3.2.2 Dam break wave in a sloping channel . . . 26
3.3 A piecewise solution . . . 28
3.3.1 Solution with a compensated time factor . . . 29

4 Numerical Dam Break Model **31**
4.1 Overview of OpenFOAM . . . 31
4.2 interFoam solver . . . 32
4.2.1 RANS equations . . . 32

4.2.2 Modified VOF method . . . 35
4.2.3 Discretised model equations . . . 36
4.2.4 Pressure-velocity coupling . . . 38
4.3 Validation of the solver . . . 40
4.3.1 Grid convergence . . . 43

5 Dam Break Experiments 45
5.1 Experiment setup . . . 45
5.2 Tank and gate release system . . . 46
5.3 Data acquisition and synchronization . . . 47
5.3.1 Wave probes . . . 48
5.3.2 Pressure sensor . . . 49
5.3.3 Temperature sensors . . . 51
5.3.4 Accelerometer . . . 51
5.3.5 Video recording and illumination . . . 51
5.4 Test cases . . . 52

6 Results of Dam Break Models 54
6.1 Main period with Stoker solutions . . . 54
6.1.1 Sudden dam break . . . 59
6.2 Main period with the piecewise solution . . . 61
6.2.1 Horizontal bed cases . . . 61
6.2.2 Slope bed cases . . . 65
6.2.3 Bottom friction factor . . . 73
6.3 Pressure measurement . . . 76
6.3.1 Typical signal of pressure . . . 76
6.3.2 Numerical pressure results . . . 81
6.4 Elevations . . . 82
6.4.1 Wave probes . . . 82
6.4.2 Virtual wave probes . . . 85

7 The BIV technique and the Application 87
7.1 BIV test experiment . . . 87
7.1.1 System capacity . . . 91
7.2 Considerations on bubble/drops properties . . . 93
7.2.1 Shape regimes of the fluid particles . . . 94
7.2.2 Equation of particle motion . . . 97
7.3 Application of the BIV technique . . . 101
7.3.1 Example in the main period . . . 102
7.3.2 Example in the impact period . . . 105

7.3.3 Example in the reflection period . . . 106
7.3.4 Notes on BIV technique application . . . 106

8 Conclusions and Future Work 108
8.1 Conclusions . . . 108
8.1.1 Continuous phase . . . 108
8.1.2 Dispersed phase . . . 109
8.2 Future works . . . 110

Bibliography 111

A Shallow Water Equations 120
A.1 Shallow Water Equations . . . 120
A.1.1 Saint Venant Equations . . . 123
A.1.2 Method of Characteristics . . . 123

B Camera Calibration 124
B.1 camera calibration . . . 124

C Water Level Dectection 127
C.1 Algorithm for water level detection . . . 127

D Uncertainty Analysis of BIV 132
D.1 Uncertainty analysis of BIV . . . 132
D.1.1 Optimize magnification factor . . . 135

List of Figures

1.1 Green water incident of the Selkirk Settler. Photograph by Captain G. A. Ianiev. Available at: http://www.boatnerd.com/pictures/fleet/spruceglen.htm [accessed 17^{th} April 2017] 1
1.2 Main methodology 4

2.1 Scenarios of green water. Adapted from GRECO *et al.* [24] 8
2.2 Schematic green water flow over the deck 9
2.3 Results of similarity solution by ZHANG *et al.* [27], adapted from GRECO [11] 10
2.4 Typical arrangement for particle image velocimetry 12
2.5 The cross-correlation algorithms, adapted from RAFFEL *et al.* [16] . 14
2.6 Principle of the three-point Gaussian fit, adapted from THIELICKE and STAMHUIS [38] 14
2.7 PIV image around an air bubble in a thin light-sheet, adapted from BRÜCKER [39] 15
2.8 Reflection and refraction of components of an incident ray for an air bubble, adapted from DAVIS [40] 16
2.9 Sketch of a combination of the shadowgraph with PIV, adapted from SATHE *et al.* [47] 17
2.10 Sketch of BIV arrangements, adapted from RYU *et al.* [15] 17

3.1 Dam break in Eulerian representation, adapted from STOKER [10] . 20
3.2 Dam break in Lagrangian representation, adapted from STOKER [10] 21
3.3 The Whitham solution 24
3.4 Sketch of a dam break wave in a dry downward sloping channel, adapted from CHANSON [53] 26
3.5 Sketch of a dam break wave in a dry upward sloping channel, adapted from CHANSON [19] 27
3.6 Sketch of a horizontal dam with different sloping bed 28
3.7 Example of transformation for $\theta = 10$ and $f = 0.1$ at instant $t^* = 0.667$ 29

4.1 Discretization of the solution domain, adapted from GREEN-SHIELDS [63] . . . 37
4.2 Schematic of dam break model,in units: mm, adapted from LOBOVSKỲ *et al.* [32] . . . 41
4.3 Results of pressure comparing to experimental data . . . 43

5.1 Experimental setup, overall view . . . 45
5.2 Experimental setup of the dam-break tests . . . 46
5.3 Schematic view of the gate release system . . . 47
5.4 Data acquisition Flow . . . 47
5.5 Downsteam turbulence . . . 49
5.6 Wave probes and virtual wave probes . . . 49
5.7 Sketch of the slope bed blocks . . . 53

6.1 H=110 mm, evaluation of free surface profile . . . 55
6.2 OpenFOAM free surface profile . . . 56
6.3 Sketch of the initial stage of the dam break problem with top particle P_1 and bottom particle P_2 at the dam gate section . . . 57
6.4 H=300 mm, evaluation of free surface profile, adapted from from LOBOVSKỲ *et al.* [32] . . . 59
6.5 Results of the two higher level cases at instant t_g . . . 60
6.6 Example results of the piecewise solution in horizontal channel . . . 61
6.7 H=110 mm, results of the PS with compensated time $t_c^* = \frac{t_1^*}{3}$, and with bottom friction factor $f = 0.04$ . . . 62
6.8 H=220 mm, results of the PS with compensated time $t_c^* = \frac{t_1^*}{3}$, and with bottom friction factor $f = 0.12$ . . . 63
6.9 H=600 mm, adapted from LOBOVSKỲ *et al.* [32], results of the PS with compensated time $t_c^* = \frac{t_1^*}{3}$, and with bottom friction factor $f = 0.16$ . . . 64
6.10 H=110 mm, evaluation of free surface profile for downward slope angle 10 degree, with $t_c^* = \frac{t_1^*}{3}$ and with $f = 0.04$ . . . 66
6.11 H=220 mm, evaluation of free surface profile for downward slope angle 10 degree, with $t_c^* = \frac{t_1^*}{3}$ and with $f = 0.12$ . . . 67
6.12 H=110 mm, evaluation of free surface profile for downward slope angle 5 degree, with $t_c^* = \frac{t_1^*}{3}$ and with $f = 0.04$ . . . 68
6.13 H=220 mm, evaluation of free surface profile for downward slope angle 5 degree, with $t_c^* = \frac{t_1^*}{3}$ and with $f = 0.12$ . . . 69
6.14 H=110 mm, evaluation of free surface profile for downward slope angle 10 degree, with $t_c^* = \frac{t_1^*}{3}$ and with $f = 0.04$ . . . 70

6.15 H=220 mm, evaluation of free surface profile for upward slope angle 10 degree, with $t_c^* = \frac{t_1^*}{3}$ and with $f = 0.12$ 71
6.16 H=110 mm, evaluation of free surface profile for downward slope angle 10 degree, with $t_c^* = \frac{t_1^*}{3}$ and with $f = 0.04$ 72
6.17 H=220 mm, evaluation of free surface profile for downward slope angle 10 degree, with $t_c^* = \frac{t_1^*}{3}$ and with $f = 0.12$ 73
6.18 A typical signal of pressure sensors and the zoomed pressure peaks . . 76
6.19 Small peaks before impact related to the gate releasing 77
6.20 Pitch motion test with 6 DOF platform 77
6.21 Pitch motion test in different periods, the amplitude of the pitch angle is 10 degree 78
6.22 Pressure peaks in ten times repetitions for horizontal bed case H = 110 mm 80
6.23 Simulated pressure for $H = 220$ mm 81
6.24 Simulated pressure for $H = 110$ mm 82
6.25 Elevation time history of wave probe h7 and h8 for horizontal bed case $H = 110$ mm, in 10 repetitions 82
6.26 Elevation time history at wave probe location h7 and h8 for horizontal bed 83
6.27 Elevation time history at wave probe location h7 and h8 84
6.28 Elevation of virtual wave probe h5 85
6.29 Water Level Dectection of h5 (the blue one) at time 120 ms (left) and 132 ms (right) 85
6.30 Elevation of virtual wave probe h3 (left) and the corresponded areated peak at time 224 ms (right) 86
6.31 Elevation of virtual wave probe h1 (left) and the corresponded small areated front at time 212 ms (right) 86

7.1 Schematic of the BIV test experiment 87
7.2 An example image and bubble identify process 89
7.3 Workflow of PIVlab, adapted from THIELICKE and STAMHUIS [38] 90
7.4 An example of the output velocity fields 91
7.5 Results for the test experiment 93
7.6 Shape regimes for bubbles and drops, adapted from CLIFT *et al.* [81] 94
7.7 Bond number versus bubbles or drops diameter 96
7.8 Terminal Reynolds number versus bubbles or drops diameter 97
7.9 Velocity amplitude response versus Stokes number 100
7.10 H=110 mm, BIV analysis velocity vectors in time 12, 20, 28, 36, 44, 52 ms 102

7.11 Gate releasing velocity in time history obtained with BIV 103
7.12 BIV results example during the runup 103
7.13 Wave front velocity time evolution 104
7.14 BIV results example during the runup 106
7.15 BIV results example of the reflection wave 106

A.1 A Typical Water Column 121

B.1 camera calibration image example 124
B.2 camera calibration mean error 125
B.3 camera calibration mean error 125

C.1 Original 128
C.2 Edge dectected with Sobel method 128
C.3 Edge thickness dilated 129
C.4 Hough transform for straight lines 129
C.5 Hough transform peaks 130
C.6 Dectected top three longest line 130
C.7 Calculate the detected water level 131

List of Tables

3.1 Summary of the piecewise solution 29

4.1 The discretization schemes of interFoam 42
4.2 Order of accuracy and Grid Convergence Index for three integration variables. Subscripts 3, 2 and 1 represent case $DS = 20, 10, 5$ mm, respectively. 44

5.1 Specifications of EPX sensor 50
5.2 Camera properties 52
5.3 Slope bed blocks and test cases 53

6.1 The average gate releasing velocity and the gate removal period . . . 60
6.2 Summary of the different bed slope bed cases 65
6.3 Bottom friction factor calculation with Approach A 74
6.4 Bottom friction factor calculation with Approach B 75

7.1 Summary of BIV test experiment 90
7.2 Analytical approaches of front velocity with bottom friction effects . . 104
7.3 The average dimensionless wave front velocity for time $t > t_1^*$ 105

D.1 Evaluate the uncertainty on α 133
D.2 Evaluate the uncertainty on image displacement ΔX 134
D.3 Evaluate the uncertainty on δu 134
D.4 Evaluate the uncertainty on Δt 135
D.5 Evaluate the uncertainty on u 135

Nomenclature

Abbreviations

2D Two Dimensional

3D Three Dimensional

BIV Bubble Image Velocimetry

DCC Direct Cross Correlation

DFT Discrete Fourier Transform

DOF Depth of Field

DSR Dynamic Spatial Range

DVR Dynamic Velocity Range

ESS Eulerian Stoker Solution

FFT Fast Fourier Transform

FOV Field of View

LHS Left Hand Side

LSS Lagrangian Stoker Solution

OpenFOAM Open Field Operation And Manipulation

PIV Particle Image Velocimetry

RANS Reynolds Averaged NavierStokes

RHS Right Hand Side

VOF Volume of Fluid

Symbols

α	Water volume fraction
κ	Kinematic viscosity
μ	Dynamic viscosity
μ^{eff}	Effective dynamic viscosity
ν	Kinematic viscosity
ρ	Density
θ	Angle
Bo	Bond number
d_p	Particle diameter
f	Bottom friction factor
g	Gravitational constant
H	Initial water level in dam
h	Local water depth
Mo	Morton number
Re	Reynolds number
Re_T	Reynolds number in terminal velocity
S_t	Stokes number
t	Time
t_1	Time for ESS and LSS has an intersection point at dam section
t_c	Time compensation factor
t_g	Time at gate releasing distance equals to H
U	Dam break wave front Velocity
u	Horizontal velocity component
U_T	Terminal velocity
v	Horizontal velocity component
x	Horizontal axis
y	Vertical axis

Chapter 1

Introduction

Interactions between extreme waves and offshore structures are of primary interest to ocean engineers. In rough sea conditions, when the relative motion between the ship deck and the local water surface becomes so excessive that the incoming wave can overcome the freeboard and flow onto the deck of a ship. This problem is known as “shipping of water”, “deck wetness” or “green water”.

(a) Before incident (b) During incident

Figure 1.1: Green water incident of the Selkirk Settler. Photograph by Captain G. A. Ianiev. Available at: http://www.boatnerd.com/pictures/fleet/spruceglen.htm [accessed 17^{th} April 2017]

Green water has been considered to be a major issue with regards to safety and operability of offshore structures for a long time. SCHØNBERG and RAINEY [1] reported a green water accident for the Selkirk Settler in the mid Atlantic in February 1987, as shown in Fig. 1.1, the upper deck is being swamped by a huge wave crest. That same storm sank two ships and severely damaged three others.

In the oil and gas industry, as the demand for fossil fuel is increasing, oil production has moved into the deep water. A common deep water facility is the floating production storage and offloading (FPSO) vessel. FPSO units are the ship-type structure, often permanently moored to the seabed. They remain at their position

during a storm and their decks carry a lot of sensitive equipment, which is at the risk of possible damage due to the shipping of water on deck. One example of a critical green water event of the Norwegian FPSO, Petrojarl Varg, was reported by ERSDAL *et al.* [2] in January 2000. The living quarters were hit by green water and resulted in the damage of a window at the second floor. LEONHARDSEN *et al.* [3] reported two green water incidents in the North Sea which forced the shutdown of production and damaged safety equipment. MORRIS *et al.* [4] reported that, from year 1995 to year 2000, 17 green water incidents were identified on 12 UK FPSO units and caused different level of damage. Due to its importance in oil production, the interests on the green water problem are growing.

Green water generated by extreme waves is primarily an air-water mixture, as can be observed in Fig. 1.1b. It includes a continuous phase and a dispersed phase.

In the continuous phase, since the resemblance between the dam break model and the green water phenomenon was reported by GODA *et al.* [5], the dam break model has become the most popular approach for representing the shipping of water on deck, e.g. BUCHNER [6], GRECO *et al.* [7], SCHØNBERG and RAINEY [1], RYU *et al.* [8], PHAM [9]. The standard approach for solving the dam break problem is the so-called "Stoker solution" (STOKER [10]).

The "Stoker solution" is a simplified solution, which restricts to a horizontal bed case without bottom friction. However, during a green water incident, the pitch angle of ship deck varies due to the incoming wave. According to BUCHNER [6] and GRECO [11], the green water impact on structures are determined by the flow velocity and its propagating wave front shape, where the bottom friction taking place. The "Stoker solution" do not take this two aspects into consideration and thus there is a calling on extending the solution to include the two aspects.

The initial stage of the dam break model is another interesting topic. Unlike its application for hydraulics researchers usually with a long open channel, in shipping of water, the deck of the ship is relatively short. The limited deck length makes the initial stage of the dam break model more relevant. In the initial stage, there is a discontinuity in the "Stoker solution", the wave front velocity jumps from zero to $2\sqrt{gH}$ at $t = 0^+$, where g is the gravity acceleration and H is the initial water level within the dam. This indicates that the "Stoker solution" is not a good approximation for dam break wave in the initial stage. To the best of our knowledge, despite a few studies, e.g. STANSBY *et al.* [12], BUKREEV and GUSEV [13] and OERTEL and BUNG [14], the initial stage has not been well investigated yet.

On the other hand, the dispersed phase of the shipping of water has rarely been studied. Due to the high void fraction nature of the green water flow, the measurement on a important characteristics of flow, the velocity field, becomes very difficult. Recently, RYU *et al.* [15] introduced the so-called Bubble Image

Velocimetry (BIV) technique, based on the idea of combining the shadowgraph technique that illuminates the fluid from behind to reveal the flow pattern, and the classical Particle Image Velocimetry (PIV) technique that correlates the consecutive images to determine the velocity. In contrast to the PIV technique, no small seeding particles are added in the flow, but the bubbles itself are used as the tracer particles. Using the BIV technique, RYU *et al.* [8] succeed in measuring the velocity field of several green water cases induced by breaking waves. They concluded that the comparisons with the "Stoker solution" are surprisingly well. However, PIV is a very dedicated technique which has many special requirements on the seeding particles. Despite of the success achieved by RYU *et al.* [8] in obtaining the velocity field, a very important aspect, the different properties between bubbles and solid seeding particles, was not taken into consideration in their work. According to RAFFEL *et al.* [16], the seeding particles should be small enough to follow the flow and also be large enough to scatter sufficient light; the density of the particles should be close to the fluid; the distribution of particles should be homogeneous. Comparing to the solid seeding particles, the properties of bubbles are quite different. The density of air bubbles is only one thousandth of water; the bubbles size and its distribution depend on the flow itself, which are almost out of control; the bubbles may break-up into small ones or coalescence into a bigger one. None of these specific properties of bubbles has been considered in work by RYU *et al.* [8].

1.1 Research objectives

Based on the above observations, this thesis is aimed to improve the knowledge of the green water problem on both phases. In the continuous phase, the main objectives are:

- To extend the analytical dam break solution for green water problem by taking account the bottom friction and the bed slope effects;
- To evaluate a numerical model based on open source code OpenFOAM;
- To do dam break experiments with different slope bed and acquire necessary experimental data that can validate the analytical solution and numerical model;

In the dispersed phase, the main objectives are:

- To test the BIV technique and evaluate its system capacity;
- To evaluate the special characteristics of bubbles that differ the PIV and BIV technique;

- To acquire the dam break velocity fields in the dispersed phase using the BIV technique;

In order to achieve these goals, the main methodology are sketched in Fig. 1.2a and Fig. 1.2b respectively.

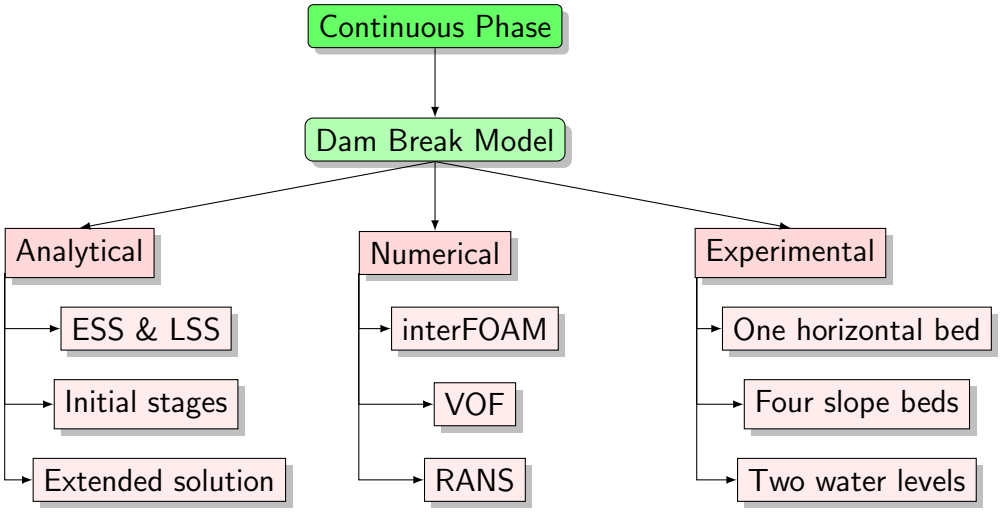

(a) Continuous phase, ESS donates Eulerian Stoker solution and LSS represents Lagrangian Stoker solution

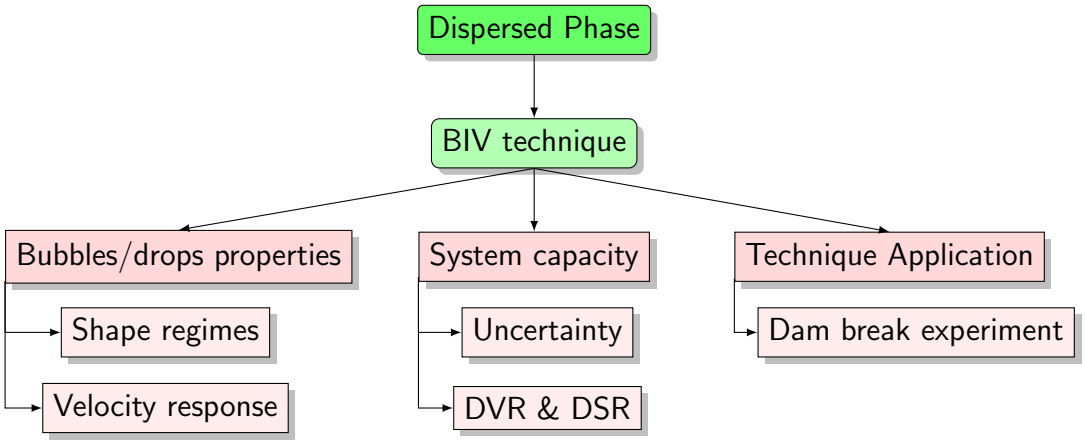

(b) Dispersed phase, DSR donates dynamic spatial range and DVR represents dynamic velocity range

Figure 1.2: Main methodology

In the continuous phase, the dam break model is applied. The dam break model is explored by three main approaches, namely analytical, experimental and numerical. Two main topics of the dam break model are explored: the initial stage and an extended solution to include bottom friction and bed slope effects. Analytically, STOKER [10] proposed two dam break solutions using Eulerian and Lagrangian representation. To distinguish the two solutions, they are called as the Eulerian Stoker solution (ESS) and the Lagrangian Stoker solution (LSS) respectively. Both Stoker solutions are introduced to studied the dam break wave in a dry horizontal channel. In the initial stages, the "sudden dam break" concept proposed by

LAUBER and HAGER [17] is also investigated. To include the bottom friction effects and the bed slope effects, a simplified piecewise solution (PS) is proposed based on the work by WHITHAM [18] and CHANSON [19]. Numerically, the two fluid model with the Volume of Fluid (VOF) method implemented in the interFoam solver is used to simulate the dam break wave. The interFoam solver solves the Reynolds-averaged Navier-Stokes equations (RANS) with a $k-\varepsilon$ turbulence model. Experimentally, different dam break cases are carried out including one horizontal bed and four different downstream bed slopes (upward 10° and 5°, downward 10° and 5°). For each bed, the experiment is run with two different water levels (a lower level 110 mm and a higher level 220 mm). The results are evaluated by comparing different approaches.

In the dispersed phase, the present study is mainly focusing on the BIV technique, which requires a good knowledge on the special characteristics of bubbles. With regarding to measurement accuracy, two main aspects of bubble characteristics are considered: the bubble dimension size and bubble density. The bubble dimension size are related with its shape regimes which are determined by three dimensionless groups: the Bond number, the Morton number and the terminal Reynolds number. The density ratio between the particles and the surrounding fluid affects the particle velocity response in the fluid. This is investigated with the particle motion equation: the Basset-Boussinesq-Oseen (BBO) equation. To test the performance of the BIV technique, a test experiment is carried out. A uncertainty analysis is done by the ITTC Recommended Procedures and Guidelines on PIV uncertainty analysis (PARK *et al.* [20]). The capacity of the BIV system, including the dynamic velocity range (DVR) and dynamic spatial range (DSR) are also explored.

1.2 Outline of the thesis

The thesis is structured as follows.

After this brief introduction, the general physics of green water phenomenon and the developments in the PIV technique and the BIV technique are reviewed in Chapter 2.

In Chapter 3, the analytical approaches for the dam break model are explored. The theoretical solutions proposed by STOKER [10] for a horizontal bed cases are given first. To include the bottom friction effects and the bed slope effects, a simplified piecewise solution (PS) is proposed based on the work by WHITHAM [18] and CHANSON [19].

In Chapter 4, the two fluid model with the Volume of Fluid (VOF) method implemented in the interFoam solver (version 2.3.0) is described in detail. The solver solves the Reynolds-averaged Navier-Stokes equations (RANS) with a $k-\varepsilon$ turbu-

lence model. The solver is also validated with previously published experimental data for a horizontal bed case.

In Chapter 5, the dam break experiments are described. Different dam break cases are carried out including one horizontal bed and four different downstream bed slopes (upward 10° and 5°, downward 10° and 5°). For each bed, the experiment is run with two different water levels (a lower level 110 mm and a higher level 220 mm).

In Chapter 6, the results are evaluated by comparing different approaches. For the horizontal bed cases, the initial stages of the dam break problem are explored. The "sudden dam break" concept proposed by Lauber and Hager is also investigated.

In Chapter 7, the BIV technique is explored. A test BIV experiment is carried out first. The uncertainty and the capacity of the BIV system are explored. The main difference with the PIV technique is that the BIV technique uses the bubbles as tracer particles. The special characteristics on bubbles are also explored by the bubble (or drops) shape regimes and velocity response in fluid. The BIV technique is then applied to the dam break experiment.

Finally, the main conclusions are remarked in Chapter 8.

Chapter 2

Literature review

Green water has been considered to be a major issue with regards to safety and operability of offshore structures for a long time. The green water generated by extreme waves is primarily an air-water mixture, which includes a continuous phase and a dispersed phase. This chapter reviews the general physics of green water phenomenon and the developments of the BIV technique for measuring the dispersed phase.

2.1 The green water phenomenon

Following BUCHNER [6], the main stages associated with the green water problem are:

- Motions and relative wave motions
- Water flow onto the deck
- Water behaviour and loading on the deck
- Green water impact on structures

The relationship between the green water phenomenon and the incoming wave is quite complicated. The complex fluid-structure interactions are still not well understood. As commented by ERSDAL *et al.* [2], it is not necessarily the greatest wave that causes maximum green water event. BUCHNER [21] and HAMOUDI and VARYANI [22] also found that there is no direct relation between the velocity of the incoming wave and the water velocity over the deck. STANSBERG *et al.* [23] pointed that green water is generally the combined effect of two mechanisms, the extreme wave events and negative pitch of the vessel. Hence, the pitch motion is very important to the green water problem. In the present work, the influence of the pitch motion is evaluated by a static pitch angle together with dam break model.

2.1.1 Scenarios of green water

GRECO *et al.* [24] suggested that the green water on deck is qualitatively associated with the scenarios given in Fig. 2.1. Based on the ratio between the incoming wave vertical velocity W_w and the vertical velocity W of water elevation at bow and in terms of incoming wave steepness, the scenarios include the follows: dam break (DB, figure a) type events characterized by flow of water along the deck similar to those generated by the breaking of dams; initial plunging plus dam break (PDB, figure b) type events, where the dam break water evolution is preceded by an initial plunging phase; plunging wave (PW, figure c) type events, with the occurrence of a large-scale plunging jet impacting on the deck and dominating the water-on-deck features; and hammer fist (HF, figure d) type events. The ratio $\frac{W_w}{W}$ is used to characterize the local effect of the ship on the free-surface elevation, while the wave steepness is a measure of the incoming-wave non-linearities.

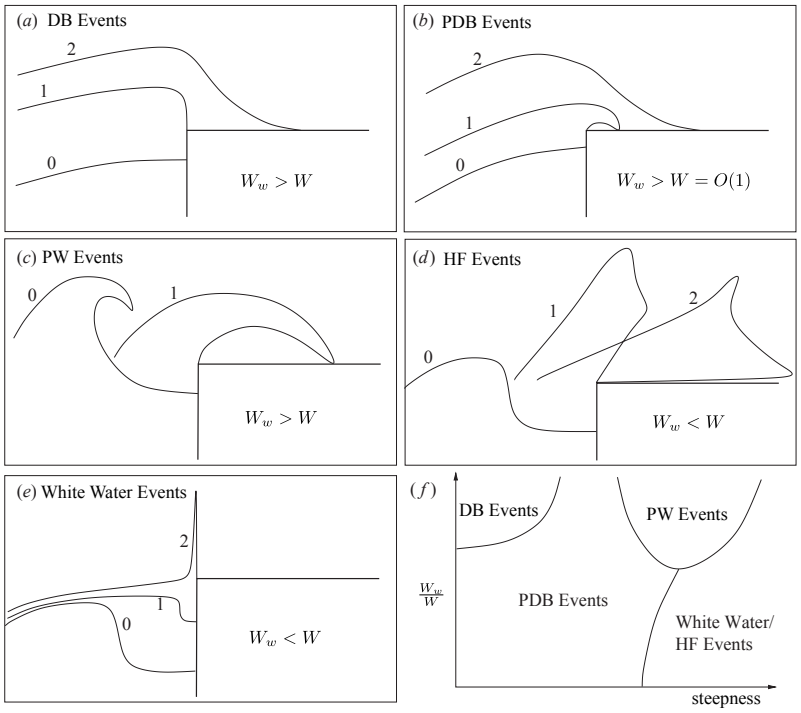

Figure 2.1: Scenarios of green water. Adapted from GRECO *et al.* [24]

The PDB type events are documented in GRECO *et al.* [7] and the HF type events are documented in GRECO *et al.* [24]. According to BUCHNER [6], most cases of green water flow onto the deck are resemble with theoretical dam break model. Therefore, in the present work, we mainly consider the DB type events.

2.1.2 Green water impact on structures

In the green water problem, the horizontal velocity becomes dominant once the flow reaches the deck level. When the high velocity water front on the deck reaches a structure, this results in significant impact loading on the structure. The behavior of the wave front resemble a jet impinging perpendicularly a vertical wall. In such a scenario, BUCHNER [21] extended the slamming expression given by SUHARA *et al.* [25] to the green water problem. In this expression the peak pressure depends on the square of the velocity,

$$P = c\rho u^2 \tag{2.1}$$

where P is the peak impact pressure, c is called the impact coefficient, ρ is the fluid density and u is the horizontal velocity. Based on empirical relations obtained from experiments, SUHARA *et al.* [25] proposed an impact coefficient $c = 1.4$ for bottom slamming situations. A different impact coefficient value of 0.88 was proposed by BUCHNER [6], using Eq. (2.1) , and he commented that factor $c = 1.4$ was conservative for the impact pressure.

BUCHNER [6] also noted a almost linear relationship between the impact force and the maximum water height on deck, which is consistent with the experimental results by FONSECA and SOARES [26]. BUCHNER [6] then introduced a new expression as,

$$F = h_{max}\rho u^2 \tag{2.2}$$

where F is the peak force per meter breadth, and h_{max} is the maximum water height on deck.

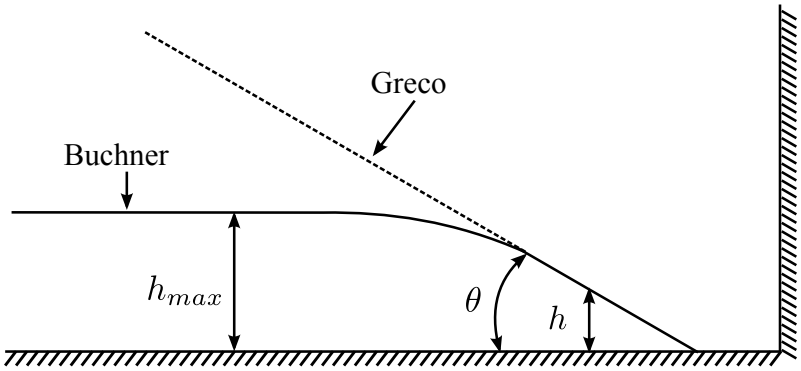

Figure 2.2: Schematic green water flow over the deck

GRECO [11] also followed the approach of representing the impact induced by the green water problem as a slamming problem. She treated the problem as a semi-infinite water wedge impact on a wall with wedge angle θ, shown in Fig. 2.2. The zero-gravity similarity solution proposed by ZHANG *et al.* [27] was used to study the influence on the impact coefficient, as shown in Fig. 2.3. It was found

that when $\theta \leq 35°$ the peak pressure occurs at the intersection of the wall and the deck (the bottom), while for larger angles the peak pressure shifts up. When the angle is large enough (i.e $\theta > 60°$), the results agree qualitatively with the results obtained using WAGNER [28] slamming theory.

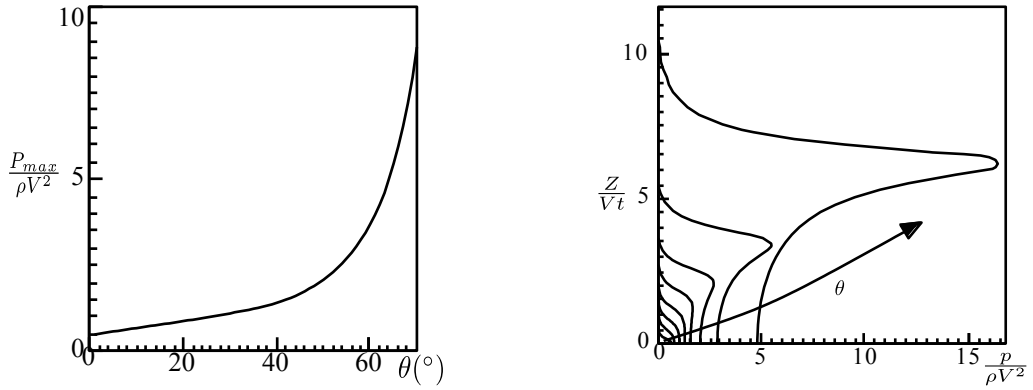

(a) Peak impact pressure with different angle

(b) Pressure distribution along the vertical wall for $5 < \theta < 75°$ with increment $\Delta\theta = 10°$

Figure 2.3: Results of similarity solution by ZHANG *et al.* [27], adapted from GRECO [11]

The semi-infinite water wedge assumption by GRECO [11] and the similarity solution by ZHANG *et al.* [27] were implemented in a numerical tool developed by STANSBERG *et al.* [29, 30]. They concluded that the predicted force peak values compared well with experimental data.

These researches indicates that the green water impact on structures are determined by the propagating wave front velocity and its shape (the angle θ). One may use the classical "Stoker solution" to predict the wave front velocity and its shape. By neglecting the bottom friction, "Stoker solution" predicts a constant wave front velocity ($2\sqrt{gH}$) with a parabolic free surface profile and the tangent at the wave front tip is horizontal. However, experimental data such as DRESSLER [31] and LOBOVSKỲ *et al.* [32] have shown that both wave front velocity and its shape are affected by the bottom friction. This emphasizes the necessity to include the bottom friction in the analytical approaches.

More recent, ARIYARATHNE *et al.* [33] studied the green water phenomenon for a breaking wave case. They suggested that the fluid density needs to be corrected by introducing void fraction factor α for the bubbly multi-phase flow.

$$P = c(1 - \alpha)\rho u^2 \tag{2.3}$$

For the wall impingement condition, the impact coefficient with void fraction factor was found to be $c = 1.3$, which is close to the value of 1.4 reported in SUHARA

et al. [25].

2.1.3 Green water loading on deck

Once the green water flows onto the deck, it is not only impacts on the superstructures, but also acts on the deck. By defining a control volume on the deck and applying the Newton's momentum relations, the total pressure on the deck was given by BUCHNER [6, 21, 34] as:

$$P = \rho(g + \frac{\partial w}{\partial t})h + \rho(\frac{\partial h}{\partial t})w \tag{2.4}$$

The first term represents the static pressure corrected for the vertical acceleration of the deck, whereas the second term includes the effect of the rate of change of water height on the deck.

OGAWA *et al.* [35] presented another approximation in regular waves,

$$F = \alpha\rho g B(fe)^2 \tag{2.5}$$

where α is the coefficient, approximated as 0.3 by the results of experiment, ρ is water density, g is gravity acceleration, B is the breadth of a ship, and fe is the freeboard exceedance.

The green water loading on deck would contribute to the pitch motion of the ship. In the present work, we simply the problem of the pitch motion with a static pitch angle. Thus, the effects due to this loading would not be considered.

2.2 The BIV technique

Velocity measurement is one basic topic in fluid mechanics and various measurement techniques have been developed.

Early quantitative measurement methods using Pitot tubes, Venturi tubes and later measurement methods, such as Hot Wire Anemometry (HWA) and Laser-Doppler Anemometry (LDA), by their nature, were measurement methods that provided instantaneous velocity signals at single-points through time.

Recently, the advent of modern imaging, laser, and data acquisition technology has allowed for the development and advancement of several relatively new measurement techniques, namely Particle Tracking Velocimetry (PTV), Laser Speckle Velocimetry (LSV), and Particle Image Velocimetry (PIV). These techniques allow to measure the instantaneous velocity for a large flow field by recording images of suspended seed particles in flows.

An important difference among the three techniques comes from the typical seeding densities that can be dealt with by each technique. PTV is appropriate with low seeding density experiments, PIV with medium seeding density and LSV with high seeding density. In PIV, a typical interrogation region may contain images of 10-20 particles. In LSV, the particle densities are so large that individual particles are not distinguishable.

The Bubble Image Velocimetry (BIV) technique proposed by RYU *et al.* [15] is a kind of direct adoption of the PIV technique. Hence, it implicit assumes the bubble (seeding) density is medium. Issues may arise on this point, since RYU *et al.* [15] claimed that BIV could be used to very high void fraction cases, which means the bubble (seeding) density is high. In the present work, we assume a medium bubble (seeding) density.

In the following section, the general description of the PIV technique and its developments to the BIV technique is given.

2.2.1 General Description of PIV

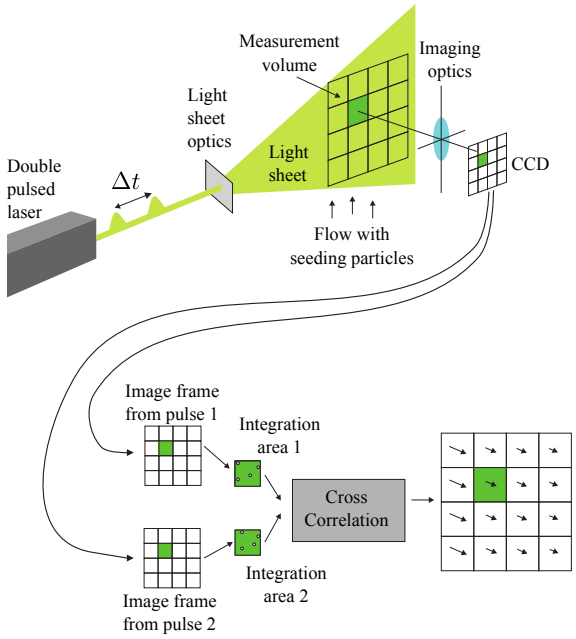

Figure 2.4: Typical arrangement for particle image velocimetry

A typical setup for PIV recording is shown in Fig. 2.4. Small seeding particles are added to the flow. The seeded flow is illuminated by a thin light sheet generated by a pulsed laser with its necessary optics. The sheet is pulsed twice and recorded by a camera located perpendicular to the sheet. The recorded image pairs are processed to determine the displacement of particles with a cross-correlation algorithm. The displacements are then converted from the image pixelated domain to the spatial

domain via a calibration procedure. Finally, the particle displacements within the spatial domain are then divided by the time separation between the laser pulses that singly exposed sequential images, i.e. velocity = displacement/Δt, to provide the velocity field.

The seeding particles added to the flow need to have control over their size, density, and distribution. For ease of use, these particles should be nontoxic, non-corrosive, and chemically inert. They should also be small enough to be good flow tracers, yet large enough to scatter sufficient light for imaging. The density of the particles should be as close as possible to the fluid. The distribution of particles should be homogeneous. MELLING [36] presented a wide variety of tracer particles that have been used in liquid and gas PIV experiments, as well as methods of generating seeding particles and introducing them into the flow.

After the images containing particles are acquired, the most sensitive part of a PIV analysis is the cross-correlation algorithm. The algorithm cross correlates small sub images (interrogation areas) of an image pair to derive the most probable particle displacement in the interrogation areas. Following HUANG *et al.* [37], the cross-correlation for two discretely sampled images can be written as:

$$C(m,n) = \sum_{i} \sum_{j} A(i,j)B(i-m, j-n) \tag{2.6}$$

where $A(i,j)$ and $B(i,j)$ are corresponding to the image intensity distribution in the first and second image of a singly exposed image pair, m and n are the pixel offset between the two images and $C(m,n)$ is the cross-correlation function.

According to RAFFEL *et al.* [16], there are two common approaches to solve Eq. (2.6). The most straightforward approach is to compute the correlation matrix in the spatial domain. This approach is called direct cross correlation (DCC). Another approach is to compute the correlation matrix in the frequency domain, called as Discrete Fourier Transform (DFT). The DFT is calculated using a Fast Fourier Transform (FFT). A graphical representation of the two cross-correlation algorithms are shown in Fig. 2.5a and Fig. 2.5b respectively.

DCC has been shown to create more accurate results than DFT, according to HUANG *et al.* [37]. However, regarding that several thousand velocity vectors can be computed from one single pair of images the computational effort of DCC is enormous. Given the size of a square interrogation area N, a number of operations of the order of N^4 have to be computed. On the other hand, the computational effort of DFT is reduced to the $O[N^2 \ln N]$.

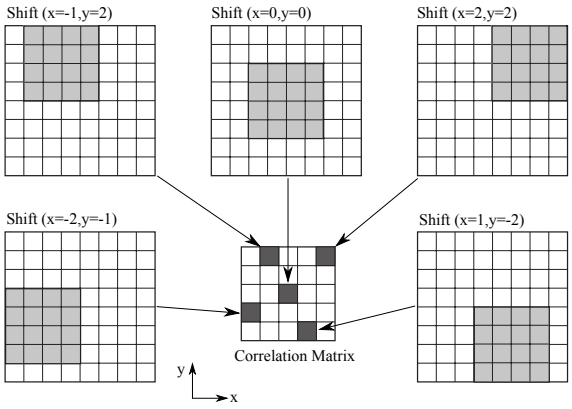

(a) Example of the formation of the correlation plane by DCC

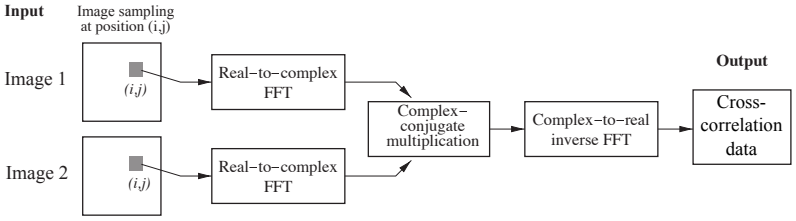

(b) Implementation of cross-correlation using FFT

Figure 2.5: The cross-correlation algorithms, adapted from RAFFEL *et al.* [16]

The most probable displacement of the particles from A to B is given by the location of the intensity peak in the resulting correlation matrix $C(m, n)$. By finding the maximum value in $C(m, n)$ and using a curve fitting technique for subpixel accuracy, the mean particle displacement (Δx , Δy) over the small area that occurs at the highest correction can be obtained. The most common used curve fitting technique is the three-point Gaussian fit, as shown in Fig. 2.6.

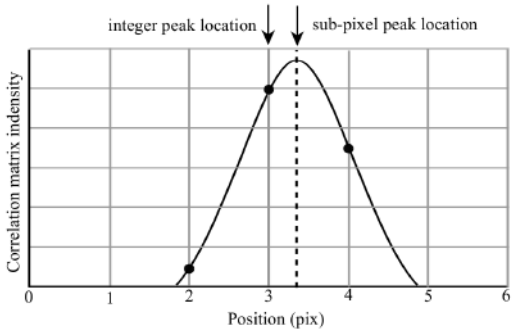

Figure 2.6: Principle of the three-point Gaussian fit, adapted from THIELICKE and STAMHUIS [38]

The velocity can be subsequently calculated as,

$$u = \frac{\Delta x}{\Delta t} \tag{2.7}$$

$$v = \frac{\Delta y}{\Delta t} \tag{2.8}$$

2.2.2 Consideration for PIV in bubbly flow

In general, the classical PIV technique uses a thin laser light sheet for illumination and with a perpendicular arrangement of the camera with respect to the light sheet. For its application to bubble field, two main characteristics of the bubble should be noted:

- The bubble size (typically in units mm) is even larger than the thickness of thin laser sheet (typically several hundreds μm)
- The bubble light scattering is much different than the solid seeding particles, for a spherical bubble, it may have reflection, refraction, second refraction, see Fig. 2.8, and for non-spherical bubble, the light scattering would be even more complicate.

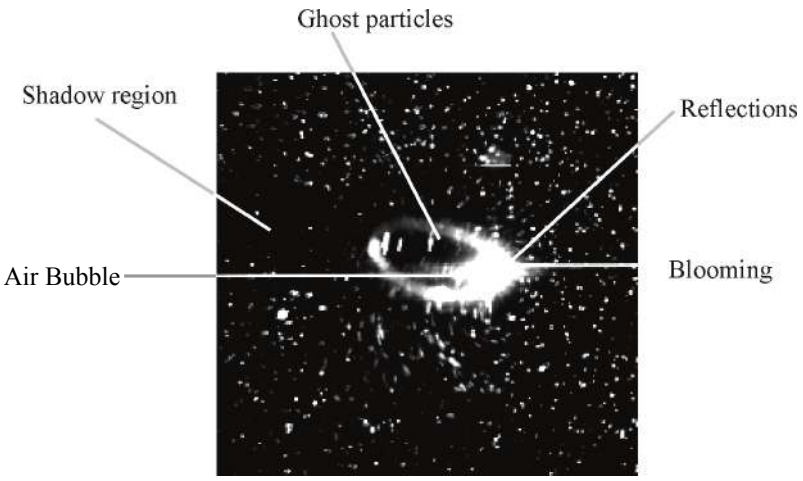

Figure 2.7: PIV image around an air bubble in a thin light-sheet, adapted from BRÜCKER [39]

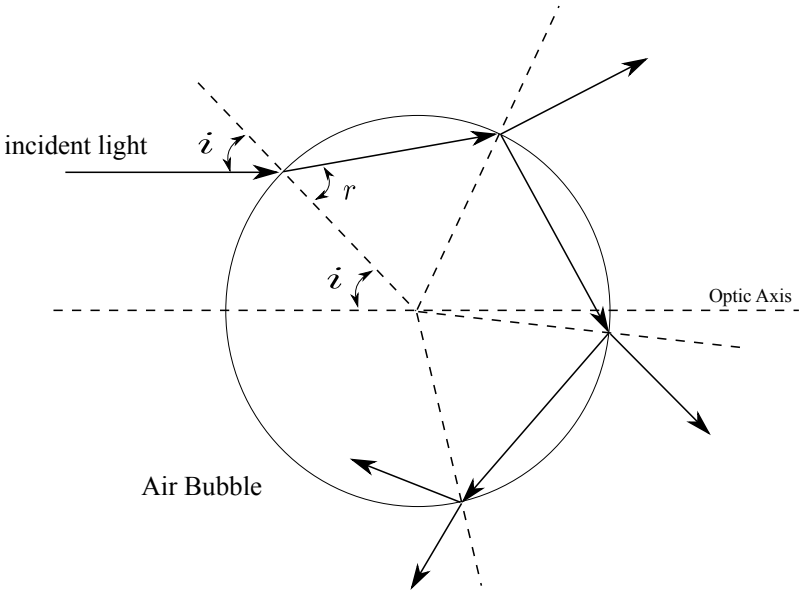

Figure 2.8: Reflection and refraction of components of an incident ray for an air bubble, adapted from DAVIS [40]

For the first characteristic, as shown in Fig. 2.7 ,BRÜCKER [39] commented that as soon as the bubble enters the light-sheet, strong reflection occurs which yields a shadow region behind the bubble. In the strong reflection area the light intensity is too high (too bright) and in the shadow region the light intensity is too low (too dark). These areas are lost for any valuable information. In addition, ghost images seem to appear inside the bubble due to a mirror effect at the phase boundary. These aspects strongly affect the quality of the results around the bubble. For the second characteristic, BRÖDER and SOMMERFELD [41] found that the scattering light intensity of air bubbles in water decrease strongly for off-axis angles larger than 82.5°. They concluded that the perpendicular arrangement of the camera in the classical PIV technique was not suitable for taking images of bubbles in a light sheet. Therefore, it is not considered to be suitable directly apply the PIV technique for bubble velocity field measurement.

BRÜCKER [39] pointed that to use the PIV technique for the dispersed phase, a combination of the shadowgraph technique is recommended. A shadow image is cast by bending of the light rays coming from the back side of the bubbles. The refraction by strong curvature of the bubbles projects the dark part and hence casts a shadow on the camera against the bright background. The early works of the combination of PIV technique and the shadowgraph technique was refered to TOKUHIRO *et al.* [42], DIAS and REITHMULLER [43], LINDKEN and MERZKIRCH [44],BRÖDER and SOMMERFELD [45], FUJIWARA *et al.* [46], more recent, SATHE *et al.* [47]. As shown in Fig. 2.9, these studies were mainly focused on the low void fraction cases (i.e single bubble rising) with the seeding particles. The bubble itself was not treated as tracers and its velocity was evaluated by its surrounding seeding particles.

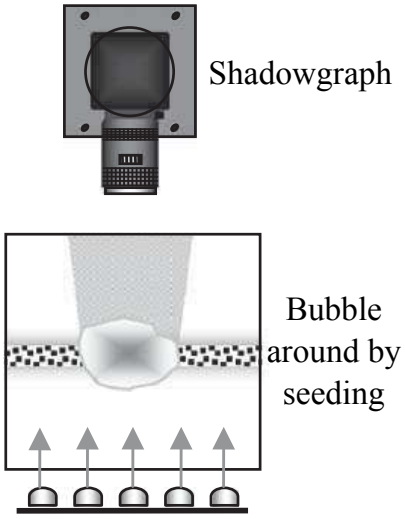

Figure 2.9: Sketch of a combination of the shadowgraph with PIV, adapted from SATHE *et al.* [47]

2.2.3 General description of BIV technique

Recently, also based on the idea of combining the shadowgraph technique that illuminates the fluid from behind to reveal the flow pattern, and the classical PIV technique that correlates the consecutive images to determine the velocity, RYU *et al.* [15] introduced the so-called Bubble Image Velocimetry (BIV). The arrangement of the BIV system is sketched in Fig. 2.10.

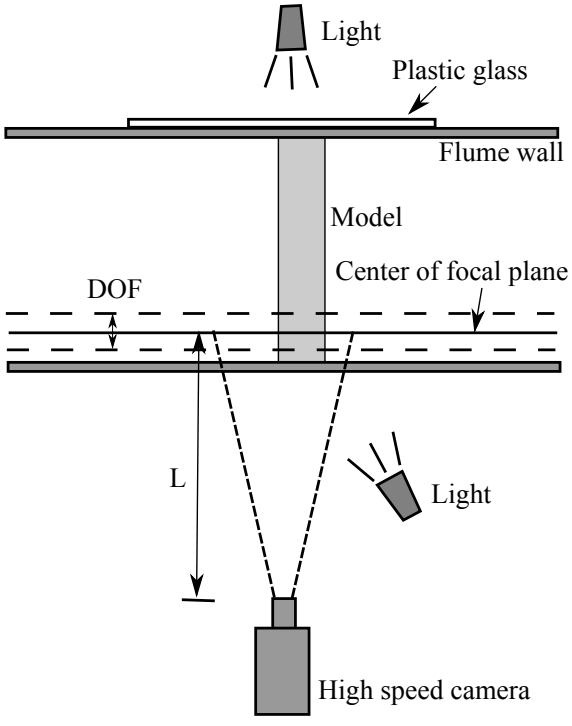

Figure 2.10: Sketch of BIV arrangements, adapted from RYU *et al.* [15]

In contrast to the previous PIV work in bubbly flow, RYU *et al.* [15] did not add small seeding particles in the flow, but they treated the bubble itself as the tracer particles. Since no seeding particles is added to the flow, the laser light sheet is not required for the BIV technique. Instead, RYU *et al.* [15] used two regular 600 W light bulbs to illuminate the flow. The main light together with a translucent plastic glass (as a diffuser) was placed at the back side of the tank to cast the shadow images. The other light was placed on the front side to improve the light intensity in the images. Since the BIV technique does not use a thin light sheet to illuminate a specific plane of interest like the PIV method, it is necessary to know where the measured bubbles are in the cross-tank direction. The measured volume is determined by the depth of field (DOF) of the camera, which is given as,

$$DOF = \frac{Lf^2}{f^2 - f^{\#}LC} - \frac{Lf^2}{f^2 + f^{\#}LC} \tag{2.9}$$

where L donates the distance between camera and the center of focal plane; f is focal length of camera lens, $f^{\#}$ is the camera aperture number and C represents the circle of confusion. In the work of RYU *et al.* [15], $L = 4.0$ m, $f = 105$ mm, $f^{\#} = 1.8$, and $C = 0.03$ mm, therefore the corresponding DOF is $D = 0.15m$. Comparing to the PIV technique, in which the thickness of the thin light sheet is typically 100 μm to 300 μm , the DOF is much larger. This becomes one of the main error source of the BIV technique. RYU *et al.* [15] assumed this error due to the thickness of the DOF in the obtained velocity can be estimated approximately as,

$$\varepsilon \approx \frac{DOF}{2L} = 1.88\% \tag{2.10}$$

RYU *et al.* [48] applied the BIV technique to study the runup and green water velocity due to breaking wave impinging and overtopping. Based on the measured data, they proposed a equation for predicting the horizontal velocity distribution of green water along the deck. Based on the velocity obtained by the BIV technique, RYU *et al.* [8] compared the green water velocity obtained by the BIV technique with the theoretical "Stoker solution", they concluded that the comparison was surprisingly well. RYU and CHANG [49] employed the BIV technique together with a fiber optic reflectometer (FOR) to measure the velocity and the void fraction in the flow, and to determine the water level on the deck.

Chapter 3

Analytical Dam Break Solutions

Sudden destruction of a dam results in a highly unsteady flow, with a forward wave advancing over a channel, and a backward disturbance wave propagating into the still water. Dam break problem is one of the classical problems of unsteady open channel flow.

This chapter deals with the dam break problem by the analytical approach and is structured as follows. After this brief introduction, the theoretical background of the two Stoker solutions is given, namely Eulerian Stoker solution and Lagrangian Stoker solution. Following that, the attempts to include the bottom friction effects are also described. Finally, a simplified dam break solution including the bottom friction effects and bed slope effects is presented.

3.1 Stoker solutions

In this section we introduce the theoretical background for the two Stoker solutions. Since ESS is the popular one, it would be described briefly while more details of LSS would be given.

3.1.1 Eulerian Stoker solution

Under certain hypotheses, the dam break flow can be described by the Saint Venant equations (SVE), which are written as follows in the 1-D sense:

$$\frac{\partial h}{\partial t} + \frac{\partial hu}{\partial x} = 0 \tag{3.1}$$

$$\frac{\partial u}{\partial t} + u\frac{\partial u}{\partial x} + g\frac{\partial h}{\partial x} = g(S_0 - S_f) \tag{3.2}$$

where h is the local depth at each section, u is the local horizontal velocity, S_0 is the bed slope and S_f is the friction slope. Eq. (3.1) comes from the continuity condition across a channel section and Eq. (3.2) is the momentum equation. The basic

assumptions of SVE are that the flow is incompressible, the water depth is shallow, the flow velocity is uniform over a cross section and the pressure is hydrostatic.

Considering a horizontal channel ($S_0 = 0$) with a dry bed and ignoring the bottom friction ($S_f = 0$), using the method of characteristics to solve the SVE, STOKER [10] presented an analytical solution in Eulerian representation, the ESS, which contains two expressions, Eq. (3.3) for the water depth and Eq. (3.4) for the sectional velocity:

$$h = \begin{cases} H & \text{for } \dfrac{x}{t} < -\sqrt{gH} \\ \dfrac{1}{9g}(2\sqrt{gH} - \dfrac{x}{t})^2 & \text{for } -\sqrt{gH} < \dfrac{x}{t} < 2\sqrt{gH} \\ 0 & \text{for } \dfrac{x}{t} > 2\sqrt{gH} \end{cases} \tag{3.3}$$

$$u = \frac{2}{3}(\frac{x}{t} + \sqrt{gH}) \tag{3.4}$$

ESS is sketched in Fig. 3.1. ESS predicts a constant water level $\frac{4H}{9}$ at the dam section $x = 0$ for time $t > 0$, which could be obtained by setting $x = 0$ in Eq. (3.3). Since the bottom friction is ignored, the downstream wave front velocity is also constant and equals to $2\sqrt{gH}$.

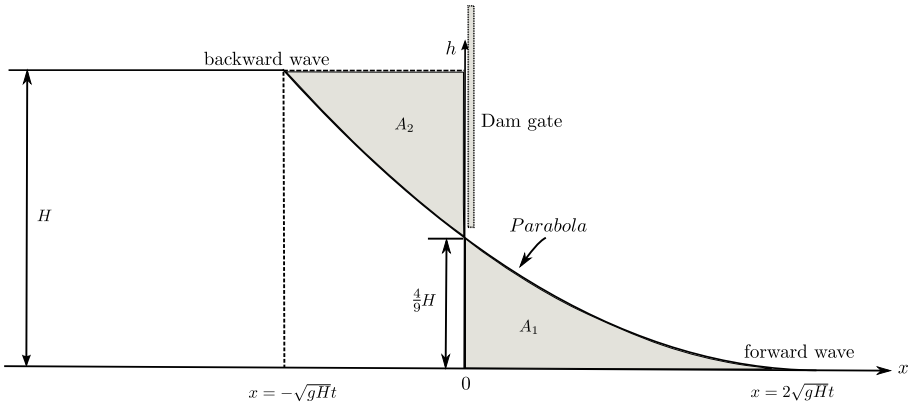

Figure 3.1: Dam break in Eulerian representation, adapted from STOKER [10]

3.1.2 Lagrangian Stoker solution

An alternative solution to the dam break problem was also proposed by STOKER [10]. This solution is based on the Lagrangian representation, as sketched in Fig. 3.2.

Assuming that the region occupied initially by the water is the half strip defined by $0 \leq a < \infty$, $0 \leq b \leq H$, where H denotes the height of the dam and a and b represent Cartesian coordinates of the initial positions of the particles at time $t = 0$. The dam gate is located at $a = 0$ and the displacements of the particles are denoted by $X(a, b; t)$, $Y(a, b; t)$ and the pressure by $p(a, b; t)$.

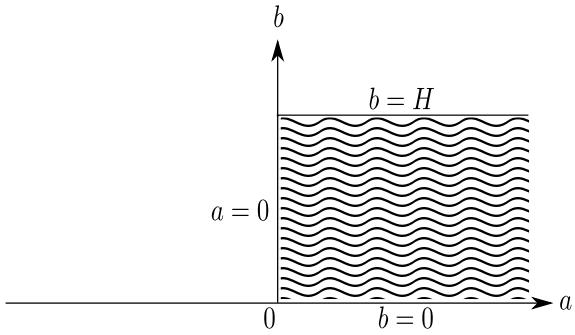

Figure 3.2: Dam break in Lagrangian representation, adapted from STOKER [10]

If gravity is assumed to be the only external force, then according to Newton's second law, the equations of motion are:

$$X_{tt} = -\frac{1}{\rho} p_X \tag{3.5a}$$

$$Y_{tt} = -\frac{1}{\rho} p_Y - g \tag{3.5b}$$

where subscripts indicate differentiation. From Eq. (3.5), STOKER [10] evaluated the equations of motion in the Lagrangian form as:

$$X_{tt} X_a + (Y_{tt} + g) Y_a + \frac{1}{\rho} p_a = 0 \tag{3.6a}$$

$$X_{tt} X_b + (Y_{tt} + g) Y_b + \frac{1}{\rho} p_b = 0 \tag{3.6b}$$

where Eq. (3.6a) is obtained by multiplying Eq. (3.5a) with X_a and Eq. (3.5b) with Y_a, and add them; similarly, Eq. (3.6b) is obtained by multiplying Eq. (3.5a) with X_b and Eq. (3.5b) with Y_b, and add them.

For an incompressible fluid, the condition of continuity is expressed as follows:

$$X_a Y_b - X_b Y_a = 1 \tag{3.7}$$

Following STOKER [10], we assume that X, Y and ρ can be expanded in power series of time,

$$X(a, b; t) = a + X^{(1)}(a, b)t + X^{(2)}(a, b)t^2 + ... \tag{3.8a}$$

$$Y(a, b; t) = b + Y^{(1)}(a, b)t + Y^{(2)}(a, b)t^2 + ... \tag{3.8b}$$

$$p(a, b; t) = p^{(0)} + p^{(1)}(a, b)t + p^{(2)}(a, b)t^2 + ... \tag{3.8c}$$

where $X^{(1)}$ and $Y^{(1)}$ are the components of the initial velocity and $X^{(2)}$ and $Y^{(2)}$ similarly for the acceleration. STOKER [10] stated that the series will converge for sufficiently small values of the time. But the convergence characteristics of the series

have not been studied here. In order to determine the displacements terms ($X^{(n)}$ and $Y^{(n)}$) and the pressure terms ($p^{(n)}$), the boundary value problem needs to be solved.

Assuming the water is initially at rest, the boundary conditions of the displacements follow:

$$X(a,b;0) = a,\ Y(a,b;0) = b \tag{3.9}$$

$$X_t(a,b;0) = 0,\ Y_t(a,b;0) = 0 \tag{3.10}$$

The conditions (3.9) are automatically satisfied because of the form (3.8) chosen for the series expansion. The conditions (3.10) are satisfied by taking $X^{(1)} = Y^{(1)} = 0$.

Initially, the free surface is represented by the particles on $(0 \leq a < \infty, b = H)$ and $(a = 0, 0 \leq b \leq H)$. When the dam is broken, the pressure can be prescribed to be zero on the free surface:

$$p(a,H;t) = 0,\ 0 \leq a < \infty,\ t > 0 \tag{3.11a}$$

$$p(0,b;t) = 0,\ 0 \leq b < H,\ t > 0 \tag{3.11b}$$

Inserting the power series (3.8a) in Eq. (3.6a) and considering the boundary condition on $(0 \leq a < \infty, b = H)$, we have:

$$X^{(2)}(a,H) = 0 \tag{3.12}$$

again inserting the power series (3.8b) in Eq. (3.6b) and considering the boundary condition on $(a = 0, 0 \leq b \leq H)$, yields:

$$Y^{(2)}(0,b) = -\frac{g}{2} \tag{3.13}$$

Finally we consider the boundary conditions on the bottom ($b = 0$). Assuming that the water particles originally at the bottom remain in contact with it, this results:

$$Y(a,0;t) = 0 \quad 0 \leq a < \infty,\ t > 0 \tag{3.14}$$

From the condition (3.14), we have $Y^{(2)}(a,0) = 0$ (in fact, $Y^{(n)}(a,0)$ would be zero for all n).

By inserting the power series (3.8) in Eq. (3.6), we can build the relationship between the pressure and displacement:

$$p_a^{(0)} = -2\rho X^{(2)} \tag{3.15a}$$

$$p_b^{(0)} = -2\rho Y^{(2)} - \rho g \tag{3.15b}$$

Considering the second derivative of pressure in a and b respectively, from Eq.(3.15) we have:

$$p_{aa}^{(0)} + p_{bb}^{(0)} = -2\rho(X_a^{(2)} + Y_b^{(2)}) = 0 \tag{3.16}$$

Once $p^{(0)}$ is found, $X^{(2)}$ and $Y^{(2)}$ can be calculated and vice versa. Using the method of conformal mapping, the solution to $X^{(2)}$ and $Y^{(2)}$ are given by STOKER [10] as:

$$X^{(2)}(a,b) = -\frac{g}{2\pi}\log\{\frac{\cos^2\frac{\pi b}{4H} + \sinh^2\frac{\pi a}{4H}}{\sin^2\frac{\pi b}{4H} + \sinh^2\frac{\pi a}{4H}}\} \tag{3.17a}$$

$$Y^{(2)}(a,b) = -\frac{g}{\pi}\arctan\{\frac{\sin\frac{\pi b}{2H}}{\sinh\frac{\pi a}{2H}}\} \tag{3.17b}$$

and then the solution to pressure $p^{(0)}$ is given as:

$$p^{(0)} = \rho g(H-b) - \frac{8\rho g H}{\pi^2}\sum_{j=1}^{\infty}\frac{1}{(2j-1)^2}\exp[-\frac{(2j-1)\pi}{2H}a]\cos\frac{(2j-1)\pi b}{2H} \tag{3.18}$$

The first term of $p^{(0)}$ represents the hydrostatic pressure.

For higher orders, STOKER [10] stated that a Poisson equation (similar to Eq. (3.16)) can be found for $p^{(n)}$, with the right hand side determined by $X^{(i)}$ and $Y^{(i)}$ for $i = 2, 3, ..., n+2$. STOKER [10] solved the Poisson equation for $n = 0$ and gave the equation for $n = 2$ as:

$$\nabla^2 p^{(2)} = -\frac{8\rho g^2}{H^2(\cosh\frac{\pi a}{H} - \cos\frac{\pi b}{H})} \tag{3.19}$$

YILMAZ *et al.* [50] solved the Eq. (3.19), which allows to give the solution to $X^{(4)}$ and $Y^{(4)}$. However, the computing effort in $X^{(4)}$ and $Y^{(4)}$ is too much higher.

In the present work, we only use the LSS given by STOKER [10] and the shape of the free surface profile is given by the following equations:

$$X = a + X^{(2)}t^2 \tag{3.20a}$$

$$Y = b + Y^{(2)}t^2 \tag{3.20b}$$

evaluated for $a = 0$ (for the particles at the dam section) and for $b = H$ on the upper free surface.

3.2 Eulerian Stoker solution extensions

3.2.1 Bottom friction effects

In ESS, since the bottom friction effects are ignored, the dam break front velocity is constant ($U = 2\sqrt{gH}$). However experimental data have shown that the wave front velocity is not constant but a function of time.

To represent the bottom friction effects, DRESSLER [51] introduced the *Chézy* resistance term K, proportional to $\frac{u^2}{gh}$ in the momentum equation, equivalently in the form of friction slope $S_f = K\frac{u^2}{gh}$. The velocity u and the depth h are then expanded as power series in K, the first terms are the Stoker expressions. By finding the next terms, he was able to see some of the modifications introduced by the bottom friction. A convex shape of the wave front can then be predicted theoretically by DRESSLER [51]. The validity of the results was latter confirmed by the same author DRESSLER [31] with the following assumptions: (a) The product Kt must remain small, (b) the velocity of the water does not vary rapidly in wave tip zone. With the first order approximation, the front velocity is given by DRESSLER [31] as,

$$\frac{U}{\sqrt{gH}} = 2 - 3.59(Kt\sqrt{\frac{g}{H}})^{\frac{1}{3}} + ... \tag{3.21}$$

Later, WHITHAM [18] claimed that Dressler's expressions would not be valid near the wave front (called the tip region) where the frictional resistance is no longer a mere correction term. To improve the solution, he treated the wave front as a growing boundary-layer region and assumed that the bottom friction should be only included in the tip region, differently from Dressler who included the resistance in the whole domain. Based on experimental observation, Whitham also assumed the front velocity is nearly uniform in the tip region.

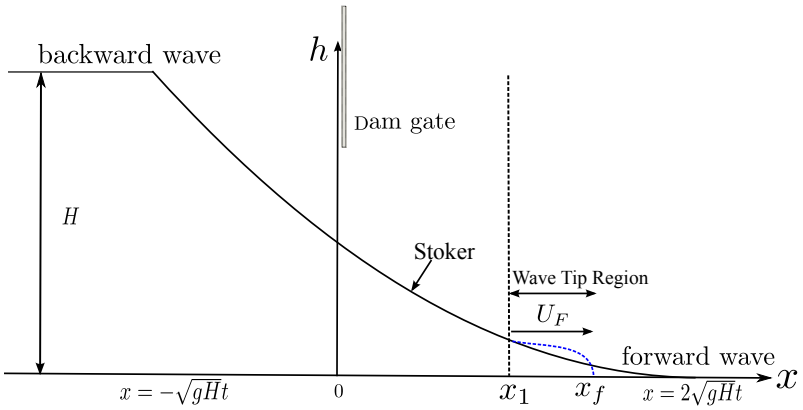

Figure 3.3: The Whitham solution

As shown in Fig. 3.3, $x < x_1$ is the frictionless area where the ESS is valid. In the tip region $x_1 < x < x_f$,where the friction is important, the front velocity is

assumed to be uniform U. Thus, in the tip region, $u_t + uu_x$ is expected to be finite, while h_x becomes large, the momentum equation (Eq. (A.16)) is then reduced to,

$$h_x + K\frac{u^2}{gh} = 0 \tag{3.22}$$

By integrating Eq. (3.22), the wave profile in the tip region could be obtained,

$$h = U\sqrt{\frac{2K}{g}(x_f - x)} \tag{3.23}$$

At $x = x_1$, the velocity and the wave profile are continuous with the ESS,

$$x_1 = (\frac{3U_1}{2} - \sqrt{gH})t \tag{3.24a}$$

$$h_1 = H(1 - \frac{U_1}{2\sqrt{gH}})^2 \tag{3.24b}$$

$$U_1 = U \tag{3.24c}$$

Based on momentum conservation in the tip region, note $U = \dot{x_f}$, yields,

$$\begin{aligned}(1 - \frac{\dot{x_f}}{2\sqrt{gH}})^3\frac{\dot{x_f}t}{\sqrt{gH}} = (1 - \frac{\dot{x_f}}{2\sqrt{gH}})^4 \\ - \frac{\dot{x_f}^2}{\sqrt{gH}\frac{R}{H}\{\frac{x_f}{\sqrt{gH}} - (\frac{3\dot{x_f}}{2\sqrt{gH}} - 1)t\}}\end{aligned} \tag{3.25}$$

Whitham solved this differential equation using a Taylor expansion. The first seven terms are:

$$\begin{aligned}\tau = 0.02431\dot{x_f}^3 + 0.02163\dot{x_f}^4 + 0.01496\dot{x_f}^5 + 0.00941\dot{x_f}^6 \\ + 0.00563\dot{x_f}^7 + 0.00327\dot{x_f}^8 + 0.00186\dot{x_f}^9 + ...\end{aligned} \tag{3.26}$$

where, $\tau = Kt\sqrt{\frac{g}{H}}$. If only take the first term of this series, the front velocity is given by,

$$\frac{U}{\sqrt{gH}} = 2 - 3.452(Kt\sqrt{\frac{g}{H}})^{\frac{1}{3}} + ... \tag{3.27}$$

More recently, CHANSON [19] followed the first steps of Whitham's work but used mass conservation to obtain the front velocity, which led to a much simple formulation for the front velocity. Another different point is that Chanson used the Darcy-Weisbach friction factor f, with relationship $K = f/8$.

In the flow represented in Fig. 3.3, the conservation of mass must be satisfied. Specifically the mass of fluid in the wave tip region (i.e. $x_1 \leq x \leq x_f$) must equal

the mass of fluid in the ideal fluid flow profile for $x_1 \leq x \leq 2\sqrt{gH}t$. It yields,

$$M = \int_{x_1}^{x_f} \rho h_{Whitham} \mathrm{d}x = \int_{x_1}^{2\sqrt{gH}t} \rho h_{Stoker} \mathrm{d}x \tag{3.28}$$

where, $h_{Whitham}$ could be obtained from Eq. (3.23) and h_{Stoker} could be obtained from Eq. (3.3).

By integrating Eq. (3.28), it follows,

$$\frac{1}{3} \frac{(1 - \frac{U}{2\sqrt{gH}})^3}{\frac{f}{8}\frac{U^2}{gH}} = t\sqrt{\frac{g}{H}} \tag{3.29}$$

3.2.2 Dam break wave in a sloping channel

The early studies attempt to extend the solution for a sloping channel are mainly referred to HUNT [52] and CHANSON [19]. HUNT [52] presented a kinematic wave equation for a downward sloping channel, this solution is available in CHANSON [53], as shown in Fig. 3.4.

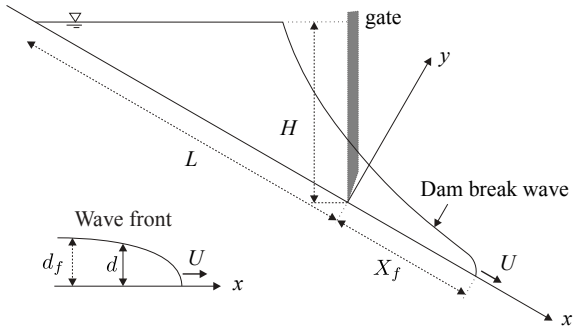

Figure 3.4: Sketch of a dam break wave in a dry downward sloping channel, adapted from CHANSON [53]

Hunt's analysis gives:

$$\frac{V_H t}{L} = \frac{1 - (d_f/H)^2}{(d_f/H)^{3/2}} \tag{3.30}$$

$$\frac{X_f}{L} = \frac{3H}{2d_f} - \frac{d_s}{2H} - 1 \tag{3.31}$$

$$\frac{U}{V_H} = -\frac{3V_H t}{4L} + \sqrt{\frac{X_f + L}{L} + (\frac{3V_H t}{(4L)})^2} \tag{3.32}$$

$$V_H = \sqrt{\frac{8g}{f} H S_0} \tag{3.33}$$

where d_f is the dam break wave front thickness, X_f is the dam break wave front position measured from the dam site, H is the reservoir height at dam site, L is the reservoir length, S_0 is the bed slope ($S_0 = H/L$) and the velocity V_H is the uniform

equilibrium flow velocity for a water depth H. From Fig. 3.4, it can be observed that Hunt's analysis assumes with a finite dam for the downward sloping bed case. This is quite different to ESS which assumes a infinite dam.

CHANSON [19] also developed a solution for a frictionless dry upward sloping channel, as shown in Fig. 3.5. This solution is called as CS, short for Chanson's solution. Chanson's analysis is more similar to STOKER [10], using the method of characteristics (Appendix A.1.2).

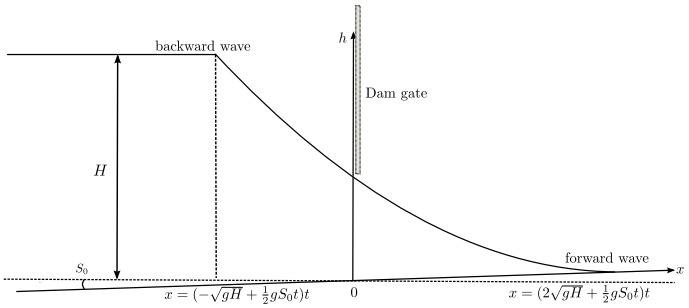

Figure 3.5: Sketch of a dam break wave in a dry upward sloping channel, adapted from CHANSON [19]

Considering the characteristics curve C_1, along C_1, $u + 2c - g(S_0 - S_f)t$ is a constant.

$$u + 2c - gS_0t = u_0 + 2c_0 - gS_0t_0 \tag{3.34}$$

where subscript (0) donates the initial condition. Initially the water is at rest at $t_0 = 0$, this gives $u_0 = 0$ and $c_0 = \sqrt{gH}$. It yields,

$$u = -2c + 2c_0 + gS_0t \tag{3.35}$$

Considering characteristics C_2 issuing from the dam break wave front,

$$\frac{\mathrm{d}x}{\mathrm{d}t} = u - c \tag{3.36}$$

By substituting Eq. (3.35) in Eq. (3.36) and doing integration, it becomes,

$$\frac{x}{t} = -3c + 2c_0 + \frac{1}{2}gS_0t \tag{3.37}$$

Noticing $c = \sqrt{gh}$, the water elevation could then be given as

$$h = \frac{1}{9g}(2c_0 + \frac{1}{2}gS_0t - \frac{x}{t})^2 \tag{3.38}$$

Combining Eq. (3.35) and Eq. (3.37), the velocity formulation can be given as,

$$u = \frac{2}{3}(\frac{x}{t} + c_0 + gS_0t) \tag{3.39}$$

It is should be noted that the axis x and h are not orthogonal as shown in Fig. 3.5. CHANSON [19] did not explain it directly but he claimed that these equations are derived "for the initial stage of the dam break wave on a flat slope". Thus whether this could be worked for a slope bed case remains to be a question.

3.3 A piecewise solution

In this section, we introduce a piecewise solution to include the pitch motion (the bed slope) for predicting shipping of water on deck. In reality, the relative motion between the incoming wave and the ship pitch motion is quite complicated. Here, we simplify the problem as shown in Fig. 3.6: the incoming wave always comes horizontally and induces a horizontal dam; while the ship deck is varying due to pitch motion and may induce both upward and downward sloping bed.

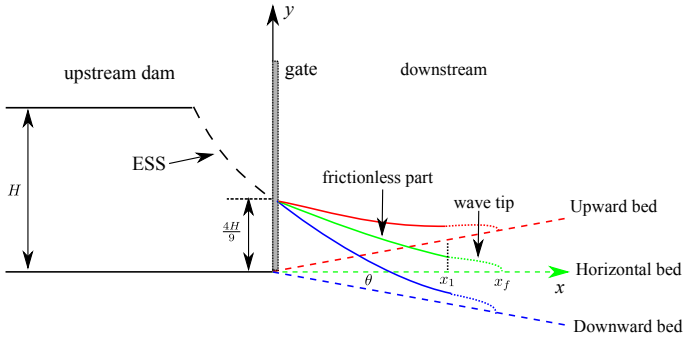

Figure 3.6: Sketch of a horizontal dam with different sloping bed

To deal with the changing in bed slope at $x = 0$, the problem is further simplified. The whole domain can be divided into two part: the upstream and the downstream.

In the upstream side, the bed slope of the dam is horizontal, hence the upstream part could be represented by the ESS: the wave elevation and velocity could be predicted by Eq. (3.3) and Eq. (3.4) respectively. ESS predicts a constant water level ($\frac{4H}{9}$) at the dam gate.

In the downstream side, we firstly consider the horizontal bed slope case. For a horizontal bed case, we can follow WHITHAM [18] and CHANSON [19], as presented in Section 3.2.1. Assuming the bottom friction is only included in the downstream wave tip and the front velocity is uniform in the wave tip. The downstream side could then be divided into two parts: the frictionless part ($0 \leq x \leq x_1$) and the wave tip part ($x_1 \leq x \leq x_f$), as shown Fig. 3.6. The frictionless part for a horizontal bed case can also be represented by ESS. In the wave tip, the wave front velocity can be solved by Eq. (3.29) and the free surface profile is given by Eq. 3.23. Once front velocity (U) is obtained, x_1 and h_1 can be calculated with Eq. (3.24a) and Eq. (3.24b) using $U_1 = U$.

Then for the sloping bed case, considering that the pitch angle is usually small (less than 10 degree), we may assume the downstream elevation of a sloping bed case ($h(\theta)$) can be transformed from the elevation of the horizontal bed case (h) by:

$$h(\theta) = -h\sin(\theta) + h \tag{3.40}$$

Fig. 3.7 shows a example of the transformation from horizontal bed to upward bed ($\theta = -10$) and to downward slope bed ($\theta = 10$). The benefit of this transformation lies that it does not require use of two coordinates system for upstream and down stream.

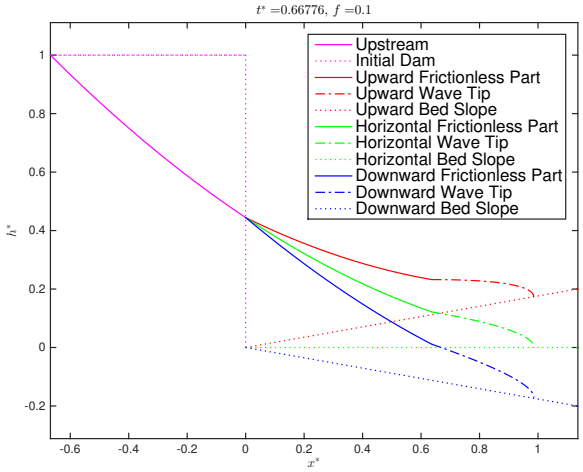

Figure 3.7: Example of transformation for $\theta = 10$ and $f = 0.1$ at instant $t^* = 0.667$

In summary, the piecewise solution (PS) consists of three part: upstream part, downstream frictionless part and downstream wave tip part. The formulations to determine elevation in each part are summarized in Table 3.1.

Table 3.1: Summary of the piecewise solution

	Elevation	Transformation
upstream	$h = \frac{1}{9g}(2\sqrt{gH} - \frac{x}{t})^2$	No
frictionless part	$h = \frac{1}{9g}(2\sqrt{gH} - \frac{x}{t})^2$	YES
wave tip	$h \approx \sqrt{\frac{f}{4}\frac{U^2}{g}(x_f - x)}$	YES

3.3.1 Solution with a compensated time factor

Introducing a compensated time factor t_c in time as:

$$t' = t - t_c \tag{3.41}$$

For instance, the compensated Stoker Euler solution (the upstream part of PS) becomes:

$$h' = \begin{cases} H & for\ \frac{x}{t'} < -\sqrt{gH} \\ \frac{1}{9g}(2\sqrt{gH} - \frac{x}{t'})^2 & for\ -\sqrt{gH} < \frac{x}{t'} < 2\sqrt{gH} \\ 0 & for\ \frac{x}{t'} > 2\sqrt{gH} \end{cases} \tag{3.42}$$

$$u' = \frac{2}{3}(\frac{x}{t'} + \sqrt{gH}) \tag{3.43}$$

where superscript $'$ donates the compensation with time. Considering time t' could not be negative, this means the compensation should be used at least when time $t > t_c$. The compensation in time will delay the velocity and improve the wave front tracking ability in time $t > t_c$. This would be discussed with experimental data in the later part of this thesis.

Chapter 4

Numerical Dam Break Model

In this chapter the numerical code used for the simulation is described. The dam break wave is a multiphase flow, including two immiscible fluids: air and water. To simulate the evolution of the interface between two immiscible fluids two basic approaches can be followed: interface tracking method and interface capturing method. The interface tracking method requires meshes that track the interfaces. The mesh needs to be updated as the flow evolves. In the interface capturing method, the computations are based on fixed spatial domains. In this study, simulations of the dam break flow are based on the interface capturing method with a modified version of the volume-of-fluid (VOF) approach, employed in the interFoam solver of OpenFOAM version 2.3.0.

The present chapter is structured as follows. A brief overview of the OpenFOAM toolbox is given first. The formulations of the interFoam solver would then be followed. In the following sections, the modifications in the interFoam solver would be described with extra attention. Finally, the interFoam solver is validated with previously published experimental data.

4.1 Overview of OpenFOAM

OpenFOAM (Open Field Operation And Manipulation) is a free and open source CFD toolbox. A general description about OpenFOAM could be found in JASAK *et al.* [54] and JASAK [55]. Basically it consists a bundle of C++ libraries and codes to solve complex problems such as turbulence, fluid flows, electromagnetics and chemical reactions using finite volume discretisation. It also features several applications to pre- and post-process the cases, including mesh generation tools (blockMesh, snappyHexMesh), setting field values, mesh decomposition, sampling data (isosurfaces, gauges). OpenFOAM is prepared to run cases in parallel, handling itself the decomposition process and the final reconstruction process.

Unlike commercial codes the OpenFOAM is not a black box. By changing the

source code, every step of of the solving process is user controllable and modifiable. This is a great advantage. It also includes several modules deal with data conversion from and to commercial CFD codes (Ansys, Fluent, CFX). This allows the cross validations with the commercial codes.

4.2 interFoam solver

The "interFoam" is one of the solvers included in OpenFOAM. It solves the three-dimensional Reynolds Averaged NavierStokes (RANS) equations for two incompressible phases using a finite volume discretisation and a modified volume of fluid (VOF) method.

4.2.1 RANS equations

The RANS equations, which include equation of continuity (Equation 4.1) and equation of motion (Equation 4.2), are the governing mathematical expressions which link pressure and velocity. The assumption of incompressible fluids has been used, which is applicable for the dam break problem.

$$\nabla \cdot \mathbf{U} = 0 \tag{4.1}$$

$$\frac{\partial \rho \mathbf{U}}{\partial t} + \nabla \cdot (\rho \mathbf{U}\mathbf{U}) - \nabla \cdot (\mu^{eff} \nabla \mathbf{U}) - \nabla \cdot (\mu^{eff} \operatorname{dev}(\nabla \mathbf{U})^T) = -\nabla \mathbf{p}_{rgh} - g \cdot \mathbf{X} \nabla \rho + \sigma \kappa \nabla \alpha \tag{4.2}$$

where ρ is the density; $\mathbf{U}$ is the velocity vector; $\mathbf{p}_{rgh}$ is the modified pressure; g is the acceleration of gravity and $\mathbf{X}$ is the position vector. The terms include the effective dynamic viscosity μ_{eff} are the stress terms, which are reformulated from the deviatoric viscous stress tensor τ and the Reynolds stress tensor $\mathbf{R}$ to improve the efficiency in numerical evaluation. The last term on the right is the effect of surface tension: σ is the surface tension coefficient; κ is the curvature of the interface and α is the water volume fraction, solved by the modified VOF method.

The elements in Equation 4.2 have a particular disposition: those placed on the left hand side (LHS) of the equals sign are used in OpenFOAM to assemble the coefficient matrix, and the ones on the right hand side (RHS) are calculated explicitly and form the independent term of the equations.

The modified pressure, the reformulated viscous stress terms and the modified VOF method would be described detailly in the later sections.

Modified Pressure

Considering the body force is only gravitational, to simplify the specification of the pressure boundary conditions RUSCHE [56] introduced the modified pressure as:

$$\mathbf{p}_{rgh} = \mathbf{p} - \rho \mathbf{g} \cdot \mathbf{X} \tag{4.3}$$

The gradient of Equation 4.3 reads,

$$\begin{aligned} \nabla \mathbf{p}_{rgh} &= \nabla \mathbf{p} - \nabla(\rho \mathbf{g} \cdot \mathbf{X}) \\ &= \nabla \mathbf{p} - \rho \mathbf{g} - \mathbf{g} \cdot \mathbf{X} \nabla \rho \end{aligned} \tag{4.4}$$

RUSCHE [56] states that this treatment also enables an efficient numerical treatment of the steep density jump at the interface by including the hydrostatic term $\mathbf{g} \cdot \mathbf{X} \nabla \rho$ into the RHIE and CHOW [57] interpolation. The Rhie-Chow interpolation is the same as adding a pressure term, which is proportional to a third derivative of the pressure. The object of Rhie-Chow interpolation is to eliminate pressure oscillations and thereby also velocity oscillations. The oscillations occur if the pressure gradient does not depend on the pressure in adjacent cells and thus allowing a jigsaw pattern. Further discussion of the Rhie-Chow interpolation implemented in OpenFOAM may refer to KÄRRHOLM [58].

Reformulated stress terms

The Navier-Stokes equations should be supplemented by an equation, which relates the deformations and the stresses within the fluids. If the fluids obey the Newtonian law of viscosity, the deviatoric viscous stress tensor is given by:

$$\tau = \mu(\nabla \mathbf{U} + (\nabla \mathbf{U})^T) \tag{4.5}$$

By applying the RANS approach, the Reynolds stress tensor is introduced,

$$\mathbf{R} = \rho \overline{\mathbf{U}' \mathbf{U}'} = -\mu_t(\nabla \mathbf{U} + (\nabla \mathbf{U})^T) \tag{4.6}$$

where μ_t term represents the turbulent dynamic viscosity and is evaluated by the chosen turbulence model. By defining the effective dynamic viscosity as,

$$\mu^{eff} = \mu + \mu_t \tag{4.7}$$

the deviatoric viscous stress tensor and Reynolds stress tensor can be rearranged as,

$$\begin{aligned}\nabla \cdot (\tau - \mathbf{R}) &= \nabla \cdot [\mu^{eff}(\nabla \mathbf{U} + (\nabla \mathbf{U})^T)] \\ &= \nabla \cdot (\mu^{eff} \nabla \mathbf{U}) + \nabla \cdot [\mu^{eff}((\nabla \mathbf{U})^T - \frac{1}{3}\operatorname{tr}(\nabla \mathbf{U})^T \mathbf{I} + \frac{1}{3}\operatorname{tr}(\nabla \mathbf{U})^T \mathbf{I})] \\ &= \nabla \cdot (\mu^{eff} \nabla \mathbf{U}) + \nabla \cdot [\mu^{eff}(\operatorname{dev}(\nabla \mathbf{U})^T]\end{aligned} \tag{4.8}$$

where tr() means the trace of a matrix, defined to be the sum of the diagonal components of a matrix, $\mathbf{I}$ represents the identity tensor ($\mathbf{I} \equiv \delta_{ij}$) and dev() donates the deviatoric part of a matrix, i.e. for any matrix $\mathbf{A}$, dev($\mathbf{A}$) can be evaluated as,

$$\operatorname{dev}(\mathbf{A}) = \mathbf{A} - \frac{1}{3}\operatorname{tr}(\mathbf{A})\mathbf{I} \tag{4.9}$$

Note if the flow is assumed to be incompressible, the following relationship holds,

$$\nabla \cdot \mathbf{U} = \operatorname{tr}(\nabla \mathbf{U})\mathbf{I} = \operatorname{tr}(\nabla \mathbf{U})^T \mathbf{I} = 0 \tag{4.10}$$

Modified $k - \varepsilon$ Model

The nonlinear Reynolds stress term requires additional turbulence model to close the RANS equation. OpenFOAM supports several turbulence models, e.g. Spalart-Allmaras model, $k-\varepsilon$ model and $k-w$ model. The most common turbulence model, the $k - \varepsilon$ model, is used for this study. The $k - \varepsilon$ model implemented in interFoam solver is a modified version, it reads,

$$\frac{\partial \varepsilon}{\partial t} + \nabla \cdot (\mathbf{U}\varepsilon) - \nabla \cdot ((\frac{\nu_t}{\sigma_\varepsilon} + \nu)\nabla \varepsilon) = C_{\varepsilon 1}\frac{\varepsilon}{k}G - C_{\varepsilon 2}\frac{\varepsilon}{k}\varepsilon \tag{4.11}$$

$$\frac{\partial k}{\partial t} + \nabla \cdot (\mathbf{U}k) - \nabla \cdot ((\frac{\nu_t}{\sigma_k} + \nu)\nabla k) = G - \frac{\varepsilon}{k}k \tag{4.12}$$

where G is the production rate of kinetic energy due to the gradients in the resolved velocity field,

$$G = 2\nu_t |\frac{1}{2}(\nabla \mathbf{U} + (\nabla \mathbf{U})^T)|^2 \tag{4.13}$$

Comparing to the standard $k - \varepsilon$ model of LAUNDER and SPALDING [59], the density is not included in Equation 4.11 and Equation 4.12 but taking into account with the turbulent viscosity,

$$\mu_t = \rho \nu_t = \rho C_\mu \frac{k^2}{\varepsilon} \tag{4.14}$$

The model constants are,

$$C_{\varepsilon 1} = 1.44 \quad C_{\varepsilon 2} = 1.92 \quad C_{\mu} = 0.09 \quad \sigma_k = 1.0 \quad \sigma_{\varepsilon} = 1.3 \tag{4.15}$$

4.2.2 Modified VOF method

One of the critical issues in numerical simulations using the VOF method is the sharp resolution of the interface while preserving the boundedness and conservation of the phase fraction. This is especially in cases of flow with high density ratios such as air and water in the dam break wave, where small errors in volume fraction may lead to significant errors in calculations of physical properties. To overcome these difficulties, the VOF method was modified with the so-called surface compression approach. In the interFoam solver, the α-equation reads,

$$\frac{\partial \alpha}{\partial t} + \nabla \cdot (\mathbf{U}\alpha) + \nabla \cdot [\mathbf{U}_r \alpha(1-\alpha)] = 0 \tag{4.16}$$

where the phase fraction α is the indicator function defined in Equation 4.17 and $\mathbf{U}_r$ is an extra, artificial compression term introduced by RUSCHE [56], defined as the relative velocity between phase a and b (Equation 4.18).

$$\alpha = \begin{cases} 0, & \text{for points belonging to one phase;} \\ 0 < \alpha < 1, & \text{for points at the phase-interface;} \\ 1, & \text{for points belonging to another phase.} \end{cases} \tag{4.17}$$

$$\mathbf{U}_r = \mathbf{U}_a - \mathbf{U}_b \tag{4.18}$$

Using the indicator function, two immiscible fluids are considered as one effective fluid throughout the domain, the local density ρ and the local viscosity μ of the fluid are given by:

$$\rho = \alpha\rho_a + (1-\alpha)\rho_b \tag{4.19}$$

$$\mu = \alpha\mu_a + (1-\alpha)\mu_b \tag{4.20}$$

where the subscripts a and b denote the different fluids.

The role of the artificial term $\nabla \cdot [\mathbf{U}_r \alpha(1-\alpha)]$ is to compress the interface. Because of the multiplication term $\alpha(1-\alpha)$, the artificial term contributes only within the interface region and vanishes at both limits of the phase fraction. Therefore, it does not affect the solution significantly outside this region. As commented by RUSCHE

[56], the main advantage of such formulation lies in the higher interface resolution comparison with the conventional VOF approach. Numerical diffusion, unavoidably introduced through the discretization of convective terms, can be controlled and minimized through the discretization of the compression term, thus allowing sharp interface resolution. The other advantage is the boundedness, the solution of α is bounded between zero and one while the original VOF method of HIRT and NICHOLS [60] does not preserve local boundedness on the phase fraction.

Calculation of surface tension

Surface tension is a tensile force tangential to the interface separating the two fluids which tries to keep the fluid molecules at the free boundary in contact with the rest of the fluid. Accurate calculation of the phase fraction distribution is crucial for a proper evaluation of surface curvature, which is required for the determination of surface tension force and the corresponding pressure gradient across the free surface. To evaluate the surface tension force, the continuum surface force (CSF) model proposed by BRACKBILL *et al.* [61] is implemented. The CSF model is suitable for fixed Eulerian meshes and applies a volumetric force in those cells of the mesh containing the transitional interface region as an approximation to the discontinuous surface tension force. The surface tension force, appearing in the momentum expression(Equation 4.2) , is represented as

$$\mathbf{f}_\sigma = \sigma\kappa\nabla\alpha \tag{4.21}$$

where the mean curvature of the free surface κ is computed from local gradients in the surface normal at the interface,

$$\kappa = -\nabla \cdot (\frac{\nabla\alpha}{|\nabla\alpha|}) \tag{4.22}$$

4.2.3 Discretised model equations

The finite volume discretization in OpenFOAM of the temporal terms and spatial terms (convection term, diffusion term and source term) are described in detail by JASAK [62]. The solution domain is subdivided into a number of cells with computational points placed at the cell centroids. Each two cells share exactly one cell face, on which a surface normal vector $\mathbf{S}_f$ is defined, as shown in Figure 4.1.

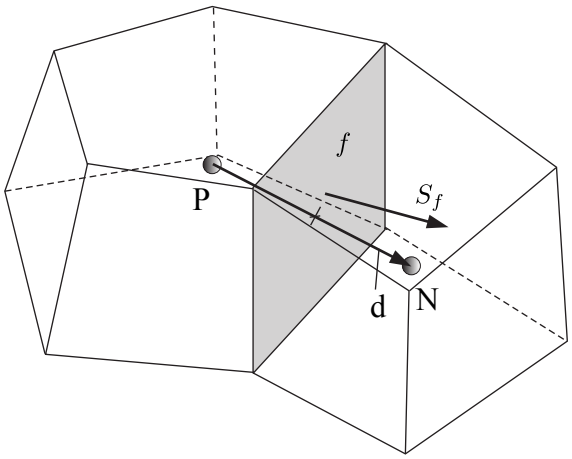

Figure 4.1: Discretization of the solution domain, adapted from GREENSHIELDS [63]

With Gausss theorem applied to the convective and diffusive terms and using the Euler implicit time scheme [1], the following discretized system of equations is derived,

$$\sum_f \mathbf{U}_f \cdot \mathbf{S}_f = 0 \tag{4.23}$$

$$\frac{\rho^n \mathbf{U}^n - \rho^o \mathbf{U}^o}{\Delta t} V_P + \sum_f \rho_f \phi \mathbf{U}_f^n - \sum_f \mu_f^{eff} \mathbf{S}_f \cdot \nabla_f \mathbf{U}^n - \sum_f \mu_f^{eff} (\mathrm{dev}(\nabla \mathbf{U}^o)^T)_f \cdot \mathbf{S}_f = \sum_f [\nabla_f \mathbf{p}_{rgh} - g \mathbf{X}_f \nabla_f \rho + (\sigma\kappa)_f \nabla_f \alpha] |\mathbf{S}_f| \tag{4.24}$$

$$\frac{\alpha^n - \alpha^o}{\Delta t} V_P + \sum_f \alpha_f \phi + \sum_f \phi_r \alpha_f (1-\alpha)_f = 0 \tag{4.25}$$

where V_P represents the control volume, subscript $()_f$ implies the value of the variable in the middle of the face, superscript $()^n$ denotes the current (new) time step, superscript $()^o$ denotes the previous (old) time step and operator ∇_f denotes a discretized gradient at the face,

$$\nabla_f \mathbf{U}^n = (\nabla \mathbf{U}^n)_f = \frac{\mathbf{U}_N^n - \mathbf{U}_P^n}{|d|} \tag{4.26}$$

where subscript $()_P$ indicates the value in the current cell and subscript $()_N$ indicates the value in the neighbour cell, and ϕ is surface velocity flux,

$$\phi = \mathbf{U}_f \cdot \mathbf{S}_f \tag{4.27}$$

[1] This time scheme is used for the demonstration of the discretization process; for the simulations later on, the CrankNicolson time scheme is used.

4.2.4 Pressure-velocity coupling

The pressure-velocity coupling is solved with the so-called PIMPLE algorithm. PIMPLE is a merged algorithm of Pressure Implicit Splitting Operator (PISO) and Semi-Implicit Method for Pressure-Linked Equations (SIMPLE). Its main structure is inherited from the original PISO, but it allows equation under-relaxation to ensure the convergence of all the equations at each time step. A detailed description of the SIMPLE and PISO algorithm can be found in FERZIGER and PERIĆ [64] and ISSA [65], respectively.

Momentum predictor

The left hand side (LHS) of Equation 4.24 is assembled and called UEqn in the interFoam solver.

$$\text{UEqn:} \quad \frac{\rho^n \mathbf{U}^n - \rho^o \mathbf{U}^o}{\Delta t} V_P + \sum_f \rho_f \phi \mathbf{U}_f^n - \sum_f \mu_f^{eff} \cdot \nabla_f \mathbf{U}^n - \sum_f \mu_f^{eff} (\text{dev}(\nabla \mathbf{U}^o)^T)_f \cdot \mathbf{S}_f \tag{4.28}$$

The UEqn could be assembled in solution vector form as $\mathbf{A}\mathbf{U}^n = \mathbf{b}$, with $\mathbf{A}$ being the momentum coefficient matrix, $\mathbf{U}^n$ the unknown velocity vectors and $\mathbf{b}$ the vector containing the source terms. The following operators acting on the UEqn can be defined and are implemented in OpenFOAM: the D-operator $\mathbf{A_D}$ gives the diagonal part of matrix $\mathbf{A}$, the N-operator $\mathbf{A_N}$ represents the off-diagonal part of matrix $\mathbf{A}$, the S-operator $\mathbf{A_S}$ extracts the source vector $\mathbf{b}$. With these operators, the UEqn becomes,

$$(\mathbf{A_D} + \mathbf{A_N})\mathbf{U}^n = \mathbf{A_S} \tag{4.29}$$

Equation 4.24 can then be rewritten in a semi-discretized form,

$$(\mathbf{A_D} + \mathbf{A_N})\mathbf{U}^n = \mathbf{A_S} - \nabla \mathbf{p}_{rgh}^o - g\mathbf{X}_f \nabla \rho + \sigma \kappa \nabla \alpha \tag{4.30}$$

Since the exact pressure gradient is not known, the old pressure filed ($\mathbf{p}_{rgh}^o$) from the previous step is used to predict the velocity $\mathbf{U}^n$. It should be noted that doing a momentum predictor is not an essential step for the convergence of the PISO pressure corrector loop although it is sometimes benefitial but not always. Therefore in interFoam solver the momentum predictor is optional by setting indicator *momentumPredictor* to yes or no.

Pressure corrector

The first corrected velocity $\mathbf{U}^*$ is being solved from the predicted velocity $\mathbf{U}^n$ and the first corrected pressure $\mathbf{p}^*_{rgh}$.

$$\mathbf{A_D}\mathbf{U}^* + \mathbf{A_N}\mathbf{U}^n = \mathbf{A_S} - \nabla\mathbf{p}^*_{rgh} - g\mathbf{X}_f\nabla\rho + \sigma\kappa\nabla\alpha \tag{4.31}$$

The problem is that the corrected pressure is yet unknown - all that known is the old pressure. To obtain the corrected pressure, introducing,

$$\mathbf{A_H} = \mathbf{A_S} - \mathbf{A_N}\mathbf{U}^n \tag{4.32}$$

By inverting $\mathbf{A_D}$, Equation 4.31 becomes,

$$\mathbf{U}^* = \mathbf{A_D}^{-1}\mathbf{A_H} - \mathbf{A_D}^{-1}\nabla\mathbf{p}^*_{rgh} + \mathbf{A_D}^{-1}(-g\mathbf{X}_f\nabla\rho + \sigma\kappa\nabla\alpha) \tag{4.33}$$

This will be used later to calculate the face fluxes. By replacing Equation 4.33 in the continuity equation, the Pressure Poisson Equation of the first corrected pressure $\mathbf{p}^*_{rgh}$ can be written as:

$$\nabla\cdot(\mathbf{A_D}^{-1}\nabla\mathbf{p}^*_{rgh}) = \nabla\cdot(\mathbf{A_D}^{-1}\mathbf{A_H} + \mathbf{A_D}^{-1}(-g\mathbf{X}_f\nabla\rho + \sigma\kappa\nabla\alpha)) \tag{4.34}$$

Further pressure correction steps can be applied using the same $\mathbf{A_D}$ matrix and $\mathbf{A_H}$ vector. This is convenient computationally since they can be stored in memory and recalled as necessary. It should be noted that although it is possible to recalculate the coefficients in $\mathbf{A_H}$ after each pressure solution, it is not done in interFoam. According to JASAK [62], the non-linear coupling is less important than the pressure-velocity coupling. The coefficients in $\mathbf{A_H}$ are therefore kept constant through the whole correction sequence and will be changed only in the next momentum predictor.

Extra flux correction term

It is not guaranteed that the implementation of the solvers in any CFD code, including OpenFOAM, is faithful to the original theory behind the algorithms. As in all CFD codes, the implementation may have some extra artificial terms to improve some features such as stability robustness. In commercial solvers such modifications are kept in the black box and cannot be tracked but in open source codes the code are free for evaluation. In the following we briefly discuss one special flux correction term in the implementation of PISO algorithm.

Taking a further look at the solver code, it reveals that in the pressure correction

loop of time step n the mass flux is of the form

$$\phi^n_{PISO} = \phi + \phi_c \tag{4.35}$$

The first term is the standard velocity flux defined in Equation 4.27 and the second term ϕ_c is the extra correction term. This extra term is specific to OpenFOAM and it is not a part of the original PISO implementation of ISSA [65]. The implementation of ϕ_c in OpenFOAM is formulated as,

$$\phi_c = \frac{K_c}{\Delta t}(\mathbf{A_D}^{-1})_f[\phi^o_{PISO} - (U^o)_f \cdot \mathbf{S}_f] \tag{4.36}$$

where the correction coefficient ($0 \leq K_c \leq 1$) is evaluated as follows,

$$K_c = 1 - min(\frac{|\phi^o_{PISO} - (U^o)_f \cdot \mathbf{S}_f|}{|\phi^o_{PISO}| + \epsilon}, 1) \tag{4.37}$$

where ϵ is a very small number to avoid division by zero.

It seems ϕ_c may affect the divergence of the face velocity since the interpolated velocity becomes subtracted from the flux. However, to the best of our knowledge, the influence of this extra flux correction term is not documented yet and requires further investigation.

4.3 Validation of the solver

As mentioned in the previous sections, the interFoam solver include many specific modifications. To validate the solver, a dam break case is set up with results compared to experimental data available from LOBOVSKỲ *et al.* [32].

The computation domain is shown in Fig. 4.2 based on the setup of LOBOVSKỲ *et al.* [32]. The length of the upstream reservoir between the dam gate and the left wall equals 600 mm and the downstream channel length is 1010 mm. Four pressure sensors $P1$ to $P4$ are located in the right wall, with different heights 3, 15, 30 and 80 mm.

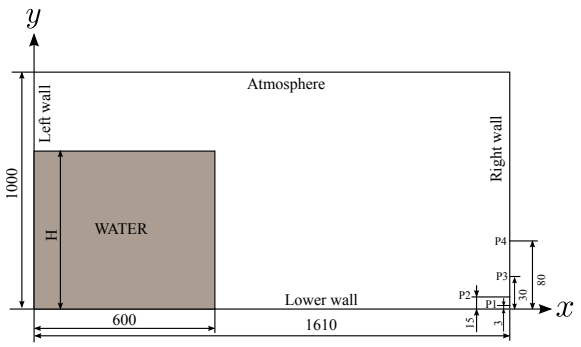

Figure 4.2: Schematic of dam break model,in units: mm, adapted from LOBOVSKỲ *et al.* [32]

The initial condition is set to be zero for all velocity components and the modified pressure. The boundary is defined in two groups: the walls and the atmosphere. The no-slip boundary condition is specified for all the walls ; the boundary conditions for the turbulence kinetic energy k and its dissipation rate ε are specified with the aid of the technique of wall functions. For the atmosphere, the zero values for the pressure, water volume fraction and all velocity components are also specified.

The OpenFOAM utility blockMesh is used to discretize the computation domain as hexahedral blocks. For the simulation a uniform mesh with $Ds = \Delta x = \Delta y = \Delta z$ is adopted. The feature of "adjustable run-time" available in interFoam is used with the maximum CFL number set to be 0.25.

The discretization schemes used in the interFoam solver is shown in Table 4.1. The "Gauss" keyword specifies the standard finite volume discretization of Gaussian integration. TVD stands for total variation diminishing scheme and CD is short for central differencing scheme. The symbol $*$ stands for an arbitrary scalar or vector.

Table 4.1: The discretization schemes of interFoam

Category	Term	Discretization schemes	Note
Temporal	$\frac{\partial}{\partial t}*$	Euler	Euler Implict
Divergence	$\nabla \cdot (\rho \mathbf{U}\mathbf{U})$	Gauss linearUpwind	Linear upwind differencing
	$\nabla \cdot (\mu^{eff} \operatorname{dev}(\nabla \mathbf{U})^T)$	Gauss linear	Linear interpolation (CD)
	$\nabla \cdot (\mathbf{U}\alpha)$	Gauss vanLeer	TVD van Leer limiter
	$\nabla \cdot [\mathbf{U}_r \alpha(1-\alpha)]$	Gauss linear	CD
Laplacian	$\nabla \cdot (\mu^{eff} \nabla \mathbf{U})$	Gauss linear corrected	CD
	$\nabla \cdot ((\frac{\nu_t}{\sigma_\varepsilon} + \nu)\nabla \varepsilon)$		with Explicit correction
	$\nabla \cdot ((\frac{\nu_t}{\sigma_k} + \nu)\nabla k)$		on non-orthogonal meshes
Gradient	$\nabla *$	Gauss linear	CD
Surface Normal Gradient	$(\nabla *)_f$	corrected	Explicit correction on non-orthogonal meshes

The simulation results of case $H = 600$ mm is shown in Figure 4.3. To evaluate the influence of the mesh size, three different mesh size $DS = 20, 10, 5$ mm is used. It is observed from the comparison with the experimental data (the solid line) in Figure 4.3, the agreement of the pressure the signal for all pressure sensors $P1$ to $P4$ is good.

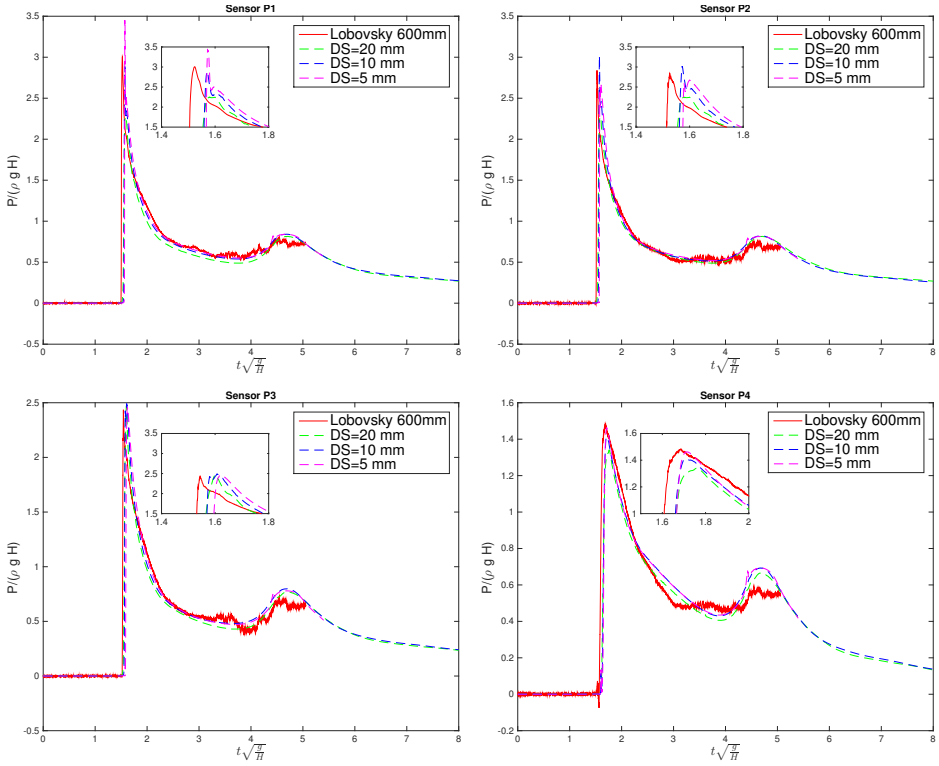

Figure 4.3: Results of pressure comparing to experimental data

4.3.1 Grid convergence

According to ROACHE [66, 67], the grid-convergence index (GCI) presents a simple method for uniform reporting of grid-convergence studies. The GCI is based on the Richardson Extrapolation (RICHARDSON and GAUNT [68]), which is a method for obtaining a higher-order estimate of the continuum value (value at zero grid spacing) from a series of lower-order discrete values $(f_1, f_2, ..., f_n)$. Using the grid refinement ratio r, ROACHE [66] generalized Richardson extrapolation by introducing the p^{th}-order methods:

$$f_{exact} \approx f_1 + (f_1 - f_2)(r^p - 1) \tag{4.38}$$

and the order-of-accuracy can be estimated by using the following equation:

$$p = \frac{\ln(\varepsilon_{32})/\ln(\varepsilon_{21})}{\ln(r)} \tag{4.39}$$

$$\varepsilon_{i+1,i} = f_{i+1} - f_i \tag{4.40}$$

where f_{i+1} is a coarse-grid numerical solution and f_i is a fine-grid numerical solution. Then the GCI for the fine grid solution can be written as:

$$GCI_{i+1,i} = Fs * |\frac{\varepsilon_{i+1,i}}{1 - r^p}| \tag{4.41}$$

where Fs is the safety factor, following ROACHE [66], the safety factor selected for this study is 3.

According to STERN *et al.* [69], the possible convergence conditions of the system are: 1) monotonic convergence ($0 < R < 1$); 2) oscillatory convergence ($R < 0$); 3) divergence($R > 1$). And R is the convergence ratio and it is determined by the equation:

$$R = \frac{\varepsilon_{21}}{\varepsilon_{32}} \tag{4.42}$$

The order of accuracy and the GCI for the impact peak pressure for all pressure sensors (p_1, p_2, p_3 and p_4) from the simulation results of three grids ($DS = 20, 10, 5$ mm) are summarized in Table 4.2.

Table 4.2: Order of accuracy and Grid Convergence Index for three integration variables. Subscripts 3, 2 and 1 represent case $DS = 20, 10, 5$ mm, respectively.

	ε_{32}	ε_{21}	R	p	GCI_{32}	GCI_{21}
p_1	0.634	0.565	0.891	0.166	15.574	13.879
p_2	0.765	0.339	0.443	1.174	1.826	0.809
p_3	0.036	0.020	0.556	0.848	0.135	0.075
p_4	0.068	0.054	0.794	0.332	0.787	0.624

As listed in Table 4.2, there is a reduction GCI value for the successive grid refinements ($GCI_{21} < GCI_{32}$). The GCI for finer grid (GCI_{21}) is relatively low if compared to the coarser grid (GCI_{32}), indicating that the dependency of the numerical simulation on the cell size has been reduced. Additionally, the convergence ratios R for all pressure sensors (p_1 to p_4) are less than one, according to STERN *et al.* [69], the convergence conditions are monotonic.

Chapter 5

Dam Break Experiments

This chapter is structured as follows. The general experiment setup would be given first. All devices used for data acquisition would be described in detail later. Finally, the test cases are included.

5.1 Experiment setup

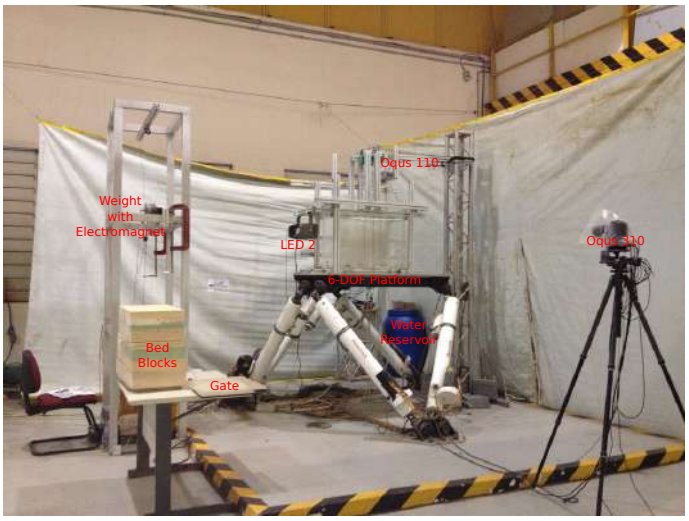

Figure 5.1: Experimental setup, overall view

The experiment setup was built and installed in the LabOceano facility. Fig. 5.1 shows an overall view of whole setup. It consists of an acrylic tank divided into two separate parts by a removable gate and a gate release system. The tank is installed on the 6-DOF platform available in the laboratory which guarantees a horizontal tank bottom. The detailed setup is shown in Fig. 5.2, including all recording equipments. All parts of the setup are further explained hereafter.

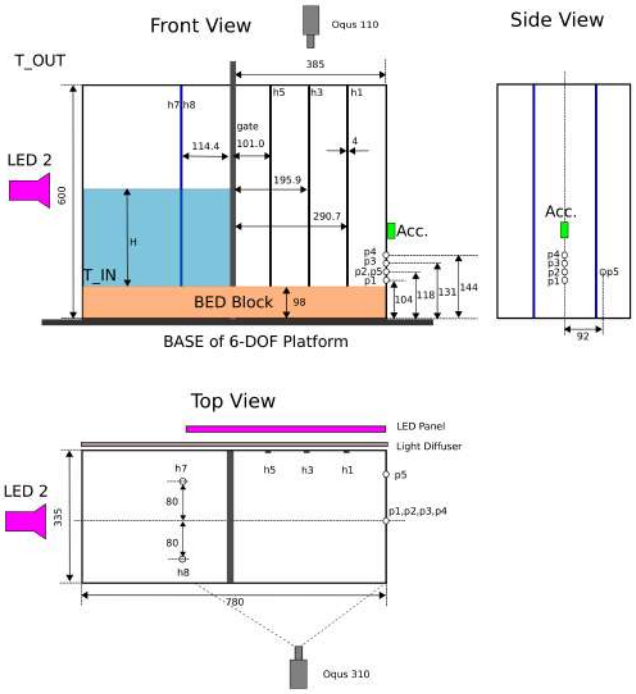

Figure 5.2: Experimental setup of the dam-break tests

5.2 Tank and gate release system

The tank is made of 15 mm thick acrylic with inner dimensions of $780 \times 335 \times 600$ mm. The angular deviation of the bottom of tank is 0.12 degree and 0.15 degree in the x and y directions respectively. A 10 mm thick acrylic dam gate is placed 385 mm from the lateral side of the tank. This defined the dam reservoir region (upstream) and the channel region (downstream).

One challenge of dam break experiment is the water-tightness of the dam gate. The dam gate should be watertight but also be removable. In this study, the Ethylene-vinyl acetate (EVA) foam is used at the bottom side and lateral side of the gate. To decrease the friction , the lateral side of dam gate is smeared with silicone grease.

As shown in Fig. 5.3, the gate release mechanism consists of two fixed pulleys, an electromagnet and a 10 kg releasing mass with a damping reservoir half filled with sand. This arrangement was similar to the release mechanism used by STANSBY *et al.* [12] and LOBOVSKỲ *et al.* [32]. To control the gate releasing, an electromagnet was used and controlled by a global TTL trigger signal. Once the global TTL trigger signal was set to logic level LOW, the 10 kg mass was dropped under gravity releasing the gate and starting video acquisition. The distance between the electromagnet and the damping reservoir was 1.1 m. The weight falls freely a distance of 0.6 m, reaching a velocity about 2-3 m/s. This arrangement

is to achieve the so-called "sudden dam break", as demonstrated in LAUBER and HAGER [17]: the nondimensional gate removal period is smaller than $t\sqrt{\frac{g}{H}} = \sqrt{2}$, with g = gravitational acceleration, H = initial water depth and t = time.

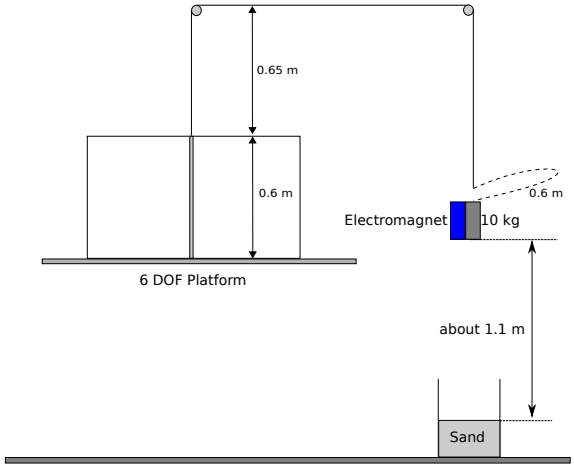

Figure 5.3: Schematic view of the gate release system

5.3 Data acquisition and synchronization

The data acquisition flow chart is shown in Fig. 5.4. A global TTL trigger signal is used to set the time origin ($t = 0$). It allows all measured variables with synchronized records related to the same time base.

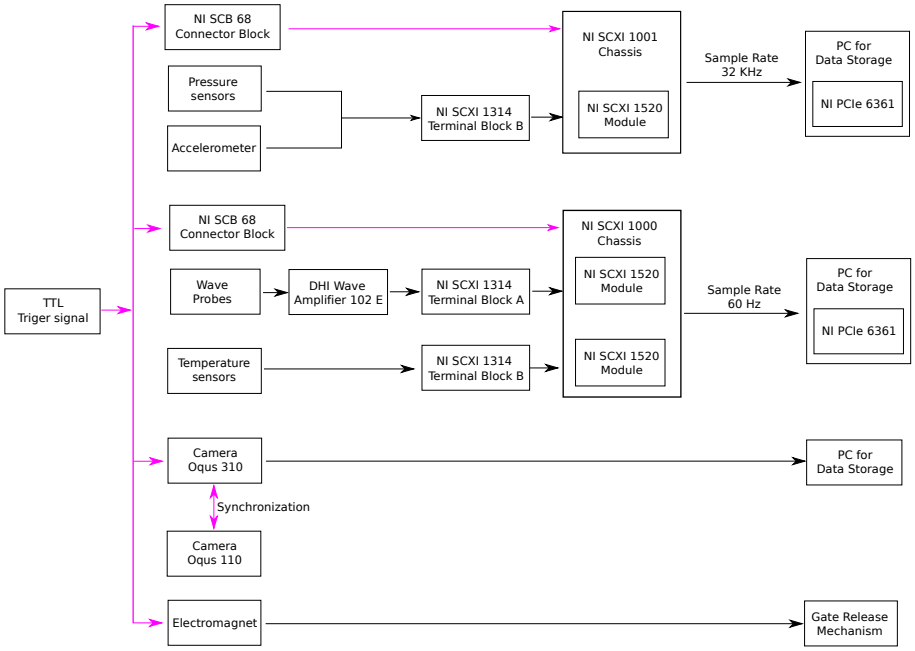

Figure 5.4: Data acquisition Flow

Considering the requirements in capturing different sensor signals, e.g. pressure sensors and wave probes, are different, two different sample rate are used. The

higher sample rate of 32 KHz is applied for pressure sensors and accelerometer and the lower sample rate of 60 Hz is applied for wave probes and temperature sensors. The choice of higher sample rate is based on the pressure nature frequency, which would be described in the Section 5.3.2.

For the video recording, the global TTL trigger signal is set as the external trigger signal of the Qualisys Track Manager (QTM) software. The synchronization between camera Oqus 310 and camera Oqus 110 is controlled by the QTM software with the internal time clock.

5.3.1 Wave probes

The wave probe comprises two thin, parallel 316L stainless steel electrodes. When immersed in water, the wave probes measure the conductivity of the instantaneous water volume between the two electrodes, a conductivity that changes proportionally to changes of the water surface elevation, i.e. the wave height, between the electrodes.

The conductance, G, between two parallel electrodes is determined as:

$$G = C_w l \frac{\pi}{\ln \frac{2D}{d}} \tag{5.1}$$

where C_w is the conductivity of the water, l donates the length of immersed part of the electrodes, d is the diameter of the electrodes and D is the distance between the electrodes (center to center). In the present work, $d = 2.3$ mm and $D = 8.0$ mm.

The DHI Wave Amplifier 102E is used for data acquisition. To outbalance the influence of temperature or salinity changes of the water, the compensation is set manually inside the DHI Wave Amplifier based on the water conductivity. The water conductivity is 850 μS/cm, measured by the TDS&EC conductivity meter with an accuracy of 2%.

The wave probe locations are specified in Fig. 5.2. This arrangement make it possible to do a comparison of the new data with previously published researches, such as BUCHNER [6], LEE *et al.* [70] and LOBOVSKỲ *et al.* [32].

In the upstream, two wave probes (h7, h8) are used to measure the water elevation. Probes are mounted in pair outside the center line to observe the three-dimensional effects in the flow. In the downstream, initially six wave probes (h1 to h6) were used. However, the Reynolds number of the downstream flow reaches $Re = \frac{2\sqrt{gH}D}{\nu} \approx 6.7E3$, with water depth $H = 0.2$ m and wave probe diameter $D =$ 2.4 mm. The Reynolds number is so high that unwanted turbulence wake vortex is found as shown in Fig. 5.5.

Figure 5.5: Downsteam turbulence

One may use smaller wave probes or change the water viscosity to reduce the Reynolds number. Considering the limited resources available in laboratory, we overcome this difficulty in the other way, measuring the water elevation indirectly. T

hree thin black plastic markers are used in the downstream instead of the real conductive wave probe. They are called as virtual wave probes (h1 , h3 and h5). The time history of water free surface elevation is evaluated by imaging analysis from captured video images. The algorithm of elevation detection is included in Appendix C.1.

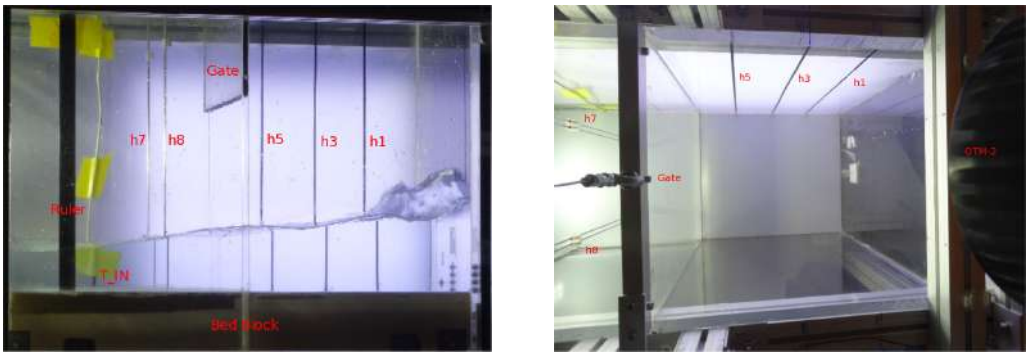

(a) front view (b) top view

Figure 5.6: Wave probes and virtual wave probes

5.3.2 Pressure sensor

At the downstream side, five pressure sensors are used to measure the impact pressure. Sensor p1, p2, p3 and p4 are located in the centerline while sensor p5 is

located outside the center-line but with the same height level of sensor p2, as shown in Fig. 5.2. This arrangement allows to observe the three-dimensional effects. The sensor positions are set near the bottom side of the tank right wall, because the peak pressure occurs at the bottom side.

The requirement for the pressure sensors is special. The sensors need to be as small as possible, operate in a large range of pressure magnitudes, possess a good resolution and be capable of measuring in two phases flows. There are various types of pressure-sensing technologies, such as piezoresistive, capacitive, electromagnetic, piezoelectric, optical, and potentiometric types. For impact pressure of green water or sloshing phenomenon, piezoresistive and piezoelectric type of sensor are mainly applied. The instruments available in laboratory are the EPX Miniature pressure sensor produced by Measurement Specialties Inc. It is a piezoresistive type pressure sensor, with a range of 7 bar and a diameter of the head of 5 mm. The specifications are shown in Table 5.1. Following SOUTO-IGLESIAS *et al.* [71], with our experimental capabilities, the bias uncertainty in the pressure measurements is about 10 milibar.

Table 5.1: Specifications of EPX sensor

Description	Value	Units
Pressure range	0-7	bar
Resonant frequency	80	KHz
Thermal Zero Shift	$\pm$1.5%	FSO / 50 °C
Sensing area diameter	5	mm
Operating Temperature	-40 to 120	°C

It should be noted that the useful frequency (the frequency response limit) of the sensor is about 20 % of the resonant frequency, that is 16 KHz. According to the Nyquist Shannon sampling theorem, the sampling rate should be chosen as twice of the highest frequency component, that is 32 KHz. The pressure sensors should be mounted carefully to avoid anomalous behavior that could be attributed to the mounting. On one hand the so-called flush mount is required which means that the membrane surface of the pressure sensor is as coincidence as possible with the surface of the test object. On the other hand, the installation torque might affect also. Excessive torque may change zero offset. In such cases, output should be re-zeroed through instrumentation.

5.3.3 Temperature sensors

To evaluate the temperature shock effect for the pressure sensors, two LM35 Precision Centigrade Temperature Sensor T_IN and T_OUT are used. As shown in Fig. 5.2, sensor T_IN is located inside the tank under the water to measure the water temperature and sensor T_OUT is located outside the tank to measure the environment air temperature.

The LM35 series are precision integrated-circuit temperature devices with an output voltage linearly proportional to the Centigrade temperature. The LM35 device does not require any external calibration or trimming to provide typical accuracy of $\pm 0.25\,^{\circ}\mathrm{C}$ at room temperature.

5.3.4 Accelerometer

Acceleration during the test may also affect the quality of the results. For instance, vibration induced by the friction between the dam gate and tank wall may affect the pressure measurement. To evaluate the possible acceleration effects, one MEMS accelerometer Model 4803A is installed on the downstream side wall.

The Model 4803A is an tri-axial accelerometer in a rugged, welded stainless steel package. It incorporates integral temperature compensation that provides a stable output over a wide temperature range from -55° to +125°. The acceleration range is $\pm 2g$.

5.3.5 Video recording and illumination

Two high-speed digital cameras Oqus 310 and Oqus 110 are used for observing the dam break flow motion. The Qualisys Track Manager (QTM) software is used for the acquisition of the high-speed videos. The field of view of camera Oqus 310 is mainly on the downstream side to capture more details of the dispersed phase of the dam break flow. Camera Oqus 110 is set at the top side of the tank to observe the three dimensional effects of the flow. The camera properties are shown in Table 5.2.

Table 5.2: Camera properties

Camera Type	Oqus 310	Oqus 110
Resolution	1280 × 1024	640 × 480
Aperture Number	2.0	1.5
Focal Length (mm)	105	8.5
Sensor Type	CMOS	CMOS
Sensor Size (mm)	6.3 × 4.7	17.9 × 14.3
Max FPS	502	247
Used FPS	500	200

For illumination, the so-called shadowgraphy technique is applied. The LED panel with dimension 500×400 mm is chosen as the light source due to the following two advantages: firstly comparing to AC powered 600 W light bulbs used in RYU *et al.* [15] or the halogen lights used in CHENG *et al.* [72], the DC powered LED panel does not have the light flicker effect and have less light fluctuation; secondly the light density distribution of the LED panel is much more uniform. To improve the light density uniformity, a light diffuser is set at the back side of the tank, as shown in Fig. 5.2.

5.4 Test cases

To study the effects of the bed slopes, five different slope bed blocks were built and would be placed at the bottom of the tank, as shown in Fig. 5.7 and Table 5.3. The height of downstream side for all the blocks are the same, equal to 98 mm, while the height of the upstream side varies for different angles.

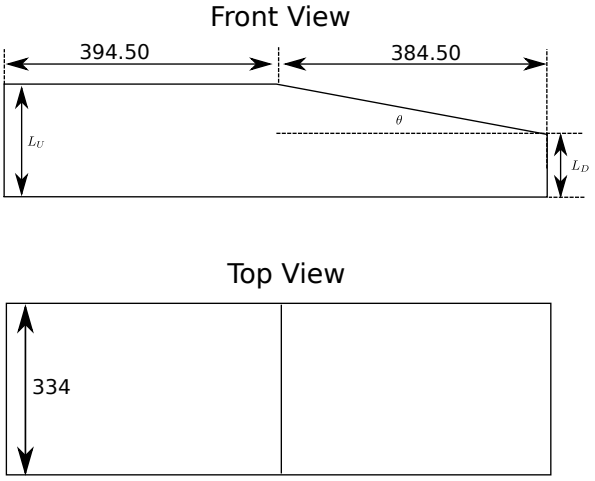

Figure 5.7: Sketch of the slope bed blocks

Table 5.3: Slope bed blocks and test cases

Block Name	L_U (mm)	L_D (mm)	θ (degree)	H (mm)
Flat	98	98	0	110, 220
5A	132	98	5	110, 220
5B	64	98	-5	110, 220
10A	166	98	10	110, 220
10B	30	98	-10	110, 220

For each block, two different water level cases are tested, including a lower water level case with $H = 110$ mm and a higher water level case with $H = 220$ mm. Therefore, totally ten cases are tested. Each case is repeated ten times.

Chapter 6

Results of Dam Break Models

After the gate releasing, the dam break wave is advancing on the channel and later impacting on the wall and reflecting backward. The whole dam break period can be divided into three main different periods, named as: the main period, the impact period, and the reflection period.

The main period lasts until the impact happens. Since the analytical dam break solutions work only in the main period, this period is in the mainly focus. In this period, we evaluate the dam break wave free surface profile by comparing the results of analytical solutions, numerical simulations, and experimental data. The "sudden dam break" concept is also investigated.

After the main period, the downstream dam break wave is impacting on the tank wall and running up along the wall, named as the impact period. In the impact period, the pressure is the main topic. Finally, a reflection wave is generated and propagated backward, called as the reflection period. This period is less relevant to the green water problem.

6.1 Main period with Stoker solutions

In the present section, we compare the free surface profile for the horizontal bed case of $H = 110$ mm. The results of both analytical solutions and numerical results are plotted over the experimental images as shown in Fig. 6.1, where the solid line is the ESS, the dotted line represents the LSS, the dots are the simulation results obtained with OpenFOAM and the dashed line indicates the initial dam. The OpenFOAM simulation results are not extracted from a cut plane but the projection of all points in the X-Z plane, as shown in Fig. 6.2a and Fig. 6.2b. The coordinate system is transformed from the world (in units mm) to image (in units pixel) based on the camera calibration data.

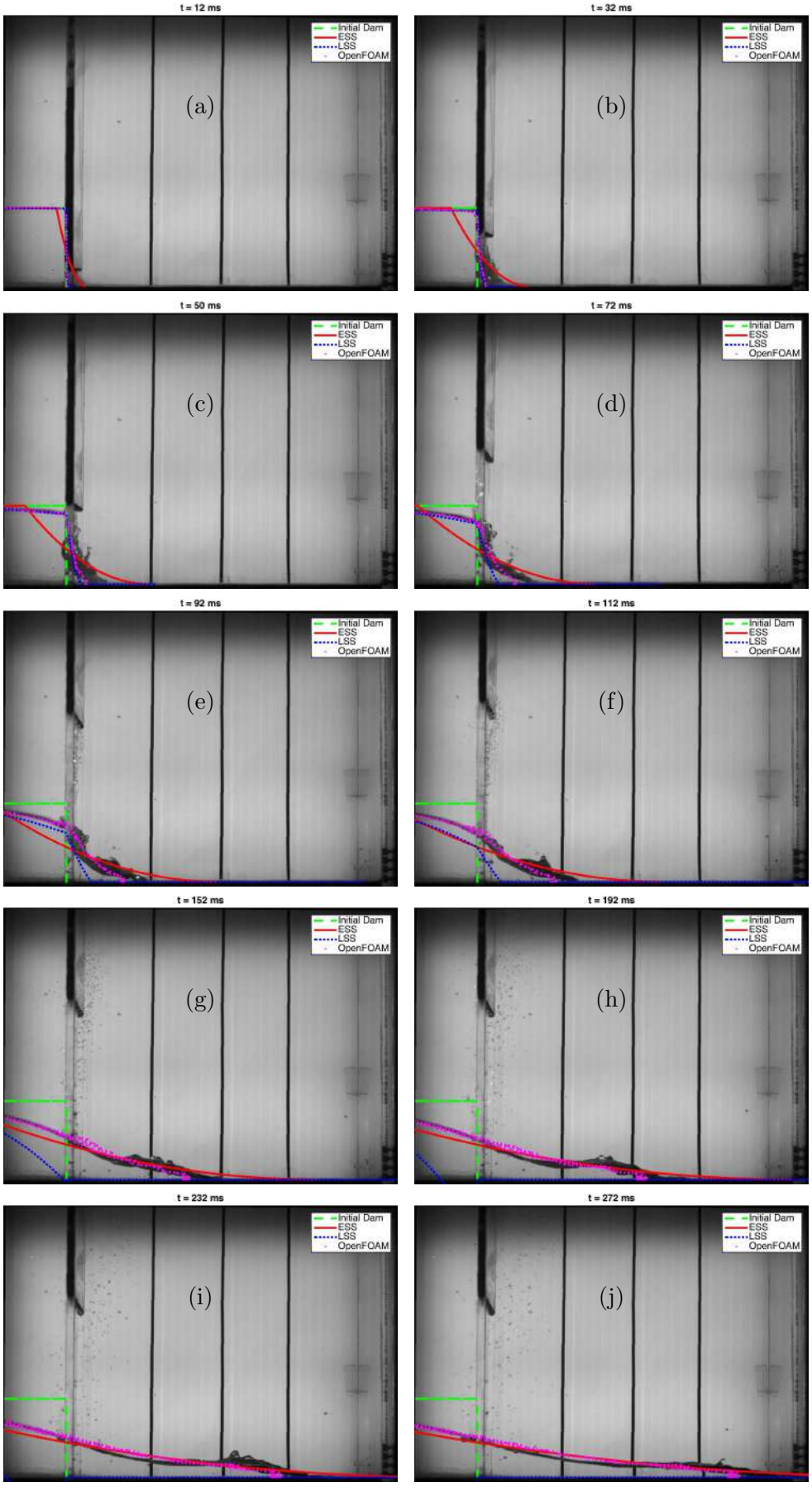

Figure 6.1: H=110 mm, evaluation of free surface profile

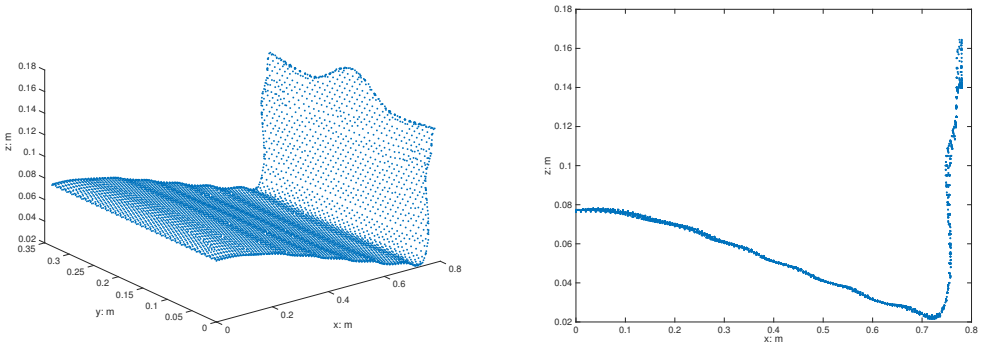

(a) free surface profile in 3D

(b) free surface profile projected in X-Z plane

Figure 6.2: OpenFOAM free surface profile

In general, the comparison between numerical results and experimental data shows a very good agreement on the free surface profile. On the other hand, based on agreement between the analytical solutions and the experimental data, the main period can be divided into three stages. Theses stages are named as: the gate releasing stage (Fig. 6.1a to Fig. 6.1c), the transition stage (Fig. 6.1d to Fig. 6.1f) and the later stage (Fig. 6.1g to Fig. 6.1j).

The first gate releasing stage is defined from the initial instant ($t = 0$) until the instant when the gate displacement is equal to the initial water level (H). At this position, the gate has no more influence in the flow. We name this instant as t_g. This interval can be associated with the gate removal period defined by LAUBER and HAGER [17]. They proposed that this period in non-dimensional form should be smaller than $\sqrt{2}$ for the flow to be considered as a sudden dam break.

From Fig. 6.1c, this instant can be estimated as $t_g = 50$ ms. In dimensionless form ($t_g^* = t_g\sqrt{g/H}$), it corresponds to 0.47, which is almost one third of $\sqrt{2}$. Following LAUBER and HAGER [17], the present case ($H = 110$ mm) can be considered as a "sudden dam break".

Comparing the analytical solutions to the experimental data, it is possible to observe that the LSS agrees quite well in both upstream and downstream side of the gate. On the other hand, the ESS overestimates the position of the wave front on both sides of the dam gate.

Following the gate releasing stage is the transition stage, defined from the end of the releasing stage (t_g) to the instant when ESS and LSS have an intersection point at the dam gate section. We name this instant as t_1. The intersection point can be estimated from the ESS. As mentioned in Section 3.1.1, the water level at the dam section is constant and equals to $\frac{4H}{9}$. Therefore the intersection point of the two solutions occurs at $(0, \frac{4}{9}H)$. Knowing where the intersection occurs we can

find now the instant t_1.

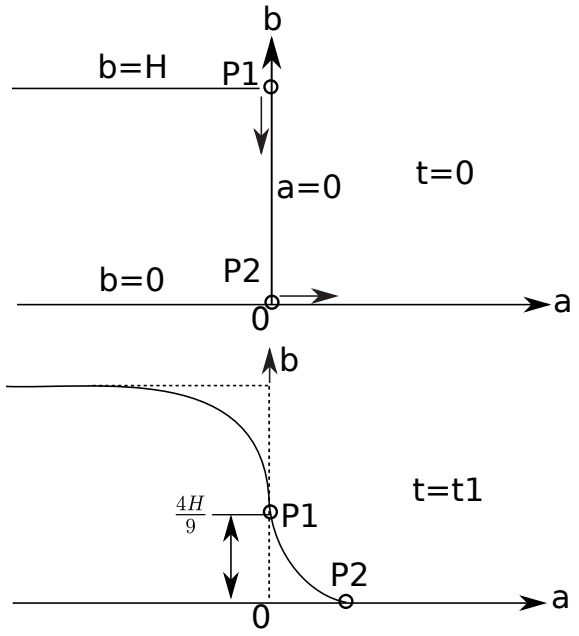

Figure 6.3: Sketch of the initial stage of the dam break problem with top particle P_1 and bottom particle P_2 at the dam gate section

In the Lagrangian representation, the dam can be represented by the points P_1 and P_2 shown in Fig. 6.3. Initially, both particles are at rest. The position of P_1 is defined as $X(0, H; 0) = 0$ and $Y(0, H; 0) = H$; while for P_2 is $X(0, 0; 0) = 0$ and $Y(0, 0; 0) = 0$. From the bottom boundary condition ($b = 0$) described in Section 3.1.2, particle P_2 would move only in the horizontal direction. On the other hand, with the boundary conditions at the dam section ($a = 0$), we have $X^{(2)}_{P_1} = 0$ and $Y^{(2)}_{P_1} = -\frac{g}{2}$, which indicates that particle P_1 would move only in the vertical direction. At instant $t = t_1$, particle P_1 reaches to position $(0, \frac{4H}{9})$. By representing the Y_{P_1} in power series, we have:

$$Y_{P_1} = H - \frac{g}{2}{t_1}^2 = \frac{4H}{9} \tag{6.1}$$

Solving Eq. (6.1), we obtain the instant t_1 equals to $\frac{\sqrt{10}}{3}\sqrt{\frac{H}{g}}$ and in dimensionless form $t_1^* = \frac{\sqrt{10}}{3}$. For the case of $H = 110$ mm, t_1 corresponds to 111.7 ms. This value is almost twice of the gate removal period. From Fig. 6.1f, we can observe that the ESS and LSS cross the intersection point at the instant 112 ms. This agrees with our results quite well.

In the transition stage, the agreement with experimental data of LSS is still better than ESS in the upstream side; while for the downstream side, both solutions have a poor agreement. It is observed that ESS overestimates the wave front location; while for LSS, one may observe the wave front location is underestimated

but with many particles (represented by dots) propagating far away on the bottom. This nonphysical behavior seems to be related to the limitations in LSS. Firstly, by inspecting Eq. (3.17a), there is a logarithmic singularity for particle P_2 ($a = 0$, $b = 0$) in $X^{(2)}$. Secondly, since $Y^{(2)}$ is always negative, the displacement Y would be negative as time t increases. Although with the bottom boundary condition (3.14), the particles are forced to contact with the bottom.

The last stage, named as the "later stage", occurs for time greater than t_1. In the later stage, it is observed that as time increases, the curve of LSS falls down rapidly and finally almost vanished. On the other hand, as time increases, the agreement of ESS with experimental data gets much better except the wave front region where the bottom friction can not be ignored anymore. However, the bottom friction effects of the dam break problem are out of the scope of the present paper, for the reader who has interest in this topic is referred to the work of DRESSLER [51] and WHITHAM [18].

Physically, if we consider particle P_1, it may be explained as follows. Initially, by neglecting the friction of the dam gate, particle P_1 behaves as free fall under the influence of gravity. The free fall velocity of particle P_1 is $v(t) = gt$ and the free fall distance $s(t) = \frac{1}{2}gt^2$. At time $t = t_1$, the fall distance $s(t_1) = \frac{5H}{9}$. This gravitational potential energy would be changed into kinetic energy in both horizontal direction and vertical direction. One may find in ESS, only the horizontal velocity component is considered. On the other hand, in LSS, due to the boundary condition $X^{(2)}_{P_1} = 0$, the horizontal velocity component of P_1 is zero, only the vertical velocity component is given. Both solutions have its own limitations. As can be observed, during the gate releasing stage and the transition stage ($t < t_1$), the vertical movement is dominant. In this period, the free fall assumption seems to be valid and the free surface profile is better described with LSS. While in the late stage ($t > t_1$), the flow propagates mainly in the horizontal direction. In this period, the free fall assumption is not valid and the free surface profile is better represented by ESS.

The behavior observed could be an important information to develop a more general solution to the dam break problem in the future, combining the LSS and the ESS. Thus, it is important to verify that our findings are not restricted to the present case ($H = 110$ mm). The experimental data available from LOBOVSKỲ *et al.* [32] is then used. Similarly, we identified the three stages for the case of $H = 300$ mm. The results are shown in Fig. 6.4, where $t_g = 100$ ms (Fig. 6.4b) and $t_1 \approx 183$ ms (Fig. 6.4c). In dimensionless form, the gate removal period t_g^* equals 0.57, which is less than half of the value ($\sqrt{2}$) proposed by LAUBER and HAGER [17]. Comparing to the present case ($H = 110$ mm), the same observations in the three stages can be made.

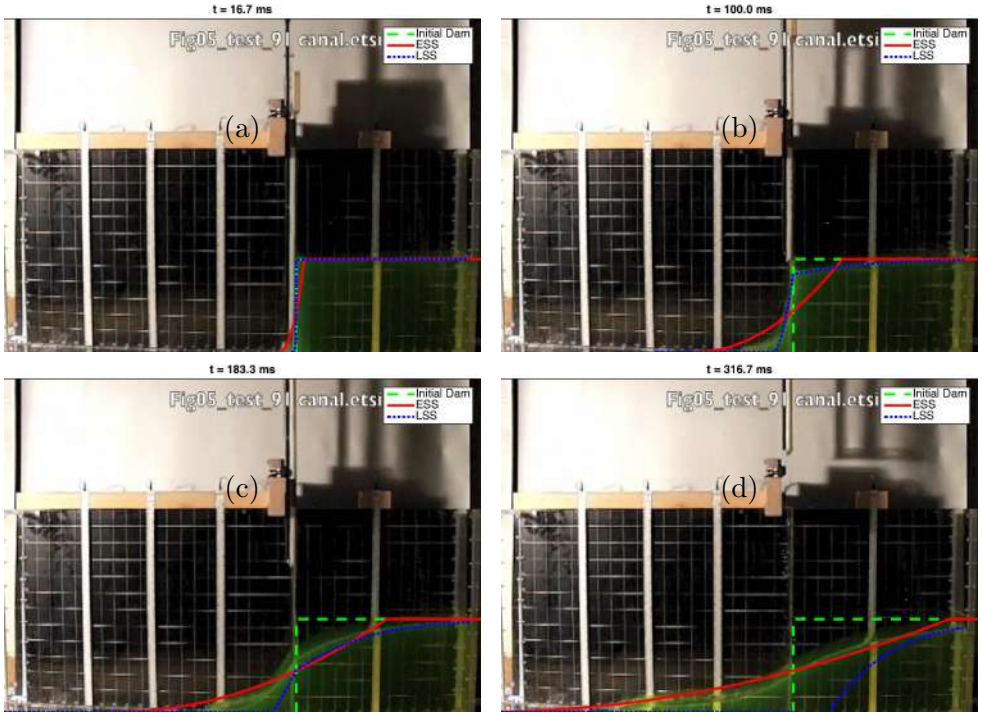

Figure 6.4: H=300 mm, evaluation of free surface profile, adapted from from LOBOVSKỲ *et al.* [32]

6.1.1 Sudden dam break

Based on the findings presented in the previous section, it is important to review the definition of "sudden dam break". As can be observed, the dimensionless gate removal period of $\sqrt{2}$ proposed by LAUBER and HAGER [17] is much larger than the value in our case ($t_g^* = 0.47$) for $H = 110$ mm and in the case ($t_g^* = 0.47$) of LOBOVSKỲ *et al.* [32] for $H = 300$ mm. It seems the value of $\sqrt{2}$ overestimates the gate removal period.

Note that LAUBER and HAGER [17] obtained this value $\sqrt{2}$ with the following assumption: the top particle P_1 behaves as free fall until P_1 reaches to bottom. As discussed before, until time $t = t_1$, particle P_1 falls to the location $\frac{4H}{9}$ and after this instant, P_1 would move mainly in the horizontal direction. The free fall assumption would not be valid in the later stage. This leads us to revise "sudden dam break" gate removal period proposed by LAUBER and HAGER [17].

Whether a dam break is "sudden" or not is directly related to the gate releasing velocity. The average gate releasing velocity could be estimated as

$$V_g = \frac{H}{t_g} \tag{6.2}$$

and in dimensionless form $V_g^* = \frac{V_g}{\sqrt{gH}}$. Clearly, V_g^* is a function of the initial water level H. To study the influence of H on V_g^*, four different cases are taking into

consideration. The first two cases are done in the present work with a lower water level ($H = 110$ mm) and a higher water level ($H = 220$ mm); the other two cases are available from the work of LOBOVSKỲ *et al.* [32], also with a lower water level ($H = 300$ mm) and a higher water level ($H = 600$ mm).

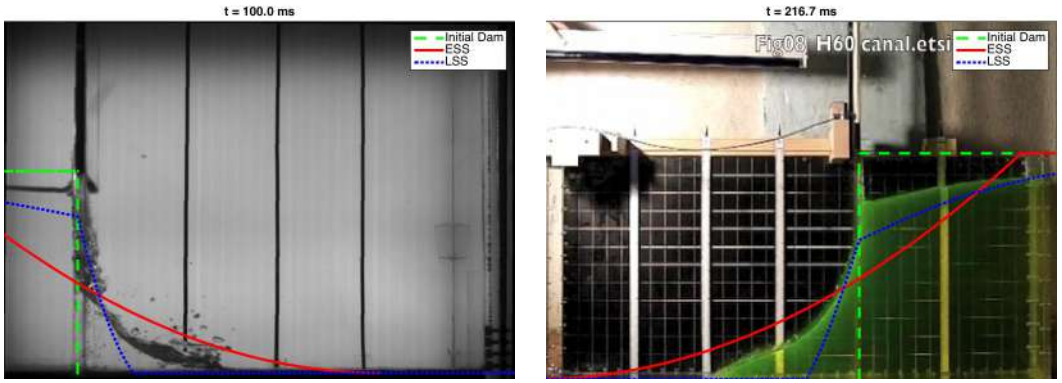

(a) $H = 220$ mm, present case

(b) $H = 600$ mm, from LOBOVSKỲ *et al.* [32]

Figure 6.5: Results of the two higher level cases at instant t_g

Table 6.1: The average gate releasing velocity and the gate removal period

H (mm)	t_g (ms)	V_g (m/s)	t_g^*	V_g^*	Agreement with LSS
Present case 110	50 ± 2	2.20	0.47	2.12	GOOD
Present case 220	100 ± 2	2.20	0.67	1.50	BAD
LOBOVSKỲ *et al.* [32] 300	100 ± 3.3	3.00	0.57	1.75	GOOD
LOBOVSKỲ *et al.* [32] 600	216.7 ± 3.3	2.77	0.87	1.14	BAD

The results of the two lower level cases at time t_g have already been shown in Fig. 6.1c and in Fig. 6.4b respectively. It is observed that for the two lower level cases, the agreement of free surface profile with LSS at time t_g is good. On the other hand, for the two higher level cases, as can be observed from Fig. 6.5, the agreement of free surface profile is poor that the curve the LSS is below the water free surface. This observation with the calculations of V_g and t_g for all four cases are summarized in Table 6.1, where t_g is obtained from the video frames. The uncertainty of t_g could be estimated as $\frac{1}{FPS}$, where FPS donates frame per second. In the present work $FPS = 500$ and in the work of LOBOVSKỲ *et al.* [32], $FPS = 300$.

This may be explained as follows. In the present work, since the gate releasing system remain the same for different water levels, then V_g for both water level cases are almost equal. However, the dimensionless velocity $V_g^* = \frac{V_g}{\sqrt{gH}}$ is decreased for

the higher water level case, as can be observed in Table 6.1. This argument is the same for the work of LOBOVSKỲ *et al.* [32]. In the two higher water level cases, as V_g^* is decreased, the dam gate is not released "suddenly" enough. Due to the existence of the gate, the discharge rate of the dam is reduced. Therefore at time t_g the dam holds more water than predicted by LSS. Thus, the two higher level cases could not consider as a "sudden dam break". It should be noted that even for the two higher level cases, t_g^* is still smaller than the value of $\sqrt{2}$ proposed by LAUBER and HAGER [17]. This confirms that the value of $\sqrt{2}$ proposed by LAUBER and HAGER [17] is overestimated.

From the data in Table 6.1, it could be found that the critical value of t_g^* might be within the range of [0.57, 0.67], which is much smaller than the value proposed by LAUBER and HAGER [17]. Further studies are required to find this exact value. In the present paper, as a first estimation, we recommend that the "sudden dam break" occurs when the gate removal period is smaller than $\frac{3t_1^*}{5} = \frac{3\sqrt{10}}{5} \approx 0.63$.

6.2 Main period with the piecewise solution

6.2.1 Horizontal bed cases

In the previous section, the main period is evaluated with the two Stoker solutions, in which bottom friction is not taking into account. The tangent of the free surface profile at the wave front tip predicted by ESS is horizontal, which does agree with a convex shape as can be observed in experimental, for example, in Fig. 6.1.

In this section, we evaluate the piecewise solution (PS) presented in Section 3.3, which takes account the bottom friction and bed slopes. Firstly, we consider the horizontal bed case. The results for the present case $H = 220$ mm and for case $H = 600$ mm available from LOBOVSKỲ *et al.* [32] are shown in Fig. 6.6a and Fig. 6.6b respectively.

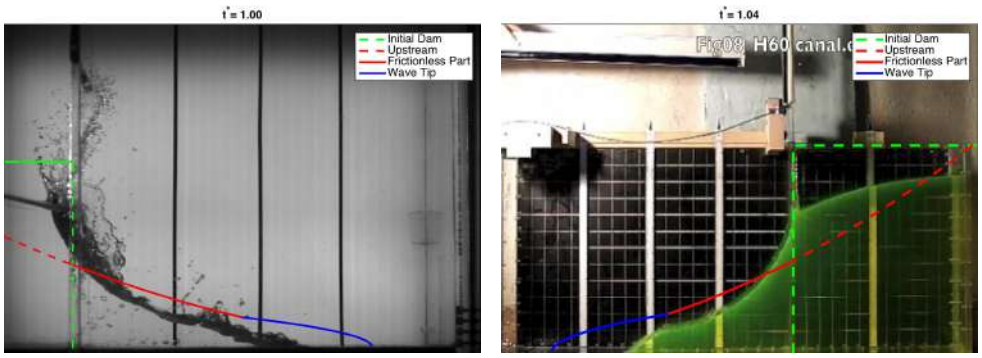

(a) H=220 mm, present case, with f=0.12

(b) H=600 mm, adapted from LOBOVSKỲ *et al.* [32], with f=0.16

Figure 6.6: Example results of the piecewise solution in horizontal channel

For a horizontal bed case, the PS actually is an extension of ESS by taking into account the bottom friction in the wave tip (wave front). The shape of the wave tip predicted by PS seems close to the experimental data, however, the wave tip location predicted by PS seems to be overestimated.

To improve the tracking ability of the wave front, we introduce a time compensation factor t_c in the PS as:

$$t' = t - t_c \tag{6.3}$$

The idea of t_c comes from the findings described in the previous section that ESS only works fine in the later stage. Thus, in the view of using ESS, the early times is not important and we may consider to compensate it. By taking $t_c^* = \frac{t_1^*}{3}$, for present cases $H = 110$ mm and $H = 220$ mm, the results are shown in Fig. 6.7 and Fig. 6.8 respectively.

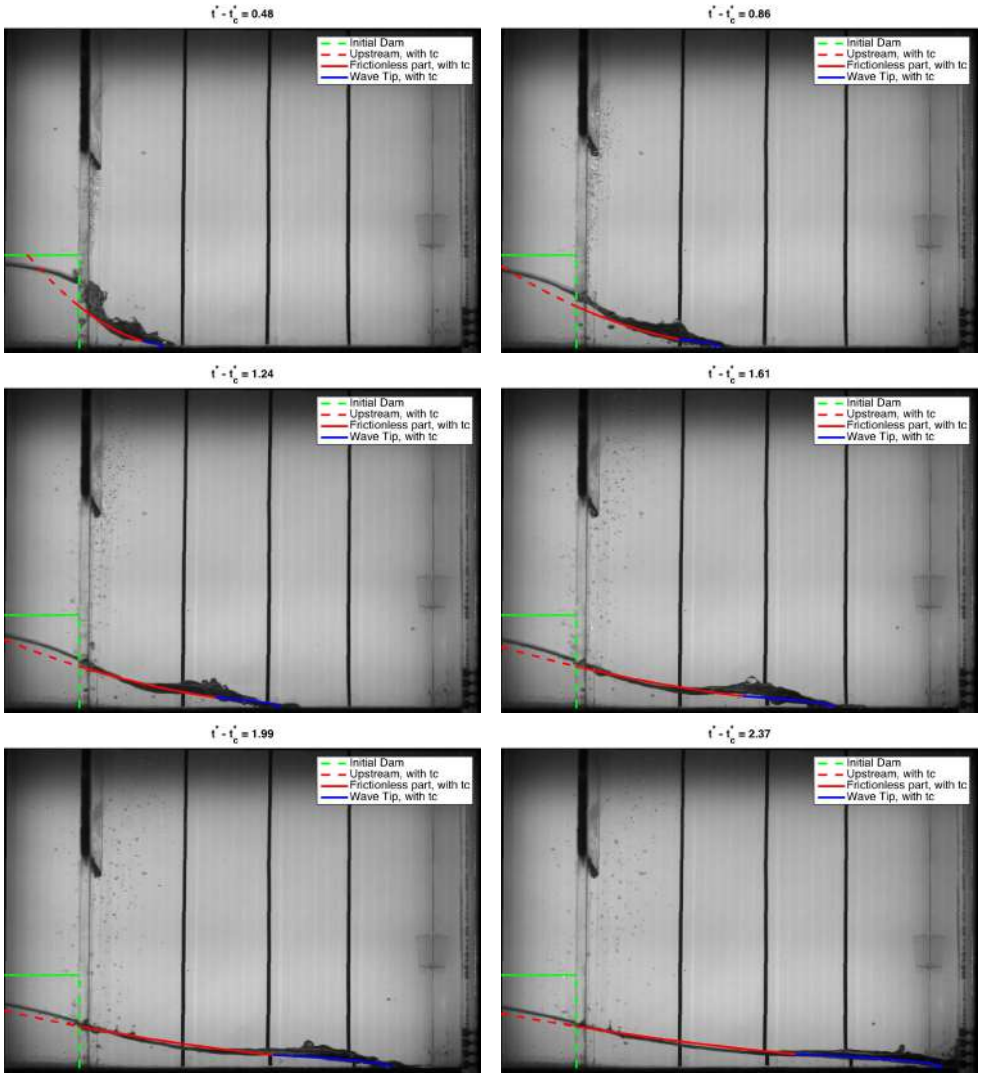

Figure 6.7: H=110 mm, results of the PS with compensated time $t_c^* = \frac{t_1^*}{3}$, and with bottom friction factor $f = 0.04$

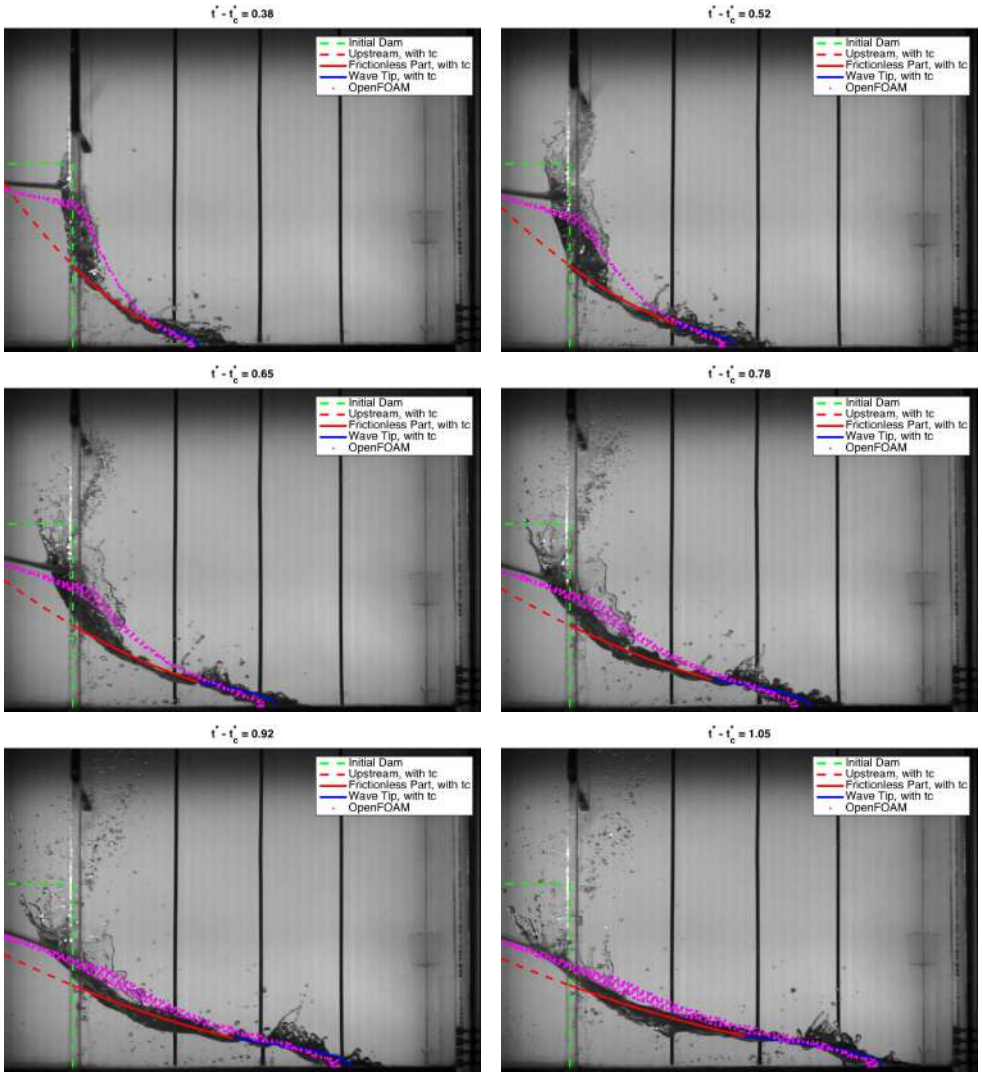

Figure 6.8: H=220 mm, results of the PS with compensated time $t_c^* = \frac{t_1^*}{3}$, and with bottom friction factor $f = 0.12$

It can be observed that the agreement between the piecewise solution with the experimental data becomes quite well in both main part and wave tip area. On one hand, the wave front location is well tracked by introducing the time compensation factor. On the other hand, the convex shape of the wave tip (wave front) is also well captured by choosing the bottom friction factor as $f = 0.04$ for case $H = 110$ mm and $f = 0.12$ for case $H = 220$ mm. Comparing to Fig. 6.1, the agreement with experimental data for the piecewise solution is much better than the ESS.

To verify that the piecewise solution with the time compensation are not restricted to the present cases, we also applied it to one previously published case H = 600 mm, available from LOBOVSKỲ *et al.* [32]. The results are shown in Fig. 6.9. A well agreement is also observed, by choosing $f = 0.16$. These observations indicate that by using the compensated time factor as $t_c^* = \frac{t_1^*}{3}$ and a proper bottom friction factor according to experiment, the PS now can track the wave front not

only in its advancing location but also in its convex shape in the wave tip.

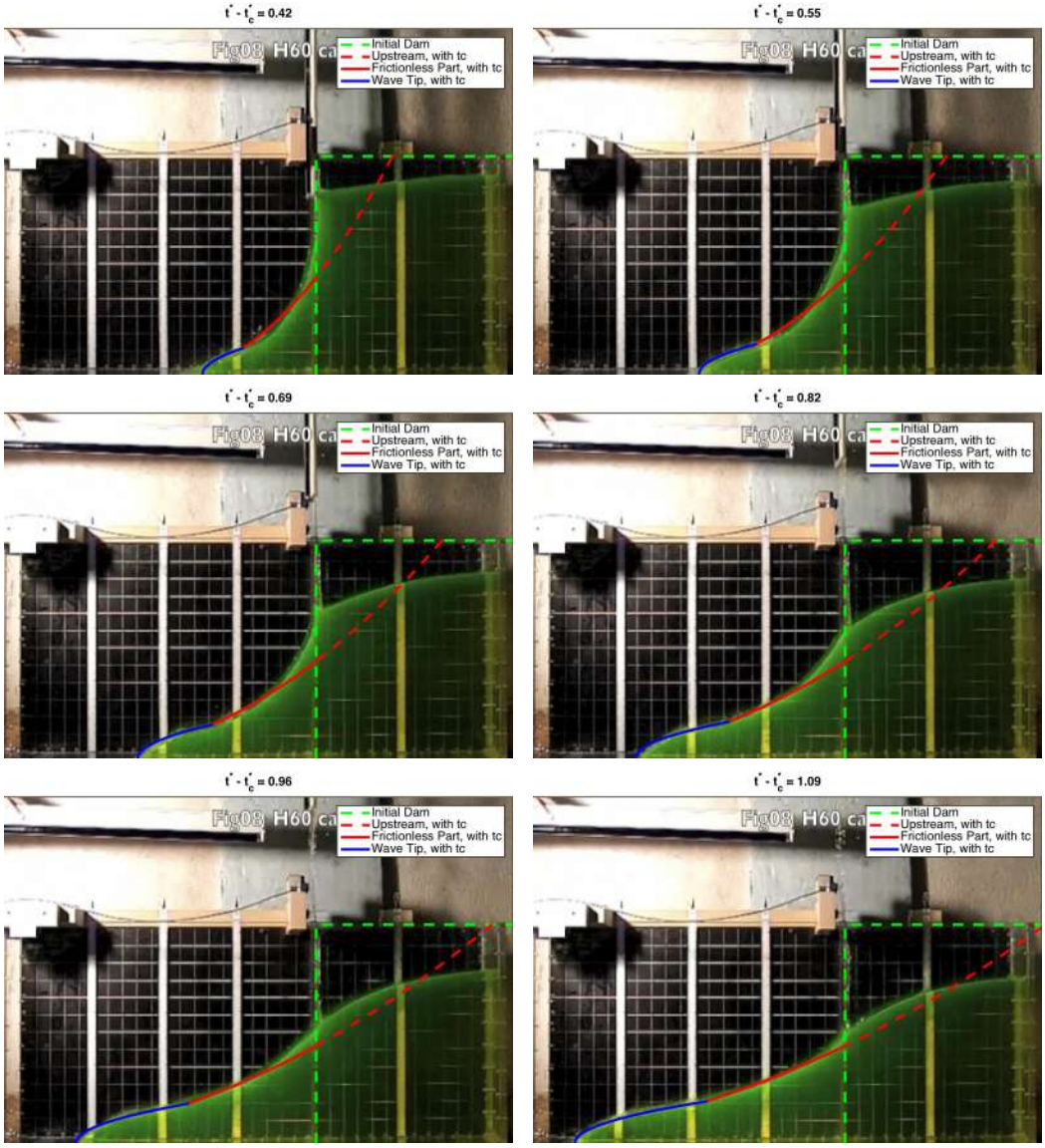

Figure 6.9: H=600 mm, adapted from LOBOVSKỲ *et al.* [32], results of the PS with compensated time $t_c^* = \frac{t_1^*}{3}$, and with bottom friction factor $f = 0.16$

Wave front angle estimation

As shown in Fig. 2.3, the water wedge angle is an important parameter to estimate the Green Water peak impact pressure. Assuming a horizontal bed case, since the wave front now can tracked by the compensated PS, it is possible to estimate the wedge angle θ as:

$$\theta = arctan\frac{\Delta h}{\Delta x} \tag{6.4}$$

where Δh is the maximum height of the wave tip and Δx is wave tip length. They can be estimated from the wave tip part solution of the compensated PS, as shown

in Section 3.3.1 and the wedge angle is given by,

$$\theta = arctan\frac{h_1'}{x_f' - x_1'} = arctan\frac{2\frac{f}{8}\frac{U_F'^2}{gH}}{(1 - \frac{U_F'}{2\sqrt{gH}})^2} \tag{6.5}$$

6.2.2 Slope bed cases

The slope bed cases can also be evaluated by PS with a compensated time factor $t_c^* = \frac{t_1^*}{3}$. The results for the different bed slope bed cases are summarized in Table 6.2.

Table 6.2: Summary of the different bed slope bed cases

Slope Angle (degree)	H (mm)	f	Figure
Downward 10	110	0.04	Fig.6.10
	220	0.12	Fig.6.11
Downward 5	110	0.04	Fig.6.12
	220	0.12	Fig.6.13
Upward 10	110	0.04	Fig.6.14
	220	0.12	Fig.6.15
Upward 5	110	0.04	Fig.6.16
	220	0.12	Fig.6.17

The following observations could be made:

- From Fig.6.10 to Fig.6.17, for all bed slope cases, for time large than $t^* \approx t_c^* + 0.3 \approx 0.63 \approx \frac{3t_1^*}{5}$, the downstream free surface profile between the PS and experimental data agrees relatively well. The wave front location and its shape is well captured by using a constant bottom friction factor ($f = 0.04$ for cases $H = 110$ mm and $f = 0.12$ for cases $H = 220$ mm).

- PS assumes a constant water level $\frac{4H}{9}$ at the dam section. This assumption seems to be valid for the downward slope cases (Fig.6.10 to Fig.6.13); while the upward slope bed cases, the water level at the dam section seems to be larger than $\frac{4H}{9}$, as shown in Fig.6.14 to Fig.6.17.

- The free surface profile between the numerical simulation results by OpenFOAM and the experimental data agrees well.

As described previously, the time interval within $[0, \frac{3t_1^*}{5}]$ might be assumed to be the gate releasing stage for a sudden dam break. Since t_c^* is introduced in the

solution, the solution would not work for $t^* < t_c^*$. We recommend to use PS with t_c for time large than $\frac{3t_1^*}{5}$. For time less than $\frac{3t_1^*}{5}$, it relates to the initial stages of dam break problem where the time compensation factor should not be used.

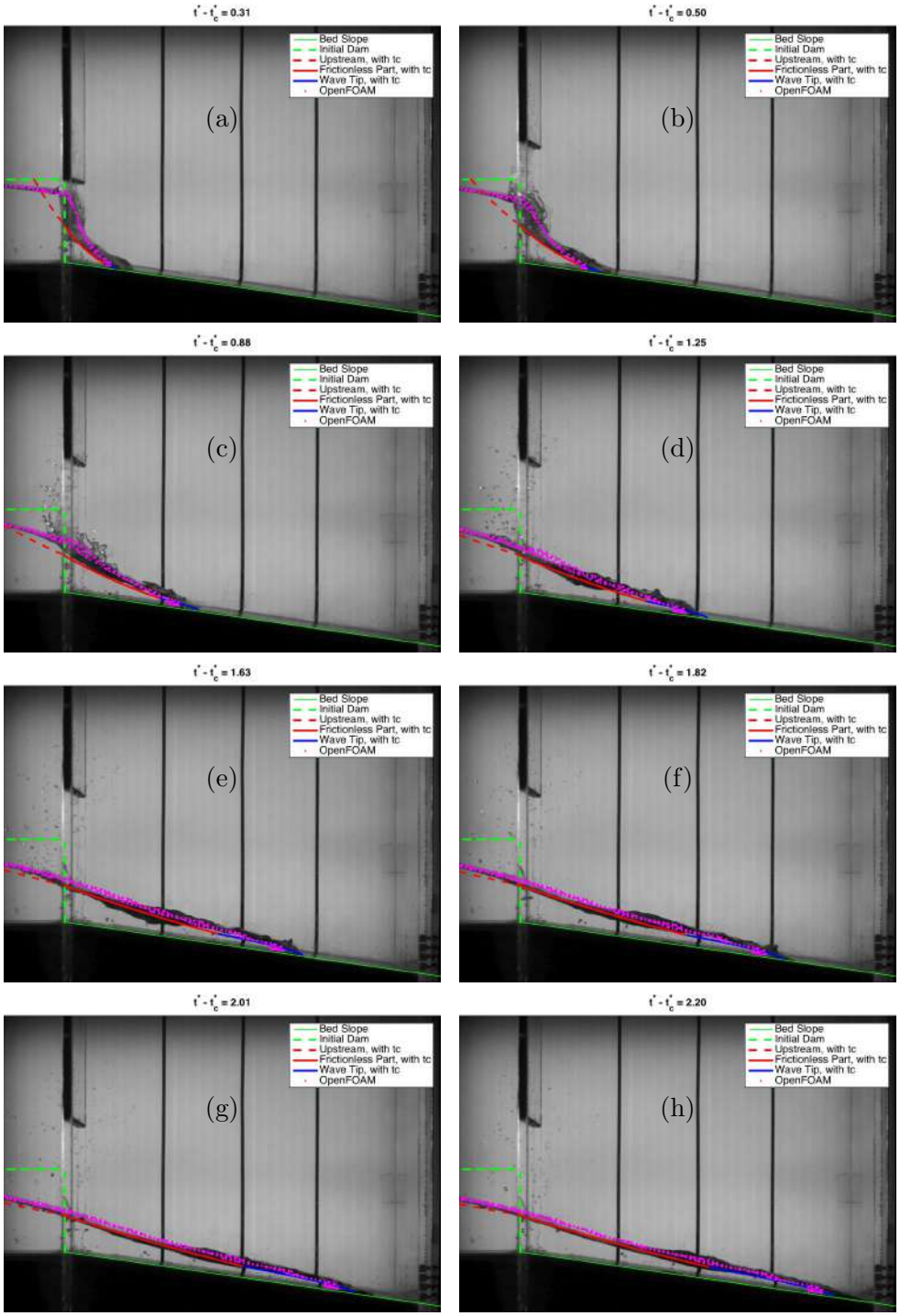

Figure 6.10: H=110 mm, evaluation of free surface profile for downward slope angle 10 degree, with $t_c^* = \frac{t_1^*}{3}$ and with $f = 0.04$

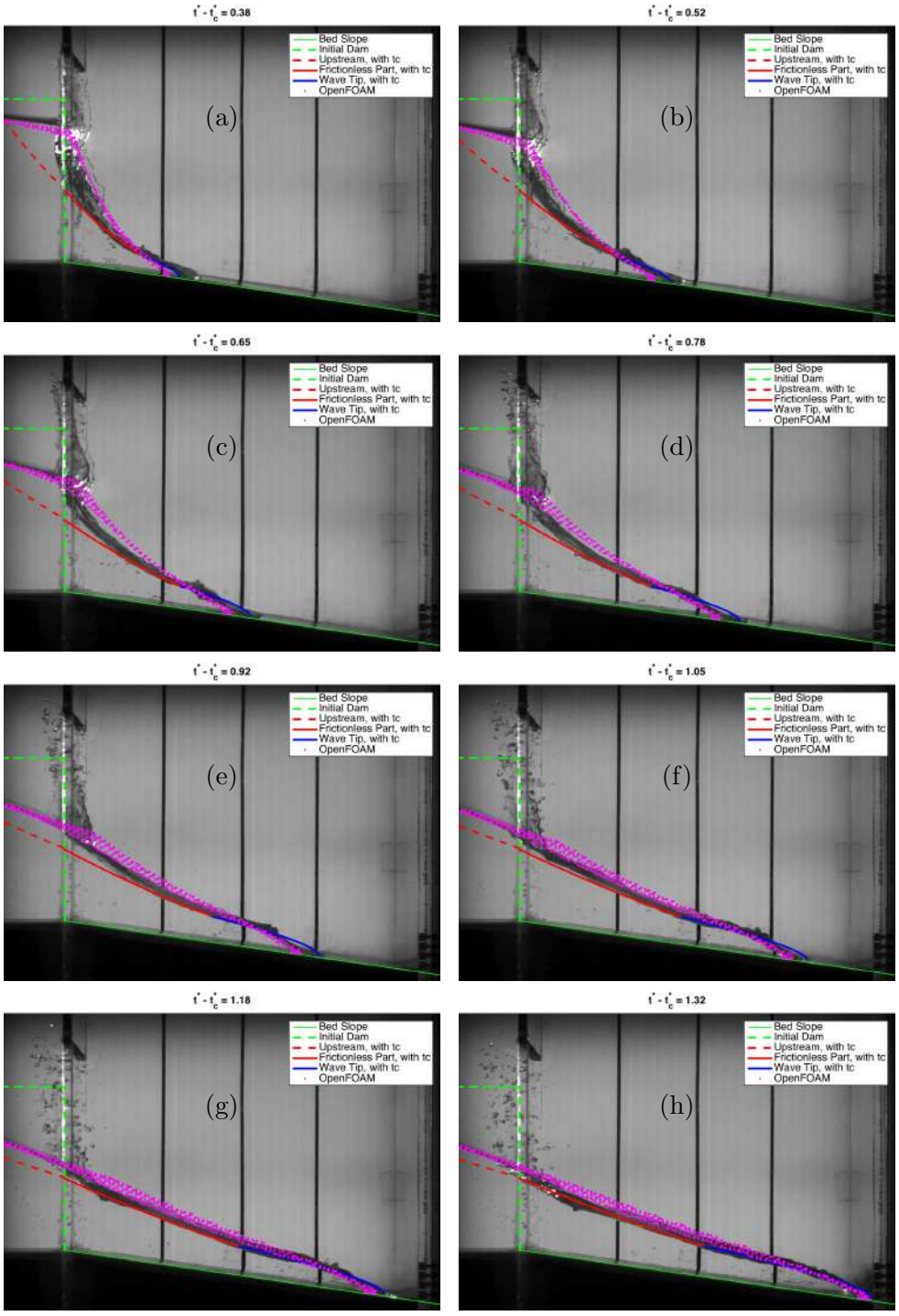

Figure 6.11: H=220 mm, evaluation of free surface profile for downward slope angle 10 degree, with $t_c^* = \frac{t_1^*}{3}$ and with $f = 0.12$

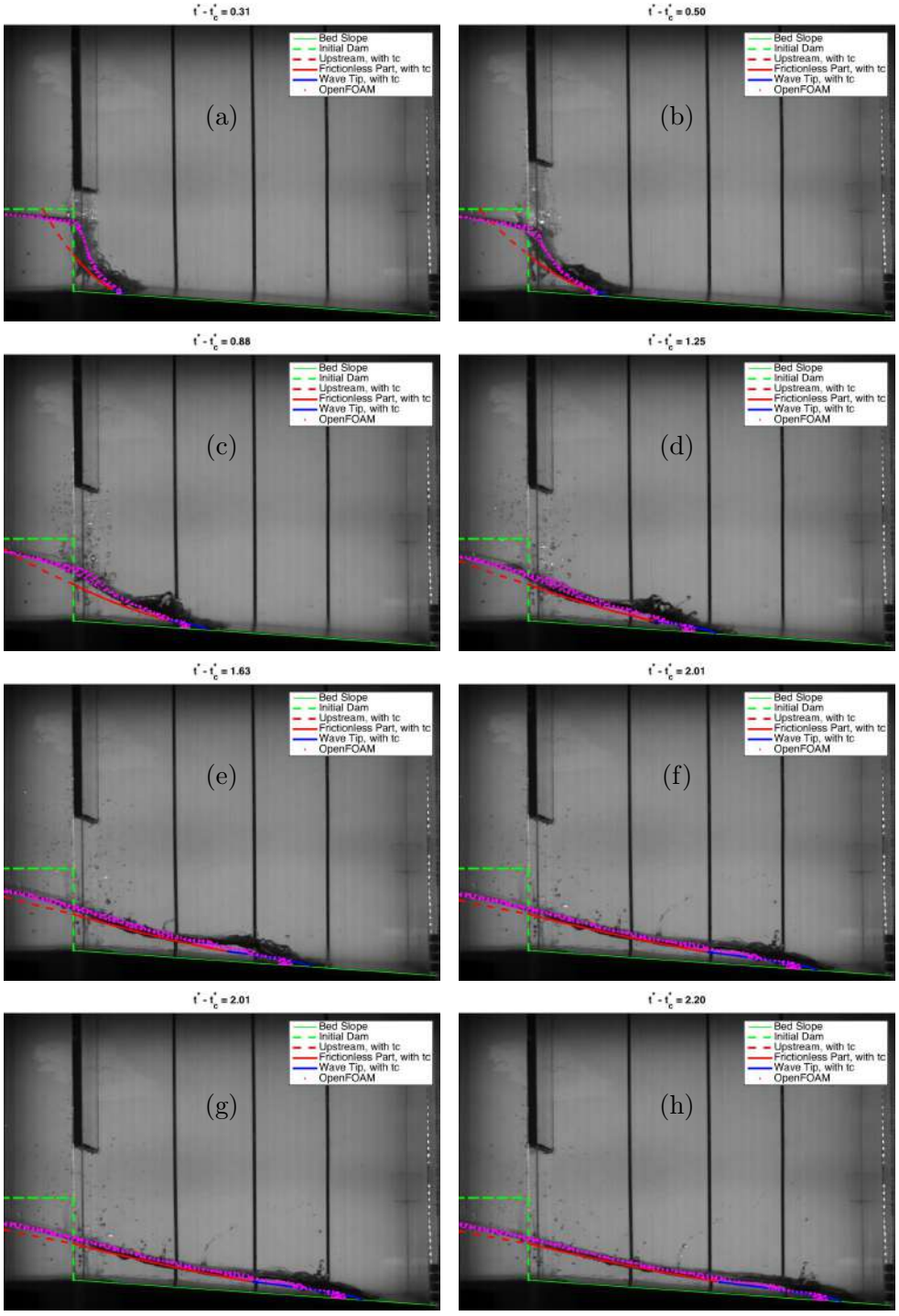

Figure 6.12: H=110 mm, evaluation of free surface profile for downward slope angle 5 degree, with $t_c^* = \frac{t_1^*}{3}$ and with $f = 0.04$

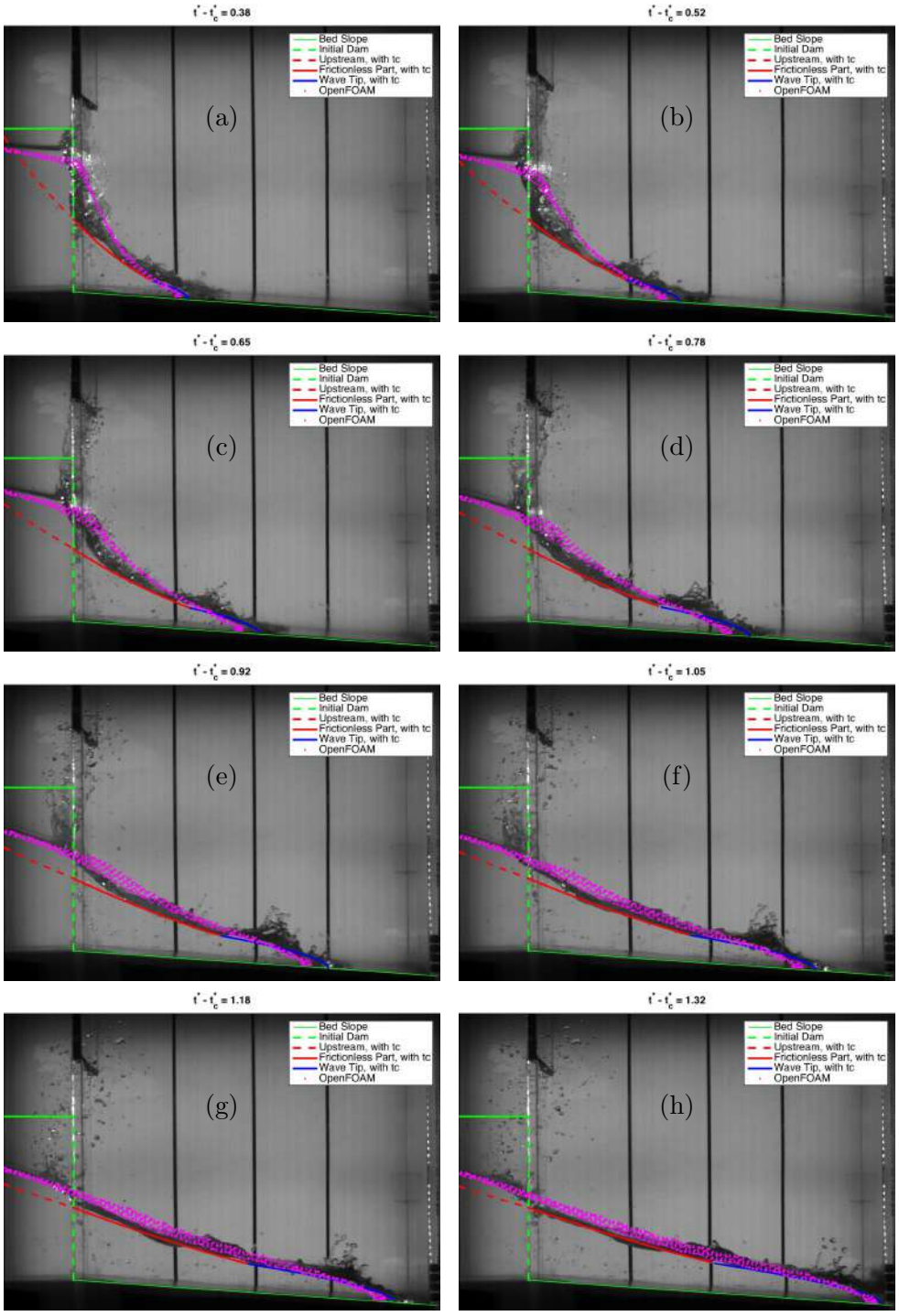

Figure 6.13: H=220 mm, evaluation of free surface profile for downward slope angle 5 degree, with $t_c^* = \frac{t_1^*}{3}$ and with $f = 0.12$

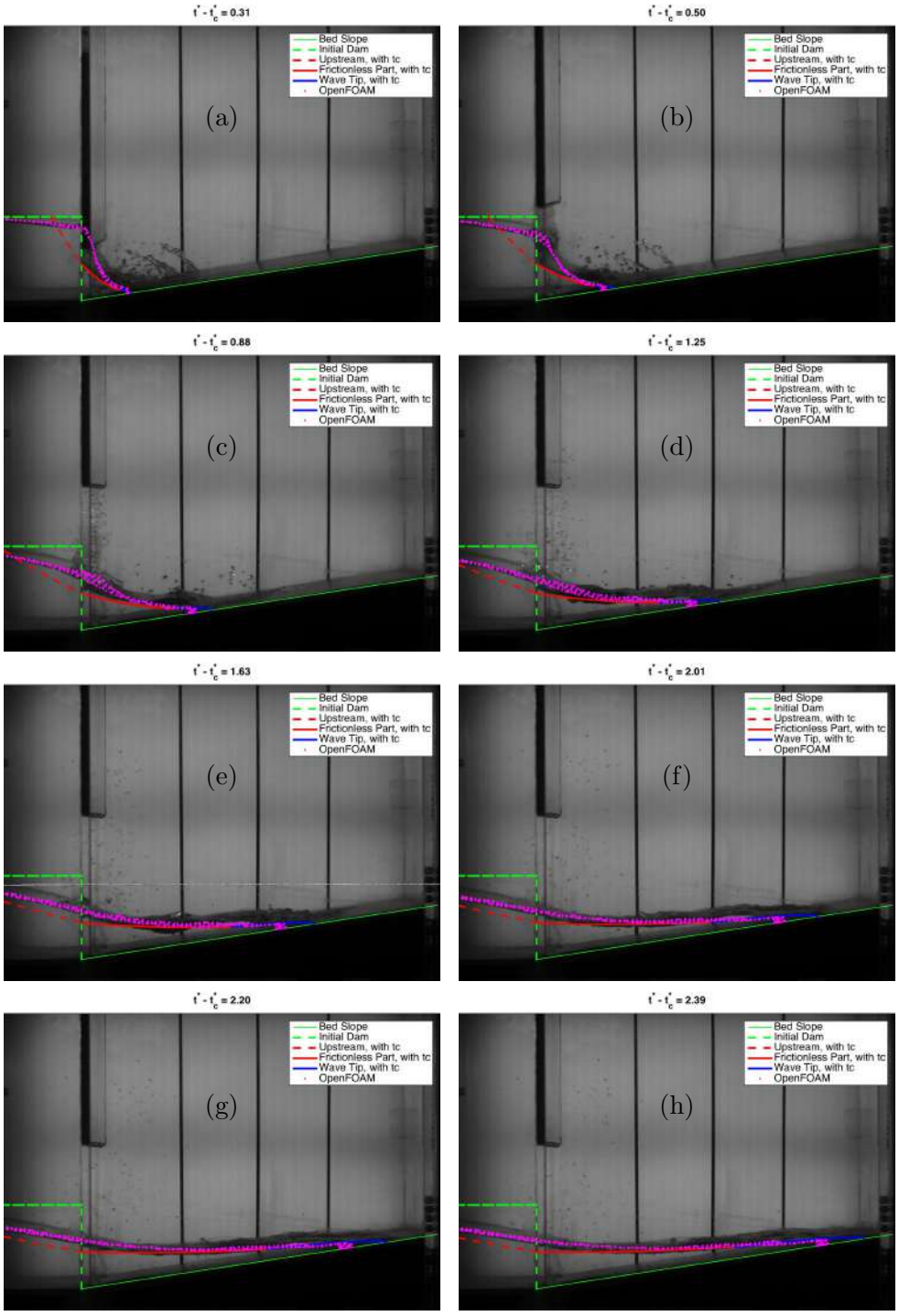

Figure 6.14: H=110 mm, evaluation of free surface profile for downward slope angle 10 degree, with $t_c^* = \frac{t_1^*}{3}$ and with $f = 0.04$

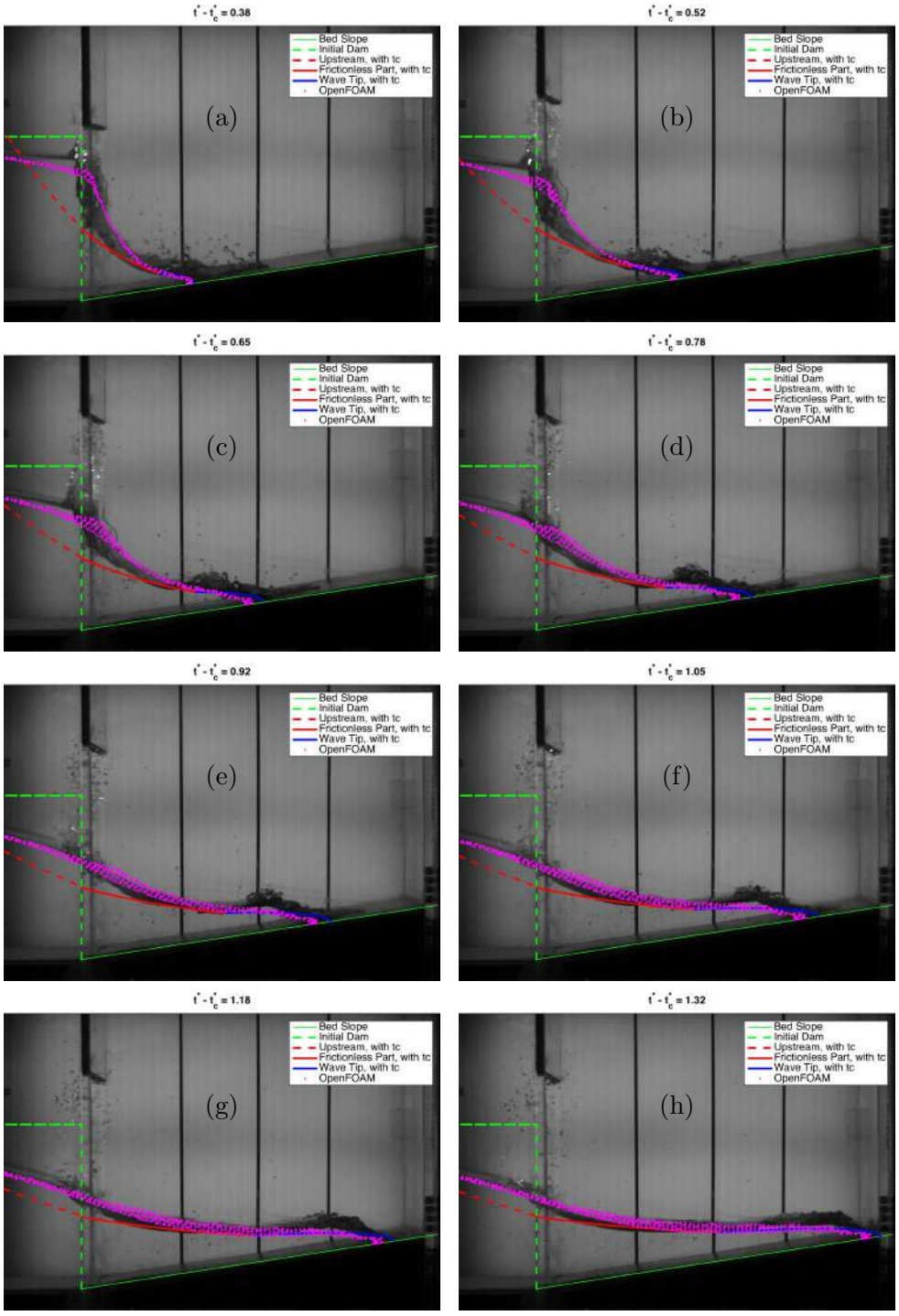

Figure 6.15: H=220 mm, evaluation of free surface profile for upward slope angle 10 degree, with $t_c^* = \frac{t_1^*}{3}$ and with $f = 0.12$

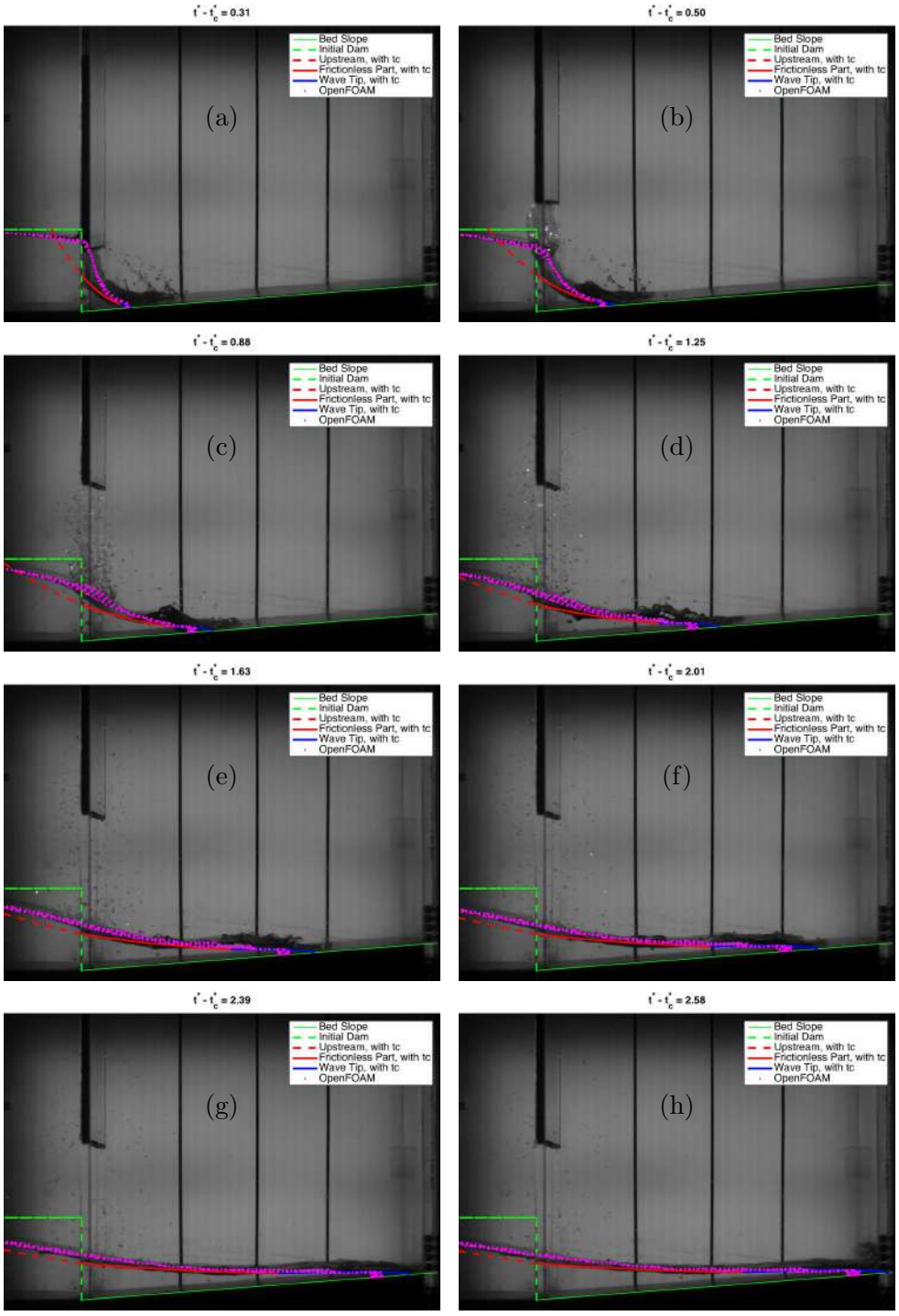

Figure 6.16: H=110 mm, evaluation of free surface profile for downward slope angle 10 degree, with $t_c^* = \frac{t_1^*}{3}$ and with $f = 0.04$

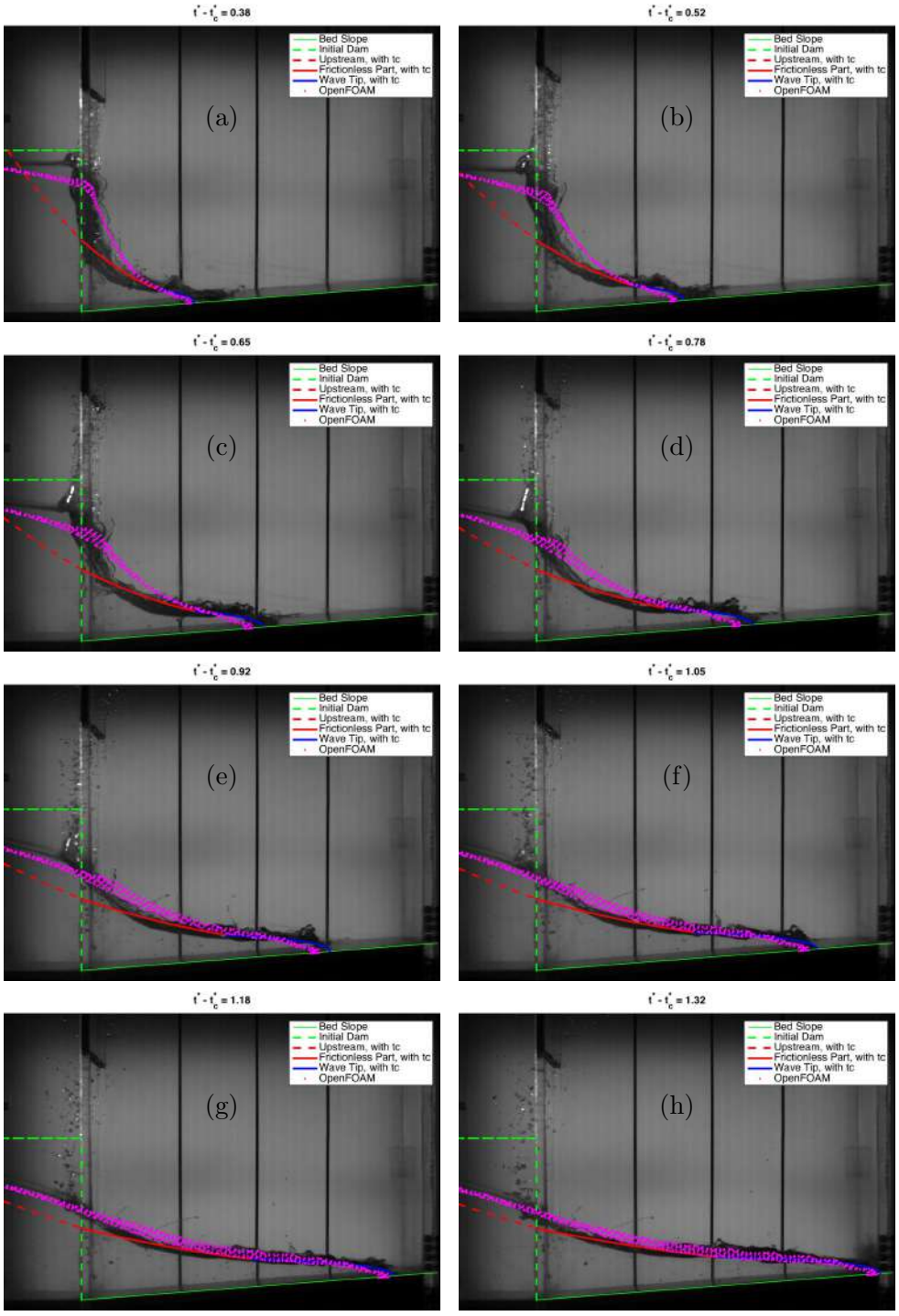

Figure 6.17: H=220 mm, evaluation of free surface profile for downward slope angle 10 degree, with $t_c^* = \frac{t_1^*}{3}$ and with $f = 0.12$

6.2.3 Bottom friction factor

Questions may arise on the bottom friction factor. The bottom friction factor is related to flow resistance. The flow resistance is quite a big topic, as pointed by YEN [73]:"Over the years there have been numerous investigators who have made important contributions to open-channel flow resistance. "

According to ROUSE [74], the flow resistance could be classified into four components: 1) surface or skin friction, 2) form resistance or drag, 3) wave resistance from free surface distortion, and 4) resistance associated with local acceleration or flow unsteadiness. By using the Darcy-Weisbach resistance coefficient f, he expressed the resistance as the following dimensionless symbolic function:

$$f = F(Re, K, \eta, N, Fr, Un) \tag{6.6}$$

in which Re = Reynolds number; K = relative roughness, usually expressed as k_s/R_H, where k_s is the equivalent wall surface roughness and R_H is hydraulic radius of the flow; η = cross-sectional geometric shape; N = nonuniformity of the channel; Fr = Froude number; Un = degree of flow unsteadiness; and F represents a function.

For a special case of steady uniform flow in straight constant diameter rigid pipes, ROUSE [74] evaluated with Eq. (6.6) yields to the commonly called the Moody diagram. There are other empirical formulations to estimate the flow resistance for steady flow. Two different approaches are showed in the following sections.

Approach A

According to CHANSON [53], the bottom friction may be estimated with the Chézy coefficient (C) and the Darcy-Weisbach coefficients (f) as,

$$C = \frac{1}{n} R_H^{\frac{1}{6}} = \sqrt{\frac{8g}{f}} = \sqrt{\frac{g}{K}} \tag{6.7}$$

where R_H is the hydraulic radius, calculated by the tank width W and initial water level H:

$$R_H = \frac{W * H}{W + 2H} \tag{6.8}$$

and n is the Manning roughness coefficient. According to CHANSON [53], the Manning roughness coefficient for the plastic or glass can be estimated as 0.01. The bottom friction factor are calculated in Table 6.3.

Table 6.3: Bottom friction factor calculation with Approach A

Cases	W (m)	R_H (m)	C	f
Present $H = 110$ mm	0.335	0.066	63.63	0.019
Present $H = 220$ mm	0.335	0.095	67.56	0.017
LOBOVSKỲ *et al.* [32] $H = 300$ mm	0.15	0.060	62.57	0.020
LOBOVSKỲ *et al.* [32] $H = 600$ mm	0.15	0.067	63.67	0.019

Approach B

CHANSON [53] and CHANSON [75] also proposed another empirical formulation (called Altsul formula) as:

$$f = 0.1(1.46\frac{k_s}{D_H} + \frac{100}{Re})^{\frac{1}{4}} \tag{6.9}$$

where k_s is the typical roughness height and D_H is the hydraulic diameter and Re is the Reynolds number defined as:

$$Re = \frac{\sqrt{gH}D_H}{\nu} \tag{6.10}$$

Table 6.4: Bottom friction factor calculation with Approach B

Cases	D_H (m)	Re	f
Present $H = 110$ mm	0.266	3.07E+05	0.0576
Present $H = 220$ mm	0.380	4.40E+05	0.0527
LOBOVSKỲ *et al.* [32] $H = 300$ mm	0.240	4.59E+05	0.059
LOBOVSKỲ *et al.* [32] $H = 600$ mm	0.267	6.49E+05	0.057

Notes on bottom friction factors

The calculated bottom friction factors in Table 6.3 and Table 6.4 with different approaches are different. Both approaches shows that the bottom friction factors is only slightly affected by the initial water level H.

To the best knowledge of the author, these empirical formulations are suitable for the steady flow. However, the dam break wave is an unsteady flow. According to ROUSE [74], the unsteadiness of the dam break flow contributes to the flow resistance. These empirical formulation seems not to be suitable for the unsteady dam break flow. As shown in Table 6.2, the bottom friction factor is quite different for $H = 110$ mm and $H = 220$ mm. The agreement of these empirical formulations does not seem to be good. Due to the limited time, the bottom friction factor would be left for further researches.

6.3 Pressure measurement

6.3.1 Typical signal of pressure

A typical signal of the pressure sensors and the zoom pressure peaks are shown in Fig. 6.18. The following aspects should be paid attention to:

1. small peaks before impact: due to gate releasing
2. pressure drop after impact: related to phase changing effects
3. the ability of the pressure Return-To-Zero (RTZ) after impact

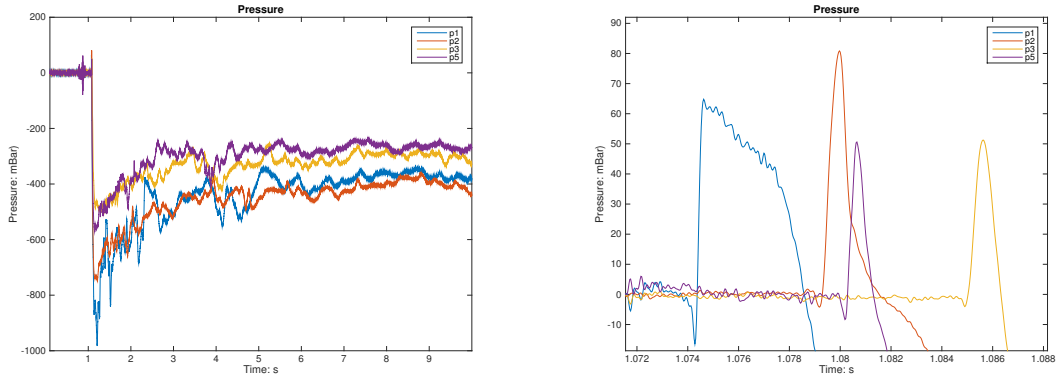

(a) A typical signal of pressure sensors (b) Zoomed pressure peaks

Figure 6.18: A typical signal of pressure sensors and the zoomed pressure peaks

Small peaks due to gate releasing

During the gate releasing stage, due to the friction between the gate and tank, there is vibration on the structure. This vibration leads to the strong variation in the acceleration signal and damping quickly. The vibration yields small variations on the pressure signal during the gate releasing: when the gate start releasing and when the gate reach the top, as shown in Fig. 6.19. Fortunately, before the impact peak pressure, those small variations on pressure have already damped almost to zero. Thus the vibration related to gate releasing seems not affect the measurement of the impact peak pressure.

Pressure drop related to phase changing effects

To study the sudden pressure drop as shown in Fig. 6.18a, by taking advantage of the 6 DOF platform, the periodical pitch motion is applied to evaluate the performance of the pressure sensors. The setup of the pitch motion test is shown in Fig. 6.20, no

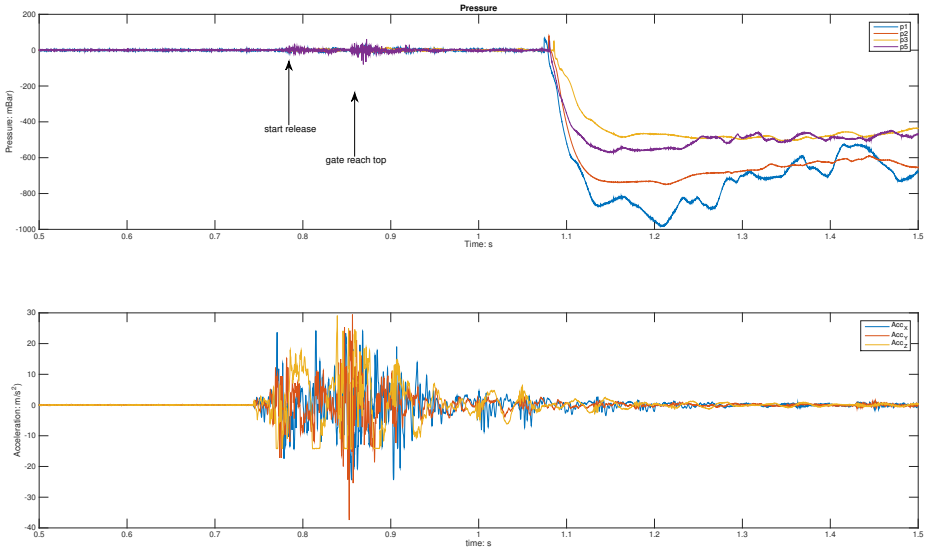

Figure 6.19: Small peaks before impact related to the gate releasing

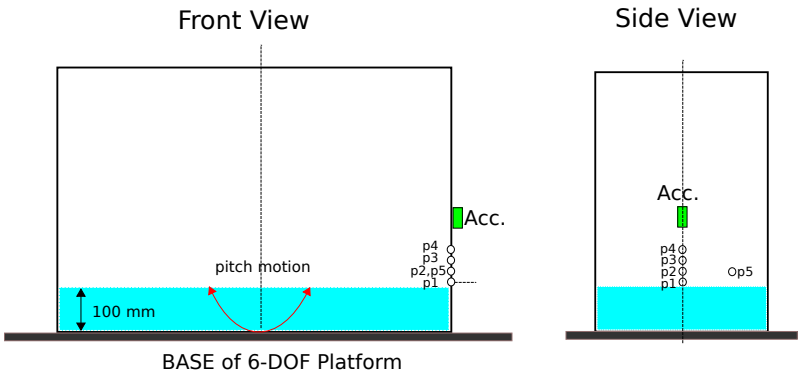

Figure 6.20: Pitch motion test with 6 DOF platform

bed blocks is used. The still water level is set to 100 mm to make sure all pressure sensors initially out of water.

Fig. 6.21 shows the results of pitch motion test in period of 3 seconds and 10 seconds, with the same amplitude of the pitch angle in 10 degree. In period of of 10 seconds, the platform moves slowly, a wave was generated in the tank, pressure sensors p1, p2 and p5 was initially dry but later are always underwater due to the wave; pressure sensors p3 and p4 are in a higher position, for this two sensors, there is a phase changing from air to water due to the wave periodically. In period of 3 seconds, the platform moves faster, the amplitude of the generated wave is higher that the phase changing from air to water is happened for all pressure sensors. Consistently a sudden pressure drop is observed: in period of 10 seconds for sensor p3 and p4; in period of 3 seconds for all sensors.

From the above observation, it could be concluded that the pressure drop is related to the phase changing effects. This phase changing may relate to the thermal

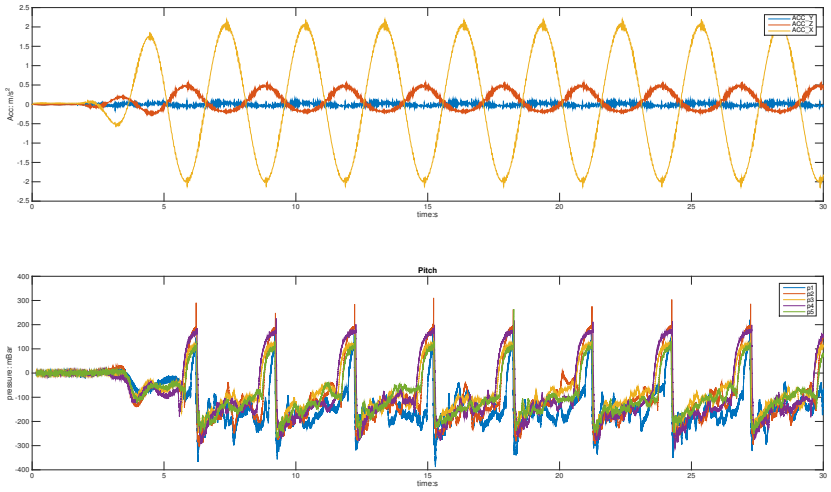

(a) Period of 3 seconds

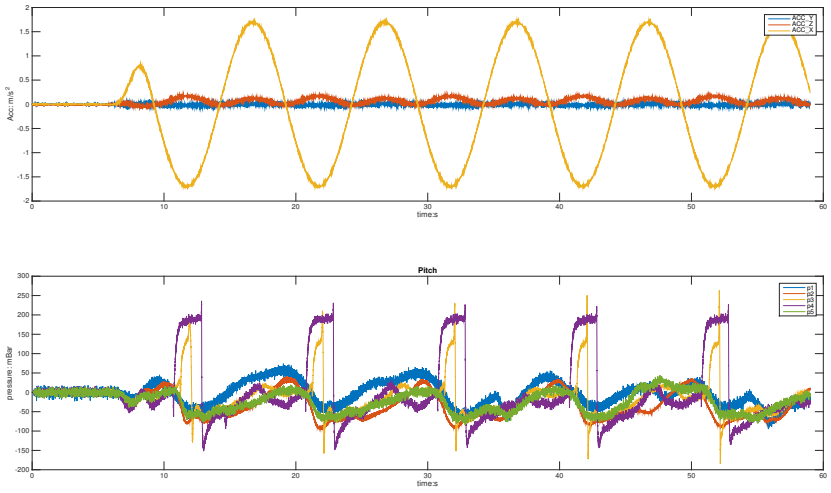

(b) Period of 10 seconds

Figure 6.21: Pitch motion test in different periods, the amplitude of the pitch angle is 10 degree

shock effects as called by VASSILAKOS *et al.* [76] or temperature shock effects as called by PISTANI and THIAGARAJAN [77]. In the convenience for later discussion, it is simply called as the thermal shock effects. As demonstrated by PISTANI and THIAGARAJAN [77], the thermal shock effects are caused by the sudden cooling of the dry sensor when it comes in contact with the liquid. The sudden cooling, due to the contact with the liquid, causes a non homogeneous contraction on the pressure sensor sensing surface that apparently results in an unwanted deformation in the element underneath. VASSILAKOS *et al.* [76] also studied the thermal shock effects and concluded that since heat transfer is involved, the thermal response takes a large fraction of a second to become evident, thus the thermal shock effects are

not important as they occur much later in time than the initial pressure pulse. This means that the thermal shock effects do not necessarily imply inaccuracy of the pressure readings during the impact event, but it could be a concern for the later time pressure response.

However, this pressure drop maybe more complex than the thermal effects. Firstly, the temperature for water and air are measured as 24.6°C and 25.3°C respectively to two LM35 Precision Centigrade Temperature Sensor T_IN (for water) and T_OUT (for air). Thus this difference in temperature of air and water is quite small, less than one degree. Secondly, it is observed from Fig. 6.21 that the phase changing velocity seems also has its contribution on the pressure drop. Initially all sensors are dry and out of water, when the platform starts to move, the movement is slow and the pressure sensor contact with liquid gently. For both periods, there are a small initial pressure drop. This small pressure drop is more related to the temperature difference between air and water, since the phase changing velocity is slow. While for the later stages, the velocity of the generated wave increased, with the increased phase changing velocity, the periodical pressure drop is much larger. What's more, considering the initial pressure drop for both periods, the initial pressure drop in period of 10 seconds is lower comparing to the period of 3 seconds. It is also could be explained as the phase changing velocity is lower for period of 10 seconds than for period of 3 seconds.

Although this pressure drop maybe a important aspect for the pressure measurement, but how to overcome it has been out of the scope of this study. It is recommended further studies on this topic.

Return-To-Zero ability

Significant concern also exists regarding the ability of the pressure transducers to return to zero reading following a water impact event. Fig. 6.18a shows the pressure signal after the pressure drop (due to the thermal shock effects) remain negative and do not return to zero. This maybe related to the properties of the sensor itself. The pressure sensors used in the work are produced by the Measurement Specialties Inc. (short as MS). VASSILAKOS *et al.* [76] studied this issue with different pressure sensors, one from MS also, the other is from Endevco Corp. The Endevco sensors are found with RTZ ability while the MS sensors do not have the RTZ ability. Unfortunately, the pressure sensors available for this work are MS sensors and they do not have the RTZ ability.

Repetitions

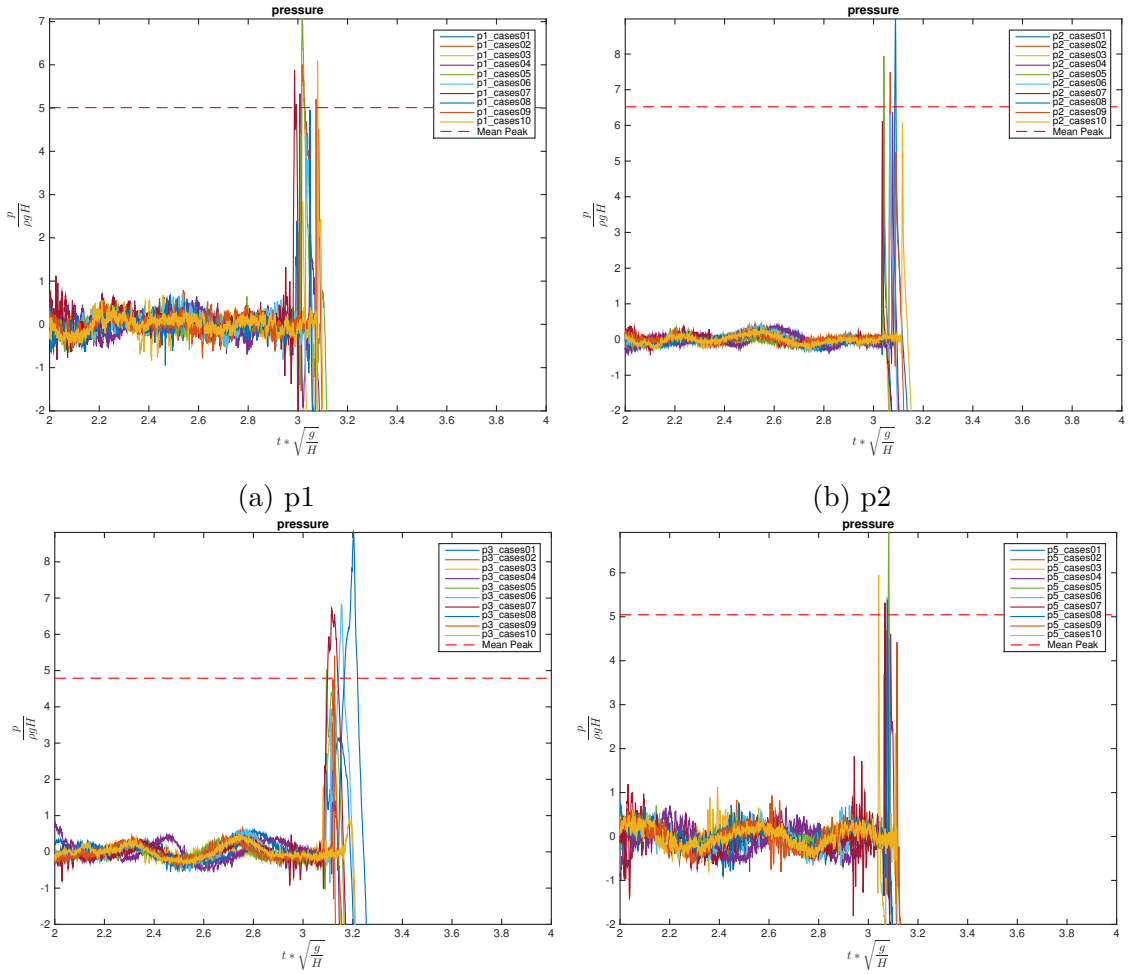

(a) p1 (b) p2

(c) p3 (d) p5

Figure 6.22: Pressure peaks in ten times repetitions for horizontal bed case $H = 110$ mm

Due to the existence of the pressure drop effects, the pressure signal after of the peak is not in interest. The important is the impact peak pressure. The zoomed pressure peak is shown in Fig. 6.18b. The peak signals of sensor p1, p2 and p3 are in time sequence according to the position order from low to high. The difference in sensor p2 and p5 may implies the possible 3 D effects.

Fig. 6.22 shows the pressure peaks in ten times repetitions, where the mean peak value is marked with the red dashed line. Comparing to LOBOVSKỲ *et al.* [32] (the mean peak value is about 3.2), the mean peak value measured in this work is larger.

Notes on pressure sensor

Although a lot of time has been spent to improve the pressure signal quality, unfortunately with the limited resources in both instrumentation and time, the quality of the pressure signal captured is not considered to be good, due to the following aspects: (a) high noise to signal ratio (in Fig. 6.22, the variation before the peak signal may upto 20% of the peak value); (b) significant pressure drop due to phase changing effect; (c) lacking of RTZ ability.

6.3.2 Numerical pressure results

The numerical simulation results are shown in Fig. 6.24 for case $H = 110$ mm and Fig. 6.24 for case $H = 220$ mm. It is expected that for downward slope bed cases with a higher pressure and for upward slope bed cases with a lower pressure.

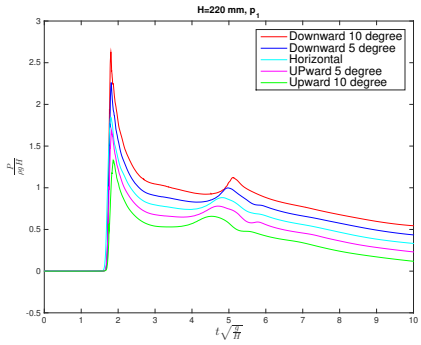

(a) Simulated pressure p_1

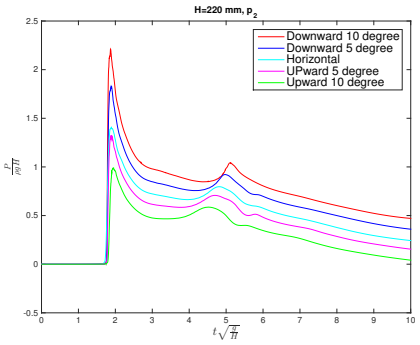

(b) Simulated pressure p_2

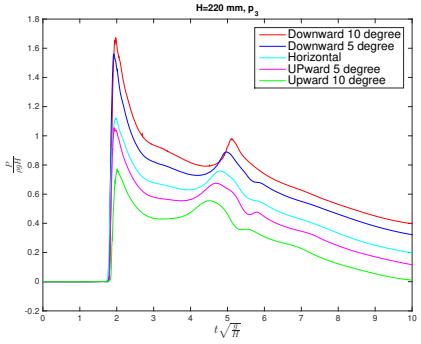

(c) Simulated pressure p_3

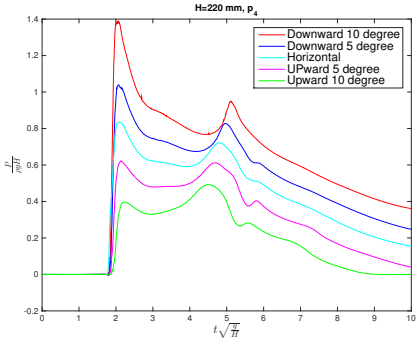

(d) Simulated pressure p_4

Figure 6.23: Simulated pressure for $H = 220$ mm

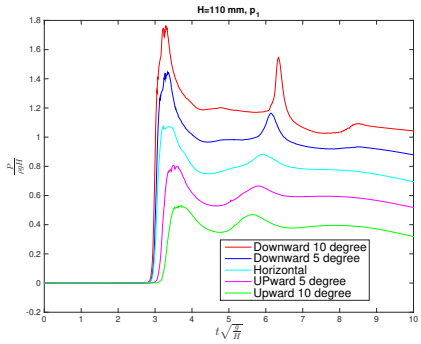

(a) Simulated pressure p_1

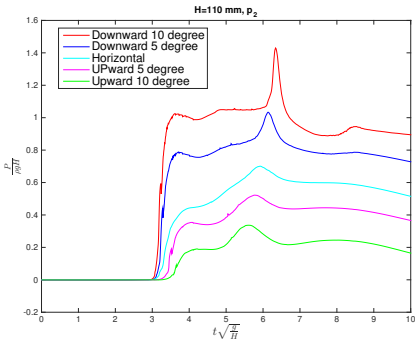

(b) Simulated pressure p_2

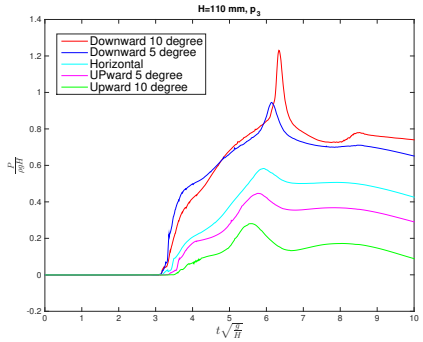

(c) Simulated pressure p_3

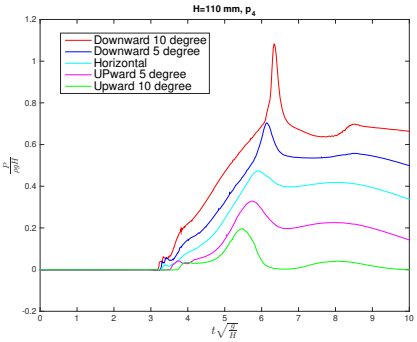

(d) Simulated pressure p_4

Figure 6.24: Simulated pressure for $H = 110$ mm

6.4 Elevations

6.4.1 Wave probes

Each case is repeated ten times. For instance, Fig. 6.25 shows the experimental elevation time history at wave probe location h7 and h8 in 10 times repetition for horizontal bed case $H = 110$ mm.

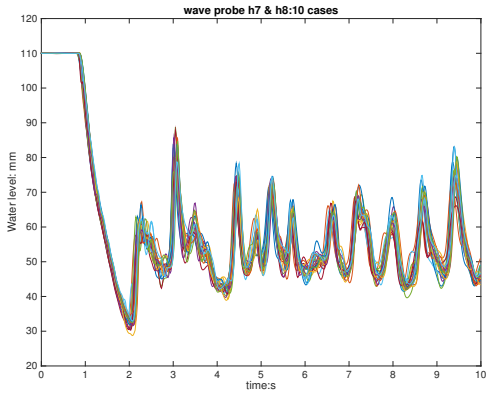

Figure 6.25: Elevation time history of wave probe h7 and h8 for horizontal bed case $H = 110$ mm, in 10 repetitions

Considering the repetition on the wave probes is quite good, in the followings, only one typical signal is given to compare with the numerical results.

Fig. 6.26 shows the elevation time history at wave probe location h7 and h8 for the horizontal bed cases. Before the reflection wave advancing back to the wave probe, a very well agreement can be observed between the OpenFOAM simulation results (in color blue) and the experimental data (in color red). The difference between the simulation results and the experimental data mainly lies after the reflection wave reaching the wave probe. Even so, the agreement seems to be relatively well. The differences in h7 and h8 indicates the 3D effects. It is observed that the 3D effects in the numerical simulation results is less than in the experimental data.

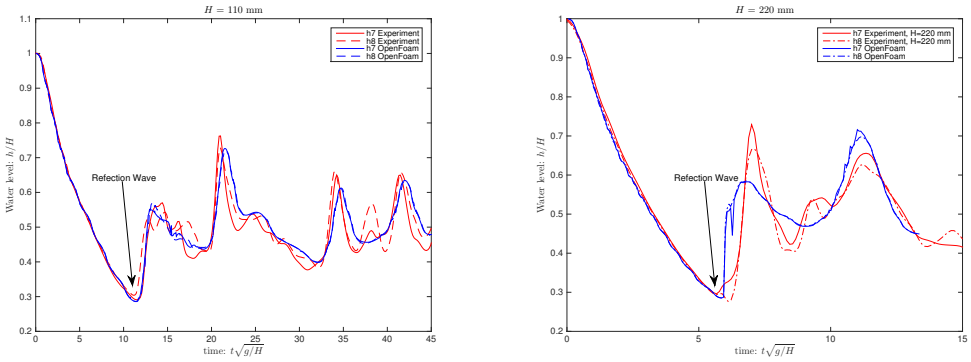

(a) H=110 mm (b) H=220 mm

Figure 6.26: Elevation time history at wave probe location h7 and h8 for horizontal bed

The elevation time history at wave probe location h7 and h8 for the slope bed cases are shown in Fig. 6.27

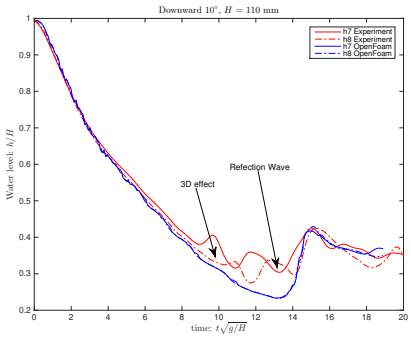

(a) Downward 10°, $H = 110$ mm

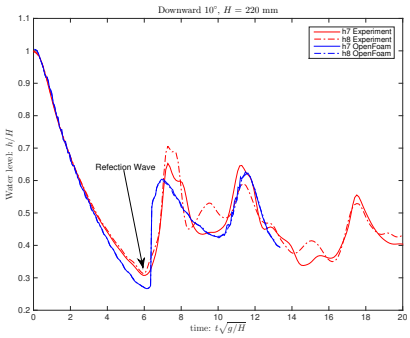

(b) Downward 10°, $H = 220$ mm

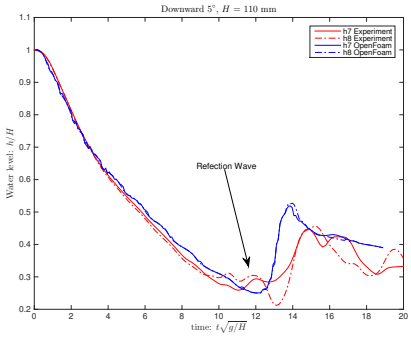

(c) Downward 5°, $H = 110$ mm

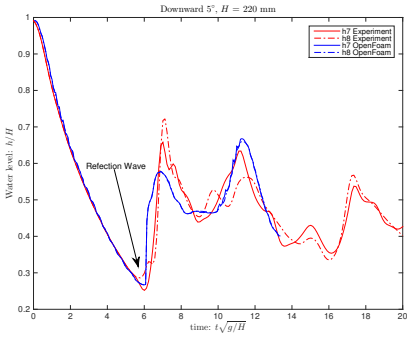

(d) Downward 5°, $H = 220$ mm

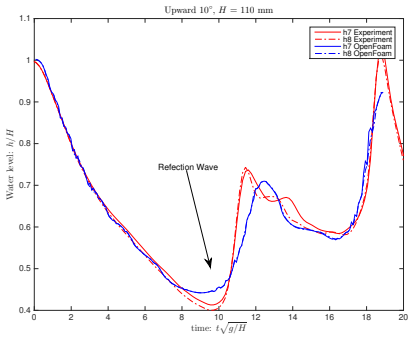

(e) Upward 10°, $H = 110$ mm

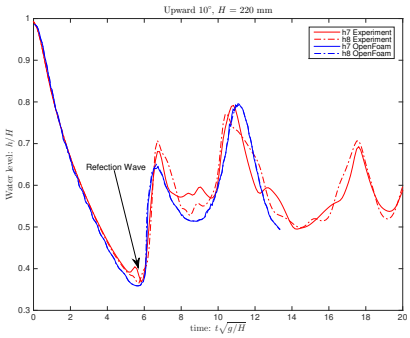

(f) Upward 10°, $H = 220$ mm

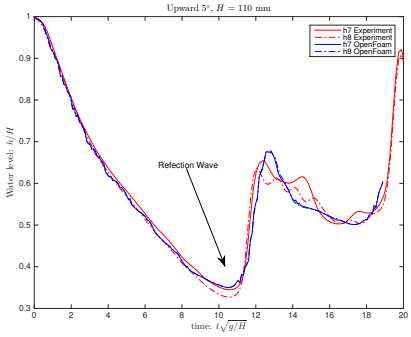

(g) Upward 5°, $H = 110$ mm

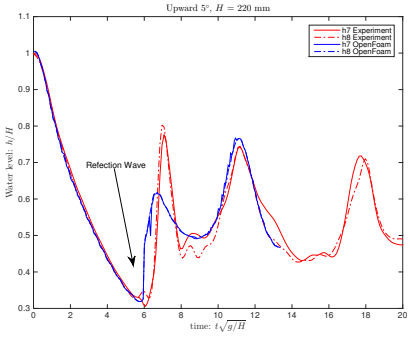

(h) Upward 5°, $H = 220$ mm

Figure 6.27: Elevation time history at wave probe location h7 and h8

6.4.2 Virtual wave probes

The image processing for water level detection (WLD) of the virtual wave probes is described in Appendix C.1. Fig. 6.28 shows the comparison of virtual wave probe h5 between the results of WLD and the previously published experimental data from LEE *et al.* [70], BUCHNER [6] and LOBOVSKỲ *et al.* [32].

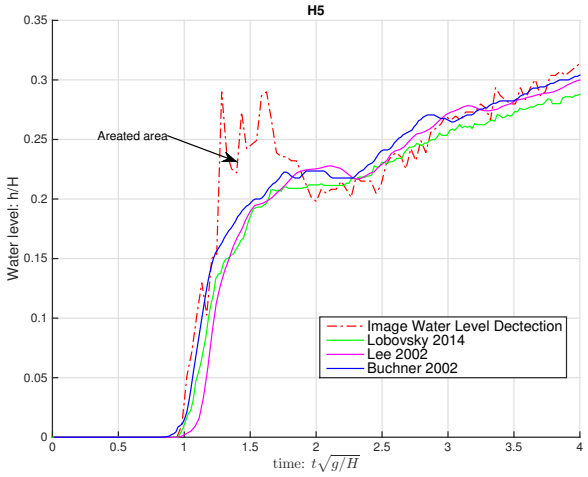

Figure 6.28: Elevation of virtual wave probe h5

Generally, the results of WLD agree with the other experimental data. However, when the wave front pass the virtual wave probe, the water level is over-estimated and with a higher variation. Physically, it is related to the aerated area at the wave front as shown in Fig. 6.29.

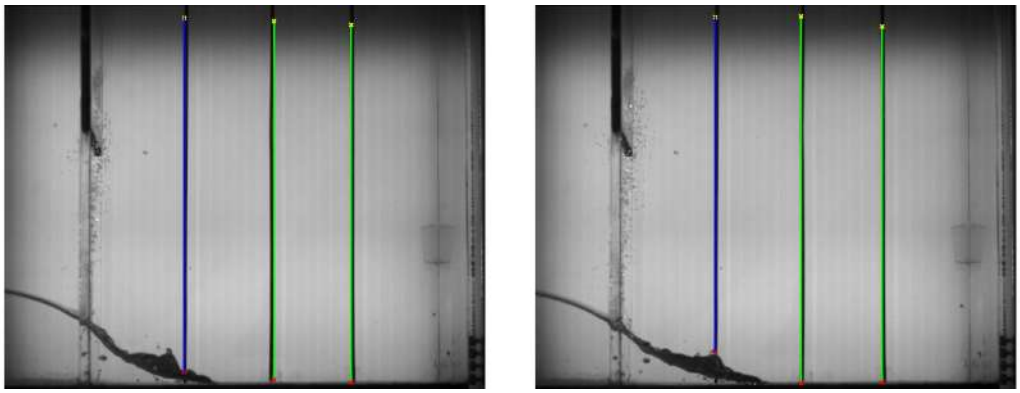

Figure 6.29: Water Level Dectection of h5 (the blue one) at time 120 ms (left) and 132 ms (right)

Similarly, Fig. 6.30 shows the WLD results of virtual wave probe h3 and the corresponded areated peak point at time 224 ms; Fig. 6.31 shows the WLD results of virtual wave probe h1 with the corresponded small areated front at time 212 ms.

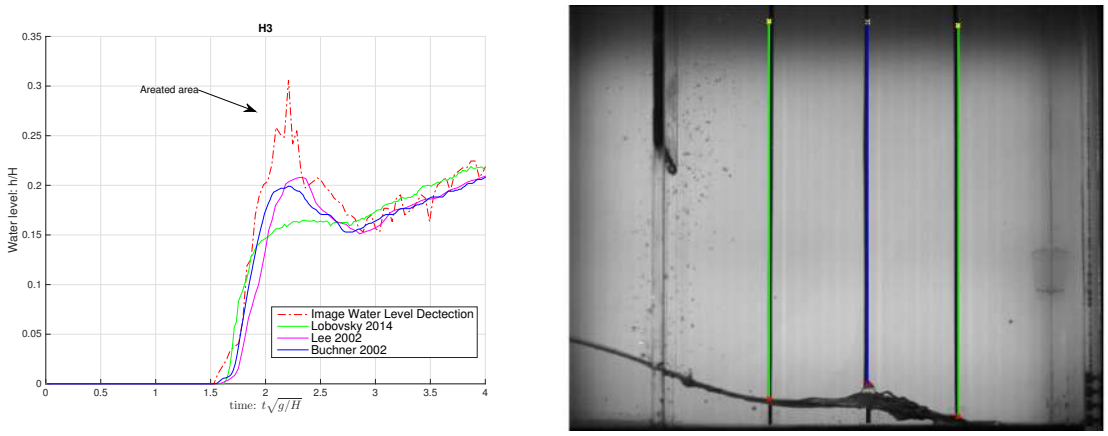

Figure 6.30: Elevation of virtual wave probe h3 (left) and the corresponded areated peak at time 224 ms (right)

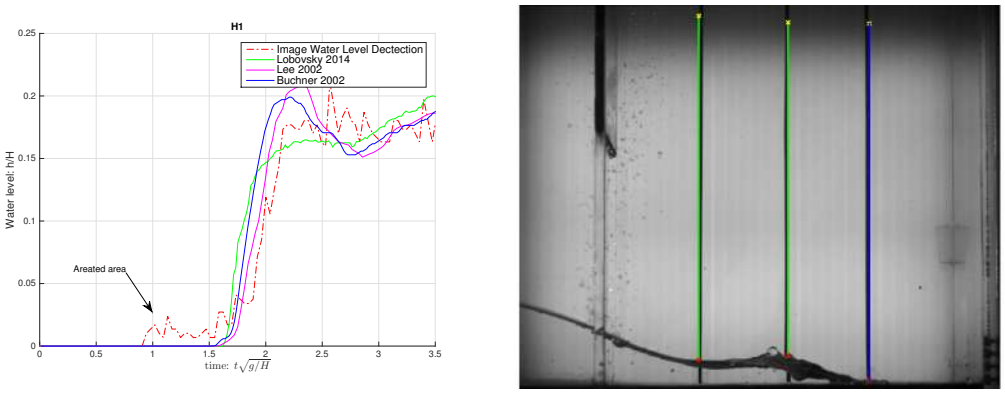

Figure 6.31: Elevation of virtual wave probe h1 (left) and the corresponded small areated front at time 212 ms (right)

Chapter 7

The BIV technique and the Application

The BIV technique can be used to obtain the velocity field of the dispersed phase. The technique correlates the fluid particles images and "texture" in the images created by the air-water interfaces. In this chapter, a test experiment was done.

This Chapter is structured as follows. The shape regimes of fluid particles together with the dimensionless groups are given first. After that the balance of force are evaluated with the equation of particle motion, namely the Basset-Boussinesq-Oseen (BBO) equation. With the BBO equation, the effects of the density ratio (particle to surrounding fluid) are evaluated. The velocity response for different particles in different fluid are given. Finally, the main capacity of the BIV system is formulated.

7.1 BIV test experiment

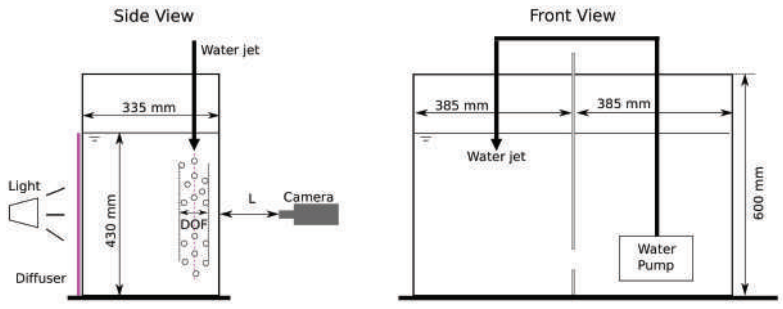

Figure 7.1: Schematic of the BIV test experiment

The BIV test experiment was constructed and installed in the LabOceano, as shown in Fig. 7.1. It consists of an acrylic tank and a water pump. The tank is made of 15 mm thick acrylic with inner dimensions of $780 \times 335 \times 600$ mm and was mounted

on a fixed platform. The water pump with water pipe (diameter of 2.8 cm) were used to generate a water jet impinging on the water surface. The impinging water jet entrained the air to the flow and generated lots of bubbles. The illumination of the flow used the shadowgraph concept. A 500 W (intensity adjustable) halogen light with a translucent light diffuser were set to the back side of the tank. A high speed camera was used in the front side to capture the shadow images of the flow. The distance (L) between the camera and tank was 287 mm. The focal length of the camera lens was 24 mm and the aperture number was 2.8. The resolution of the image was 1280×1024 pix and the frame rate was set to 250 FPS.

Fig. 7.2a shows an example image of bubbles generated by the impinging water jet. Two plastic rulers were sticked on the tank front surface. As can be observed, the field of view of image is about 171.3×136.6 mm. This provides a reference on the bubble size. To identify the bubbles, a software Image J (SCHNEIDER *et al.* [78]) was used. The image processing mainly includes three steps. In Fig. 7.2b, a FFT band-pass filter was applied to increase the intensity contrast. To remove the noise part (the rulers) for further processing, the images was cropped. By adjusting the threshold, the shadow of the bubbles are clearly shown in Fig. 7.2c. Finally, the bubbles are identified and shown in Fig. 7.2d. The bubble size statistics and its distribution diagram can then be obtained, as shown in Fig. 7.2e and Fig. 7.2f respectively. Assuming the bubble size follows the normal distribution, the mean bubble diameter is about 1.7 mm and the standard deviation is 1.01.

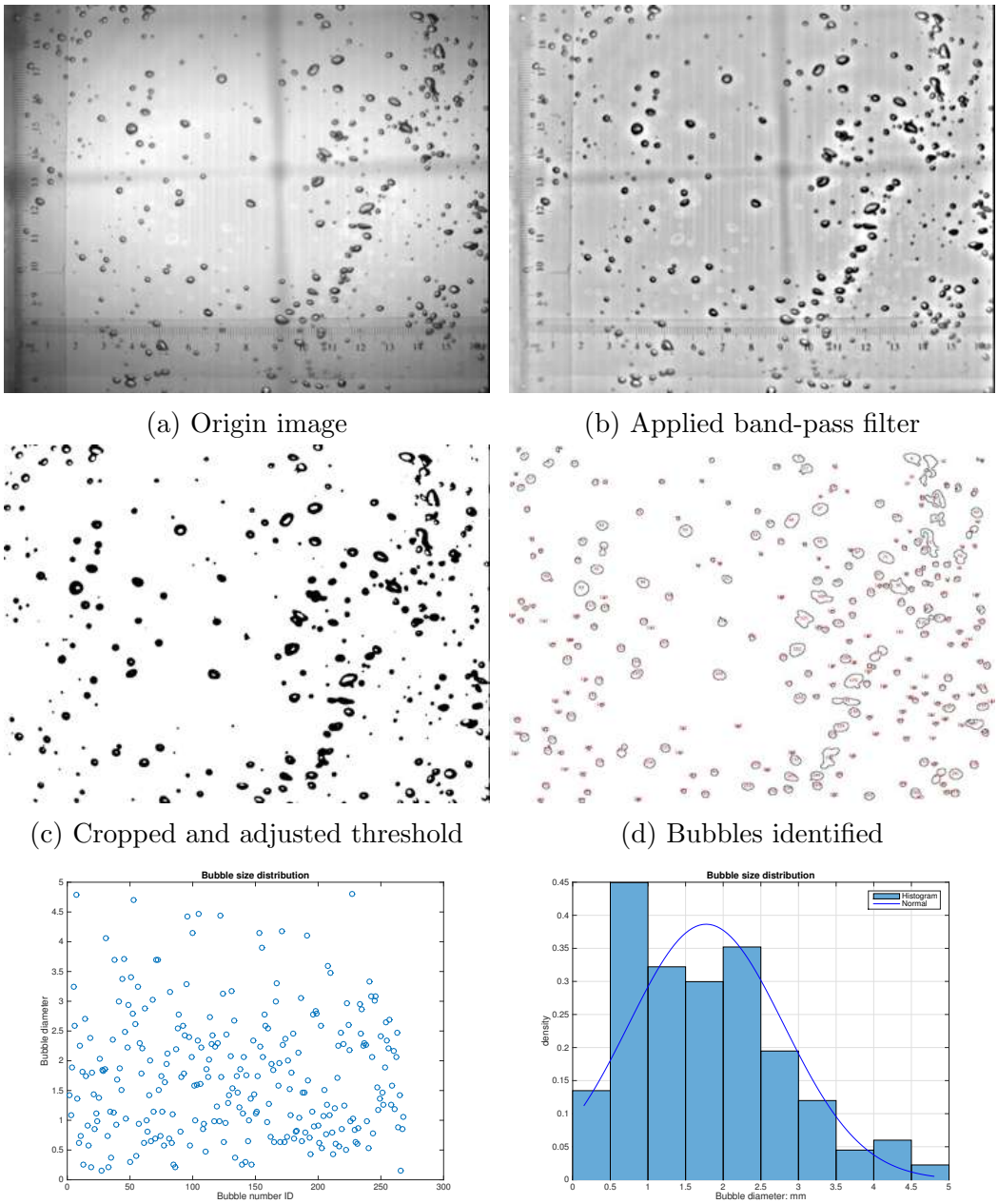

(a) Origin image (b) Applied band-pass filter

(c) Cropped and adjusted threshold (d) Bubbles identified

(e) Bubble size statistics (f) Bubble size distribution diagram

Figure 7.2: An example image and bubble identify process

The main information of the BIV test experiment is summarized in Table 7.1. To obtain the displacement of the particles, a cross-correlation algorithm is required. In the present work, we use a GUI-based open-source tool called PIVlab, available from THIELICKE and STAMHUIS [38]. PIVlab is programmed in MATLAB and additionally requires the image processing toolbox to run. A PIV analysis typically consists of three main steps image pre-processing, image evaluation, post-processing. The overview of the workflow and the implemented features of PIVlab are summarized in Fig. 7.3. The details of these implemented features are refered to THIELICKE and STAMHUIS [38] and would not be described here. The quality of

the PIV measurements in PIVlab was evaluated using synthetic particle images with known properties. Under optimal conditions (particle image diameter ≈ 3 pixels, particle density ≈ 5 - 15 particles/window, no noise, no particle pair loss, no motion blur, no shear), the bias error of the algorithm is smaller than 0.005 pixels and the random error is below 0.02 pixels.

Table 7.1: Summary of BIV test experiment

Calibration	
Distance of reference points l_r	1125 pix
Distance of reference image L_r	150 mm
Magnification factor α	0.134 mm/pix
Field of view	171.3×131.1 mm
Flow Visualization	
Average diameter of bubbles	1.67 mm
Camera resolution	1280×1024 pix
Gray scale resolution	8 bit
Frame rate per second	250
Time interval (Δt)	4 ms
Distance of lens to the target l_t	287 mm
Length of focus	24 mm
$f^{\#}$ number of lens	2.8
Data Processing	
Cross correlation method	FFT
First pass integration area size	64×64 pix
Second pass integration area size	64×64 pix
Subpixel analysis	3 points Gaussian fitting

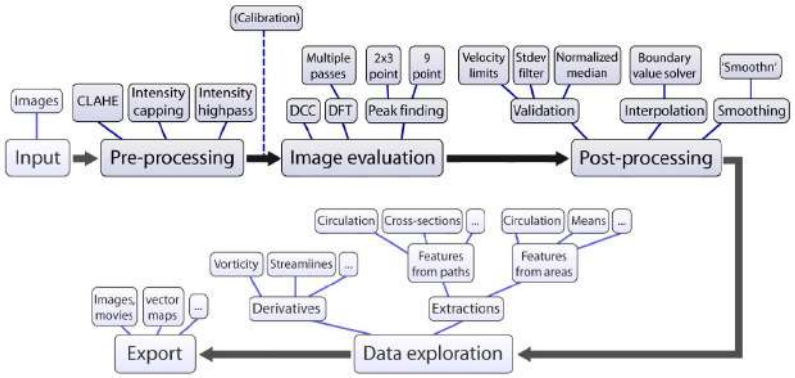

Figure 7.3: Workflow of PIVlab, adapted from THIELICKE and STAMHUIS [38]

Using the instant of Fig. 7.2a (t_0) as reference, the velocity fields in 4 ms obtained with PIVlab are shown in Fig. 7.4a to Fig. 7.4d, where the time increment equals to 1 ms. In general, at the right part of these figures, the bubble motion is mainly downward due to the impinging jet; while at the left part, the bubbles are mainly rising.

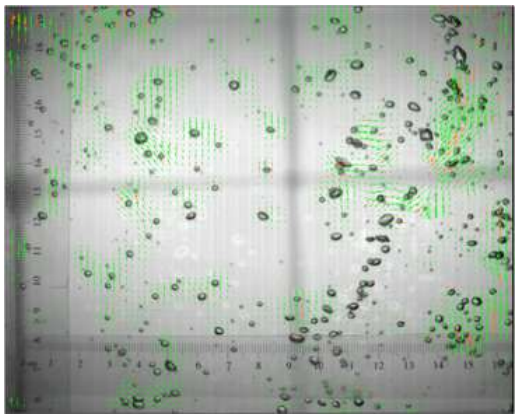

(a) Velocity fields at instant of t_0 (Fig. 7.2a)

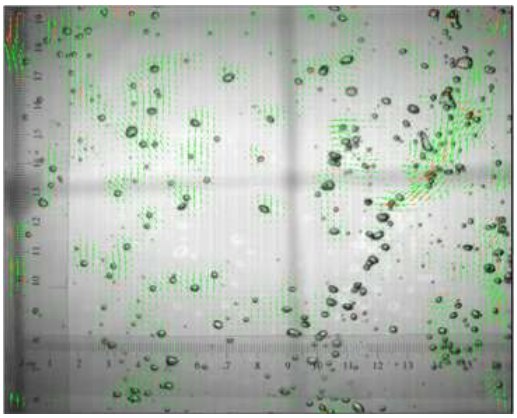

(b) Velocity fields at instant of $t_0 + 1$ ms

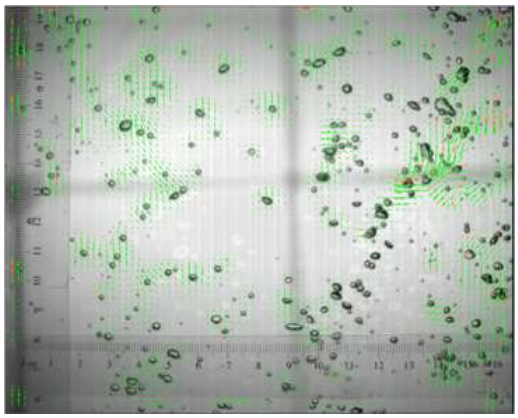

(c) Velocity fields at instant of $t_0 + 2$ ms

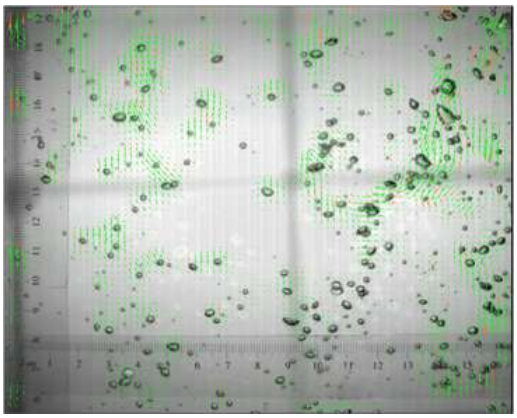

(d) Velocity fields at instant of $t_0 + 3$ ms

Figure 7.4: An example of the output velocity fields

7.1.1 System capacity

The usefulness of a PIV instrument is often characterized by its uncertainty. Since BIV is a direct adoption of the PIV technique, a brief uncertainty analysis of BIV is included in Appendix D.1, following the ITTC Recommended Procedures and Guidelines on PIV uncertainty analysis (PARK *et al.* [20]). However, as demonstrated by ADRIAN [79], the uncertainty could not completely describe the capabilities of the system. There are another two related and equally important characteristics: dynamic velocity range (DVR) and dynamic spatial range(DSR).

The DVR is defined as the ratio of maximum velocity (u_{max}) that can be mea-

sured to minimum resolvable velocity.

$$DVR = \frac{u_{max}}{\sigma_u} \tag{7.1}$$

where σ_u is the minimum resolvable velocity, can be evaluated by the uncertainty analysis on u. It should be noted that the relative error in velocity can be evaluated as the reciprocal of DVR, e.g. for a system with DVR larger than 20, the relative error on u is less than 5%.

The maximum velocity can be calculated as,

$$u_{max} = \frac{\Delta x_{max}}{\Delta t} = \frac{\Delta X_{max}}{M \Delta t} \tag{7.2}$$

wher Δx and ΔX are the displacements, lower case letters refer to quantities in the fluid and upper case letters denote quantities on the image and M is the magnification factor, in pix/mm. To avoid loss of correlation due to excessive in-plane displacement, KEANE and ADRIAN [80] state that the displacement should be smaller than one quarter of the interrogation window size D_I:

$$\frac{\Delta X_{max}}{D_I} \leq \frac{1}{4} \tag{7.3}$$

Thus the maximum displacement could be assumed as $\Delta X_{max} = \frac{1}{4} D_I$. In our setup, the images are captured by the high speed camera. The time interval between two neighbor frames can be assumed as uniform, thus Δt can be evaluated with the reciprocal of frames per second (FPS). It then gives,

$$DVR = \frac{FPS \ D_I}{4 M \sigma_u} \tag{7.4}$$

The DSR can be defined as the field-of-view (FOV) in the object space divided by the smallest resolvable spatial variation.

$$DSR = \frac{l_x}{\Delta x_{max}} \tag{7.5}$$

where l_x is FOV in x direction and minimum resolvable spatial variation can be estimated as Δx_{max}. If the working distance of the camera is constrained, l_x is proportional to the camera sensor chip size S_x. To have a large DVR on a BIV system, it is recommended to use a camera with large chip size.

For the BIV test experiment, Fig. 7.5a shows the relationship between the uncertainty on u with the average bubble diameter d_p and Fig. 7.5b shows the relationship of the dynamic range (DVR and DSR) against the average bubble diameter. For $d_p = 1.7$, the uncertainty on velocity (σ_u) is about 60.64 mm/s, DVR is about 13,

DSR is about 53. Generally, the uncertainty and DVR is a function of average bubble diameter. From the uncertainty analysis, it can be found that in BIV the bubble diameter is much larger than the seeding particles used in PIV and it becomes a main error source. Generally, to improve the uncertainty, the best way is using the BIV technique for small bubbles. In addition, small bubble diameter means large DVR while DSR is independent of bubble diameter and related to camera characteristics (the sensor size).

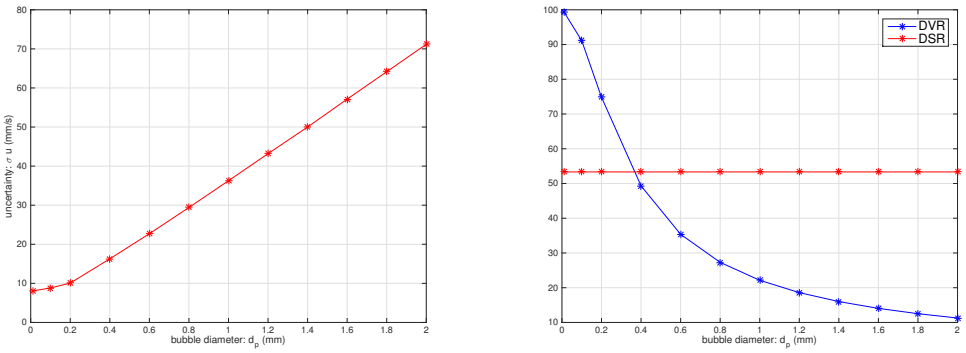

(a) Uncertainty and average bubble diameter

(b) Dynamic range and average bubble diameter

Figure 7.5: Results for the test experiment

7.2 Considerations on bubble/drops properties

In contrast to the PIV technique using the solid seeding particles, the concept of the so-called BIV technique proposed by RYU *et al.* [15] used the bubble itself as tracer. The characteristics of the bubble are quite different from the solid particles. This requires a good understanding on the properties on the dispersed phase. Following common usage, dispersed phase is a distinct state of matter (the particles) in a system, separated from other material by the phase boundary and the "continuous phase" is refer to the fluid surrounding the particles.

In this work, the "particle" is some kind self-contained body, with dimension range about 0.5 μm (PIV seeding particles) to several millimeters (large air bubbles or drops), separated from the surrounding fluid by a recognizable interface. "solid particles", "bubbles", "drops" are particles whose dispersed phases are in the solid state, gas state and liquid state respectively. Together, "bubbles" and "drops" comprise the "fluid particles". As documented in RAFFEL *et al.* [16], the main requirements on PIV seeding particles are related to the following properties, namely particle dimension size, particle density, particle light scatter characteristic, particle distribution. As discussed in the previous section, the specific light scatter characteristic of bubble has been taking into consideration by the shadowgraphy technique.

Following the concept of PIV, the particle density distribution are assumed to be medium. Beside this, the particle dimension size and particle density are the main aspects with regards to measurement accuracy and would be explored in the present Chapter. To distinguish the properties of the dispersed (or particle) phase from the continuous (or fluid) phase, subscripts "p" and "f" are used respectively.

7.2.1 Shape regimes of the fluid particles

In the absence of other forces or constraints, the action of surface tension on bubbles and drops tends to preserve their spherical shape. However, under the influence of gravitational forces, bubbles and drops in free rise or fall in infinite media are generally grouped in three different regimes CLIFT *et al.* [81]: spherical, ellipsoidal, and spherical cap, as shown in Fig. 7.6.

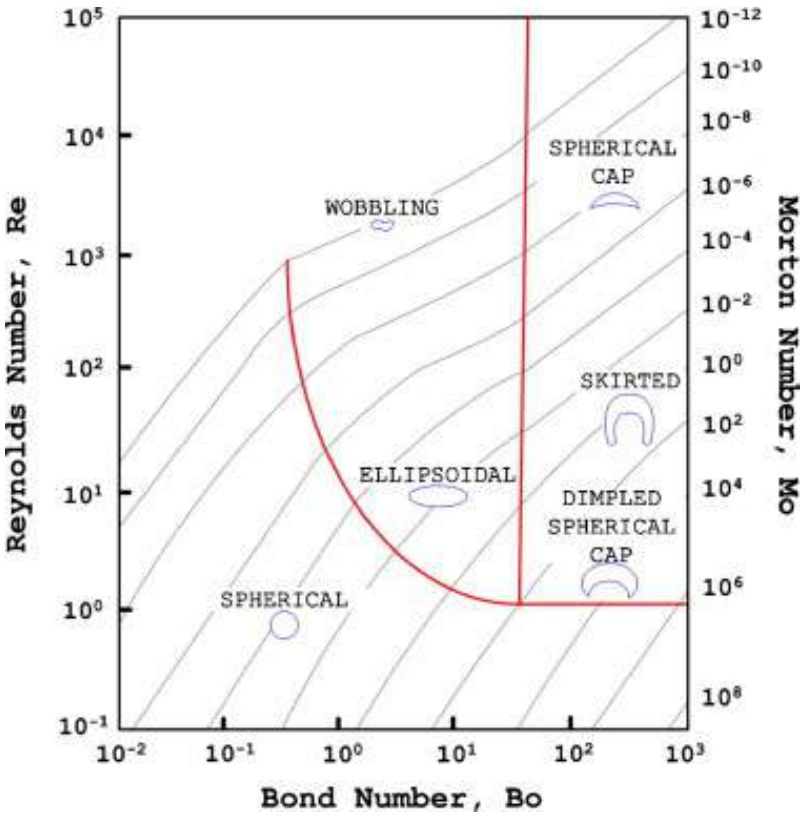

Figure 7.6: Shape regimes for bubbles and drops, adapted from CLIFT *et al.* [81]

Following AMAYA-BOWER and LEE [82], a brief description of the three main regimes provided as follows:

- Spherical regime:
  This regime is dominated by surface tension and viscous forces. Original size of the bubble is small, usually less than 1.3 mm. At low Re_T ($Re_T < 1$), bubbles and drops are spherical , regardless of the value of Bo; while at intermediate values of Re_t, bubbles and drops are spherical only when $Bo < 1$.

- Ellipsoidal regime:
  This regime is mainly dominated by surface tension. Bubble size is intermediate, typically from 1.3 to 6 mm. The range of Bond number is $0.25 < Bo < 40$ and the Re_T is usually large than 1.

- Spherical cap regime:
  This regime is governed by inertia force. Bubble size is large, usually bigger than 6 mm, with relative high Bond number $Bo > 40$ and Reynolds number $Re_T > 1.2$.

These regimes are depended on the following dimensionless groups, the Bond number (Bo) [1], the Morton number (Mo) and the terminal Reynolds number (Re_T) given by:

$$Bo = \frac{g\Delta\rho d_p^2}{\sigma} \tag{7.6}$$

$$Mo = \frac{g\mu_f^4\Delta\rho}{\rho_f^2\sigma^3} \tag{7.7}$$

$$Re_T = \frac{\rho_f d_p U_T}{\mu_f} \tag{7.8}$$

where ρ_f is the fluid density, $\Delta\rho = \rho_f - \rho_p$ is the density difference between the continuous phase (fluid) and the dispersed phase (particles), μ_f is the fluid viscosity, σ is the surface tension, g is the gravitational acceleration, and U_T is the terminal velocity of the fluid particles, defined as the steady velocity that the bubbles or drops reaches when there is a balance between buoyancy and drag forces.

The Bond number is the ratio of body forces and surface tension foces. Since Bond number is a funtion of the bubble diameter, proportional to d_p^2, it might also be considered as a dimensionless value of the particle size. The relationship between the fluid particles(bubbles/drops) diameter and the Bond number is shown in Fig. 7.7. Morton number provides a description of the properties of the surrounding fluid, mainly focusing in viscosity and surface tension. If the fluid properties are given, Morton number is a constant not affected by the particle diameter. The terminal Reynolds number depending on the terminal velocity is given the following section.

Terminal Reynolds number

According to CROWE *et al.* [83], the terminal velocity, U_T, is the final velocity a particle attains falling in a quiescent fluid. Various formulations of the terminal velocity have been presented in the literature.

[1] The Bond number is sometimes reffered to as Eötvös number.

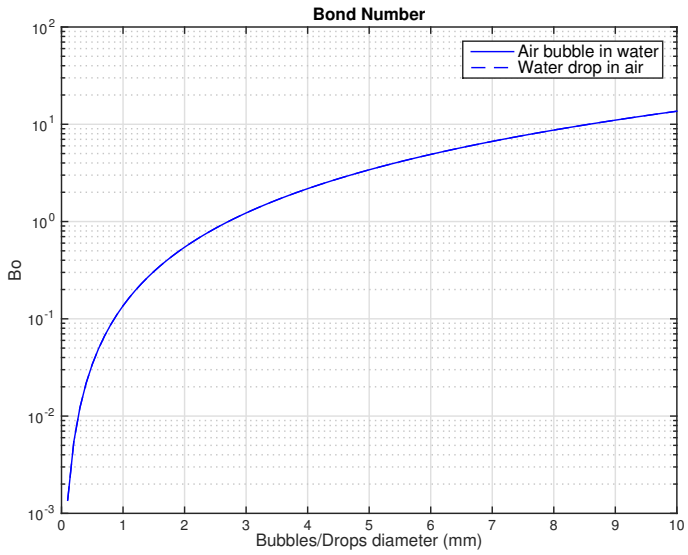

Figure 7.7: Bond number versus bubbles or drops diameter

One approach could follow AMAYA-BOWER and LEE [82], the terminal velocity is a combination of three main different shape regimes repectively to CLIFT *et al.* [81],

- Spherical regime (typically $d_p < 1.3mm$)
  The terminal velocity is proportional to size of the bubble, which can be described by HADAMARD [84] and RYBCZYNSKI [85] as follows:

$$U_T = \frac{g\Delta\rho d_p^2}{6\mu}\frac{1+\kappa}{2+3\kappa} \tag{7.9}$$

  where $\kappa = \dfrac{\mu_f}{\mu_g}$ is density ratio.

- Ellipsoidal regime:
  Terminal velocity is closely approximated by a correlation suggested by MENDELSON [86] based on wave theory, given as:

$$U_T = \sqrt{\frac{2.14\sigma}{\rho d_p} + 0.505 g d_p} \tag{7.10}$$

- Spherical cap regime:
  Terminal velocity of this regime can be described by a theory proposed by DAVIES and TAYLOR [87]:

$$U_T = \frac{2}{3}\sqrt{\frac{g\Delta\rho d_p}{2\rho}} \tag{7.11}$$

Another approach is an empirical relationship that fits the data for all three main regimes, as described in CROWE *et al.* [83]:

$$Re_T = \begin{cases} (\sqrt{22 + \sqrt{4.89Ga}} - \sqrt{22})^2 & \text{for } Ga < 4 \times 10^5 \\ 1.74\sqrt{Ga} & \text{for } 4 \times 10^5 < Ga < 3 \times 10^10 \end{cases} \tag{7.12}$$

where Ga is the Galileo number, defined as,

$$Ga = \frac{g d_p^3 (\frac{\rho_p}{\rho_f} - 1)}{\nu_f^2} \tag{7.13}$$

The terminal Reynolds number obtained from both approaches are shown in Fig. 7.8. To void the discontinuity, in the present work, the formulations by CROWE *et al.* [83] are used.

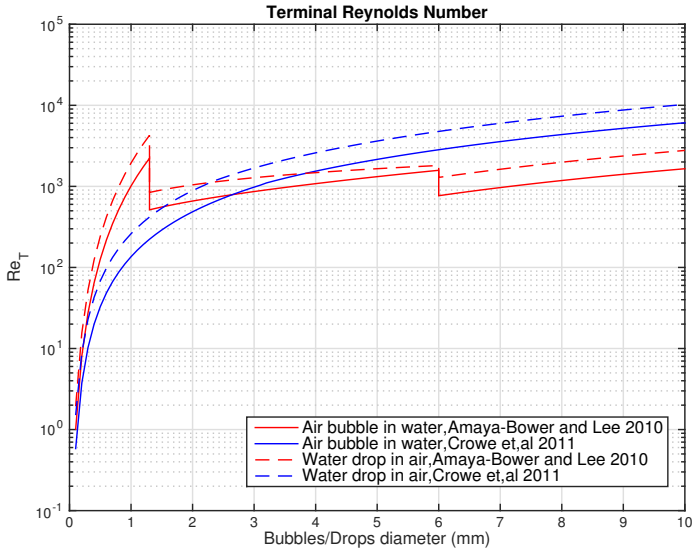

Figure 7.8: Terminal Reynolds number versus bubbles or drops diameter

In the present work, we considered the fluid particle (bubble/drops) dimension is up to several millimeters. From Fig. 7.6, the shape regimes are mainly spherical and ellipsoidal. Assuming the particle diameter of a ellipsoidal type can be estimated as a sphere with equivalent volume.The smaller the particle diameter, the closer to a sphere.

7.2.2 Equation of particle motion

One very important consideration in the PIV technique is that the seeding particles can follow the flow motion. However, the bubble motion is very sensitive to excitation by external forces at high frequencies owing to the small inertia compared to

the surrounding liquid. Questions may arise on whether the bubbles follow the fluid or not. In this section, we explore the equation of particle motion to evaluate the particle response in fluid.

Within the approximation of low Reynolds number, the equation of motion of a small spherical particle immersed in a fluid flow is given by MCKEON *et al.* [88] as:

$$\begin{aligned}\rho_p \frac{\pi d_p^3}{6}\frac{\mathrm{d}v_p}{\mathrm{d}t} = & \underbrace{\frac{\pi d_p^3}{6}(\rho_p - \rho_f)g}_{\text{term 1}} \\ & \underbrace{- 3\pi\mu d_p[(v_p - U) - \frac{1}{24}d_p^2\nabla^2 U]}_{\text{term 2}} \\ & \underbrace{+ \frac{\pi d_p^3}{6}\rho_f\frac{\mathrm{d}U}{\mathrm{d}t}}_{\text{term 3}} \\ & \underbrace{- \frac{\pi}{12}\rho_f d_p^3\frac{\mathrm{d}}{\mathrm{d}t}[(v_p - U) - \frac{1}{40}d_p^2\nabla^2 U]}_{\text{term 4}} \\ & \underbrace{- \frac{3}{2}d_p^2\sqrt{\pi\mu\rho_f}\int_{t_0}^{t}\frac{\mathrm{d}}{\mathrm{d}\xi}[(v_p - U) - \frac{1}{24}d_p^2\nabla^2 U)]\frac{\mathrm{d}\xi}{\sqrt{t-\xi}}}_{\text{term 5}}\end{aligned} \tag{7.14}$$

Eq. (7.14) is known as the Basset-Boussinesq-Oseen (BBO) equation. It describes the motion of - and forces on - a small particle in unsteady flow at low Reynolds numbers. The equation is named after Joseph Valentin Boussinesq, Alfred Barnard Basset and Carl Wilhelm Oseen. The first term in Eq. (7.14) is the body force (gravity minus buoyancy). The second term is a quasi-steady viscous force. The third term is the Froude-Krylov force due to the pressure gradient in the undisturbed flow. The fourth term is the added-mass force which is purely inertial. The fifth term is called the history force or Basset force. It is due to the diffusion of the vorticity from the particle surface to the bulk fluid flow.

The details of the derivation of the BBO equation can be found in CROWE *et al.* [83] and the solution of the BBO equation has been given by HJELMFELT JR and MOCKROS [89]. A more recent discussion of this equation and solution for turbulent flow has been given by MEI [90].

The $\nabla^2 U$ terms in Eq. (7.14) are normally small in comparison with any of the remaining terms and can be neglected. For very small particle tracers as used in PIV, the first part of the quasi-steady viscous force, the Stokes drag, dominates the right-hand side of the equation. The difference between the particle velocity v_p and

that of the surrounding fluid U can be estimated as,

$$v_p - U = \frac{d_p^2(\rho_p - \rho_f)}{18\mu}\frac{\mathrm{d}v_p}{\mathrm{d}t} \tag{7.15}$$

Clearly from the choice of neutrally buoyant particles $\rho_p \approx \rho_f$ leads to particle tracers that accurately follow the flow that $v_p \approx U$.

To simplify the problem, the unsteady forces (the Basset history force), the higher order term ($\nabla^2 U$) and the body force term are ignored, Eq. (7.14) becomes,

$$\rho_p \frac{\pi d_p^3}{6}\frac{\mathrm{d}v_p}{\mathrm{d}t} = \frac{\pi d_p^3}{6}\rho_f \frac{\mathrm{d}U}{\mathrm{d}t} - 3\pi\mu d_p(v_p - U) - \frac{\pi}{12}\rho_f d_p^3 \frac{\mathrm{d}(v_p - U)}{\mathrm{d}t} \tag{7.16}$$

To examine steady-state particle response to the oscillating flow of arbitrary sum of frequencies, we assume that velocity U can be represented as an infinite sum of harmonic functions as:

$$\begin{aligned} U(t) &= \int_0^\infty \Lambda_f(w)\exp(iwt)\mathrm{d}w \\ \frac{\mathrm{d}U(t)}{\mathrm{d}t} &= \int_0^\infty iw\Lambda_f(w)\exp(iwt)\mathrm{d}w \\ v_p(t) &= \int_0^\infty \Lambda_p(w)\exp(iwt)\mathrm{d}w \\ \frac{\mathrm{d}v_p(t)}{\mathrm{d}t} &= \int_0^\infty iw\Lambda_p(w)\exp(iwt)\mathrm{d}w \end{aligned} \tag{7.17}$$

Substituting Eq. (7.17) in Eq. (7.16), yields

$$\int_0^\infty \{S_t\Lambda_p i - S_t\gamma\Lambda_f i + (\Lambda_p - \Lambda_f) + \frac{S_t}{2}\gamma(\Lambda_p - \Lambda_f)i\}\exp(iwt)\mathrm{d}w = 0 \tag{7.18}$$

where S_t is the Stokes number defined as the ratio of the characteristic time of a particle (or droplet) τ_p to a characteristic time of the fluid τ_f and γ is the the density ratio,

$$S_t = \frac{\tau_p}{\tau_f} = \frac{\rho_p d_p^2 w}{18\mu} \tag{7.19}$$

$$\gamma = \frac{\rho_p}{\rho_f} \tag{7.20}$$

The Stokes number is a very important parameter in fluid-particle flows. If $S_t \ll 1$, the response time of the particles is much less than the characteristic time associated with the flow field. The particles will have enough time to respond to changes in flow velocity. Thus the velocity of the particle and the fluid velocity will be nearly equal. On the other hand, if $S_t \gg 1$ then the particle will essentially have no time to respond to the fluid velocity changes. Thus particle velocity will be affected and

not equal to the fluid velocity.

By solving Eq. (7.18) yields,

$$\frac{\Lambda_p}{\Lambda_f} = \frac{1 + i\frac{3S_t\gamma}{2}}{1 + i(S_t + \frac{S_t\gamma}{2})} \tag{7.21}$$

the velocity amplitude response could be defined as,

$$|\frac{v_p}{U}| = \sqrt{\frac{\Lambda_p\Lambda_p^*}{\Lambda_f\Lambda_f^*}} \tag{7.22}$$

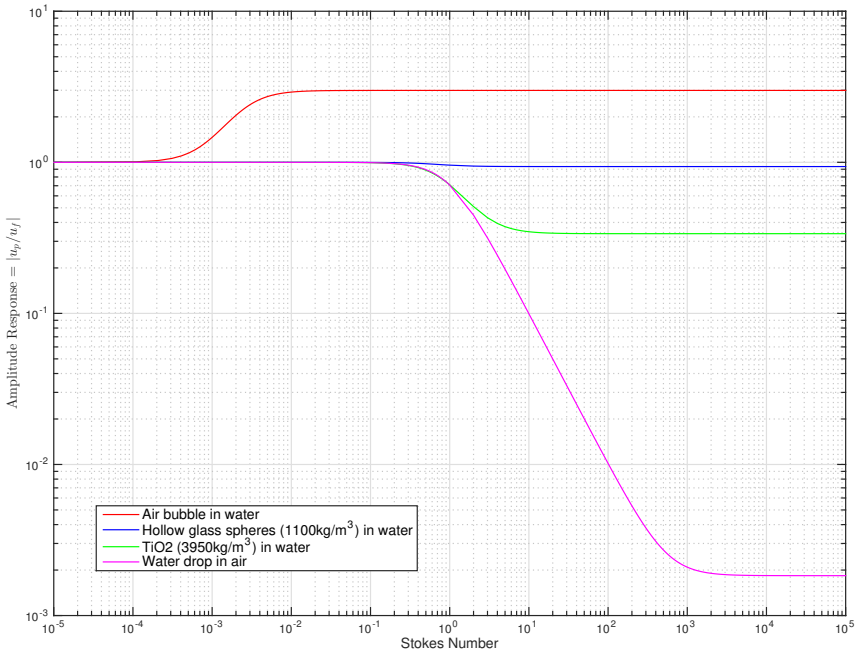

Figure 7.9: Velocity amplitude response versus Stokes number

Fig. 7.9 shows the relationship between the velocity amplitude response and the Stokes number. The velocity amplitude response could be used to quantify whether a particle follows the fluid or not. As one can imagine, light particles will follow the fluid better than the heavier particles. For common seeding particles applied in the PIV technique, the density ratio is usually larger than one ($\gamma < 1$). As can be observed in Fig. 7.9, the velocity response $|\frac{v_p}{U}| < 1$ and this is usually called "velocity lag". Comparing two type of seeding particles, the Hollow glass spheres (1100 kg/m^3) and the Titanium Dioxide (TiO_2) spheres (3950 kg/m^3), the velocity amplitude response of the light particles (Hollow glass spheres) is closer to one. The closer of the particle density to the fluid density, the better in following the flow.

When the particle density is not close to the fluid density, whether the particles

can be considered as following the flow is regards to the Stokes number. For heavier particles ($\gamma \gg 1$), e.g. water drops in air, if the Stokes number is less than 0.1, it may be regards as following the flow. On the other hand, for very light particles($\gamma \ll 1$), e.g. air bubbles in water, the situation is very different. The velocity response is generally larger than one ($|\frac{v_p}{U}| > 1$), which indicates that the bubble's velocity is generally over-response of the fluid. Only when the Stokes number is very small, less than 10^{-4}, the bubble can be regards as a good tracer.

7.3 Application of the BIV technique

Taking the advantage of the BIV technique, it is possible to obtain more information on the flow velocity field. In this section, we show some example results obtained using the BIV technique.

7.3.1 Example in the main period

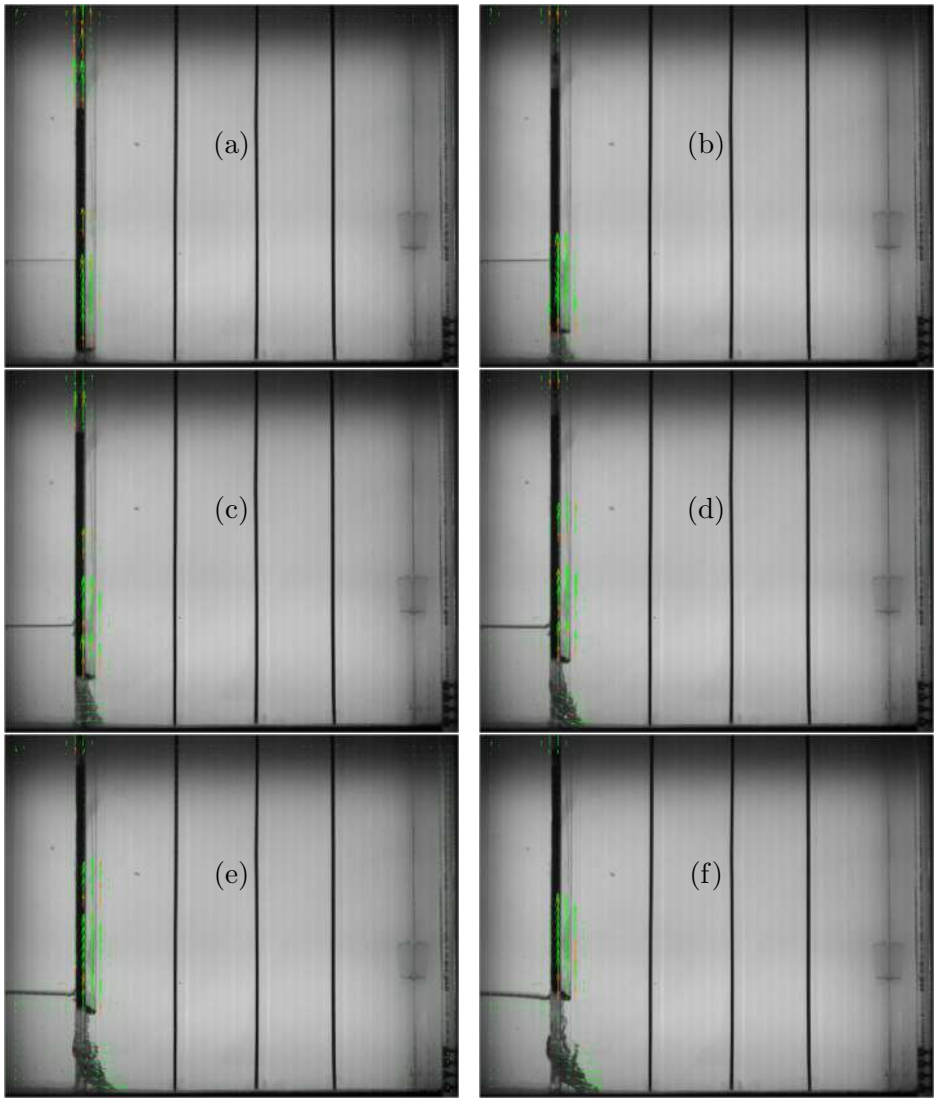

Figure 7.10: H=110 mm, BIV analysis velocity vectors in time 12, 20, 28, 36, 44, 52 ms

In the main period, the velocity field during the gate releasing stage can be obtained using the BIV technique. The velocity vectors of case H = 110 mm are shown in Fig. 7.10. It can be observed that the BIV technique detects not only on the flow velocity field but also on the gate releasing movement. The gate releasing velocity in time history is then shown in Fig. 7.11. It shows that once the gate was released, the gate velocity start to increase rapidly and later due to the non-uniform friction between the gate and the tank, there is a small variation of gate velocity. If the first 4 points in Fig. 7.11 are not accounted, the mean velocity equals to 2.11 m/s which is close to the average velocity V_g in Table 6.1 of case $H = 110$ mm.

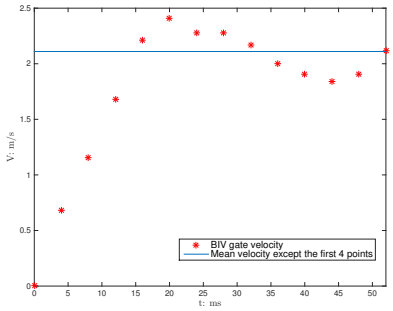

Figure 7.11: Gate releasing velocity in time history obtained with BIV

The front velocity is an important characteristic of the dam break wave. Since the flow is advancing in channel, the wave front is also developing in horizontal direction. Most velocity measurement techniques require to be mounted on certain location to measure the flow velocity on a single point, such as Pitot-tube, Hot Wire Anemometry (HWA) and Laser-Doppler Anemometry (LDA). They can not track the advancing wave front. Now with the BIV technique, it is possible to track the wave front velocity in time evolution, as shown in Fig. 7.12.

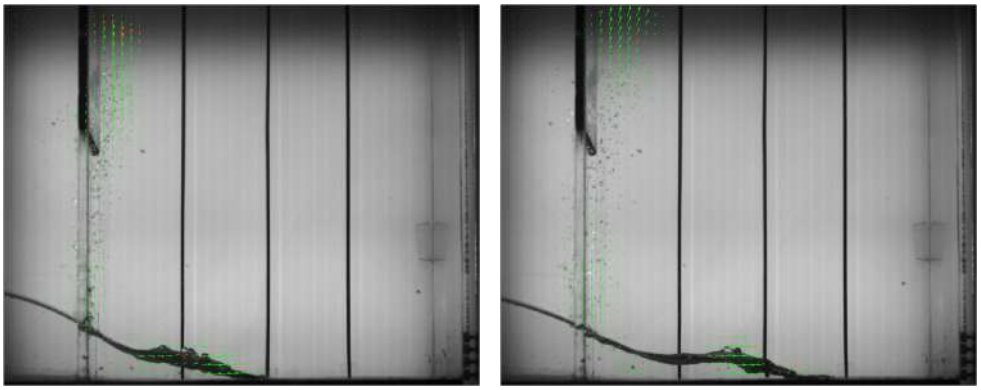

(a) At time $t = 158$ ms and $t^* = 1.50$ (b) At time $t = 198$ ms and $t^* = 1.89$

Figure 7.12: BIV results example during the runup

The results obtained by BIV technique are shown in Fig. 7.13, compared with numerical simulation results and analytical formulations summarized in Table 7.2.

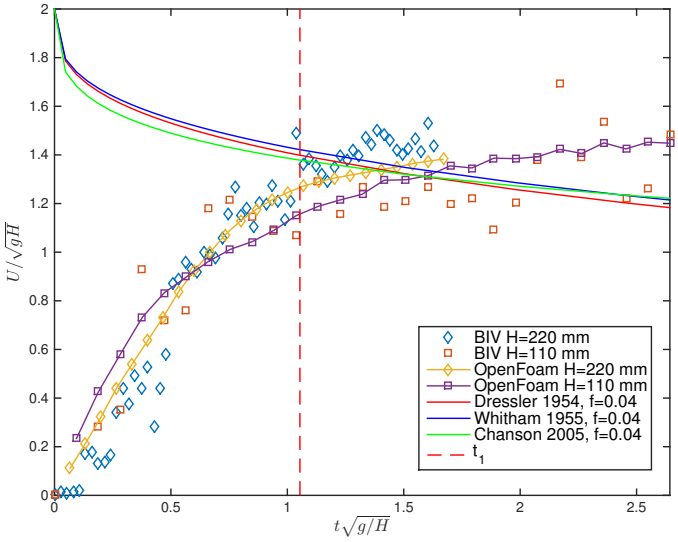

Figure 7.13: Wave front velocity time evolution

Table 7.2: Analytical approaches of front velocity with bottom friction effects

Reference	Asymptotic solution	Remarks
DRESSLER [31]	$\frac{U_F}{\sqrt{gH}} = 2 - 3.59(\frac{f}{8}\sqrt{\frac{g}{H}})^{\frac{1}{3}}$	first order approximation
WHITHAM [18]	$\frac{U_F}{\sqrt{gH}} = 2 - 3.452(\frac{f}{8}t\sqrt{\frac{g}{H}})^{\frac{1}{3}}$	first order approximation
CHANSON [19]	$\frac{1}{3}\frac{(1-\frac{U_F}{2\sqrt{gH}})^3}{\frac{f}{8}\frac{U_F^2}{gH}} = t\sqrt{\frac{g}{H}}$	exact solution

It can be observed that although there is some variation in the the front velocity results extracted with BIV technique, the general trends of the BIV results agree with OpenFOAM simulation results for both cases of $H = 110$ mm and $H = 220$ mm. Initially the water is at rest, once the dam gate is released, the front velocity starts increasing. The main acceleration range may be considered as interval $[0, t_1^*]$, as can be observed form Fig. 7.13. During this interval, the wave front velocity increases rapidly and after time t_1^*, the front velocity increases slowly. Taking the advantage of BIV technique, the average dimensionless velocity of the downstream wave front after time $t > t_1^*$ are obtained. The results are shown in Table 7.3, in comparison to previously published data.

Table 7.3: The average dimensionless wave front velocity for time $t > t_1^*$

Reference and case (mm)	$U/\sqrt{gH}$
Present case H=110	1.33
Present case H=220	1.41
LOBOVSKỲ *et al.* [32] H=300	1.56
LOBOVSKỲ *et al.* [32] H=600	1.34
MARTIN and MOYCE [91] H=57	1.48
MARTIN and MOYCE [91] H=114	1.69

In the classical ESS, the bottom friction is neglected and the downstream wave front velocity is constant equals to $2\sqrt{gH}$. However, in reality, due to the bottom friction effects, the wave front velocity is not constant but a function of time, as can be observed from Fig. 7.13. These analytical formulations in Table 7.2 include the bottom friction effects (represented by f, as described in Section 3.2.1), but they are all based on the ESS. Thus it is not surprised that they all have the common discontinuity at time $t = 0_+$, the wave front velocity jumps from zero to $2\sqrt{gH}$. Due to this discontinuity, it is could be observed that these formulations overestimate the wave front velocity in the interval $[0, t_1^*]$ too much; while for time larger than t_1^*, they are closer to BIV results and simulation results.

7.3.2 Example in the impact period

In the impact period, the BIV technique may be used to evaluate the runup process. Fig. 7.14 shows the example results at instant 358 ms and 382 ms obtained by the BIV technique. The main runup velocity field are captured, including the solid flow (the continuious phase) and some splashing water drops (the dispersed phase). It is should be noted in the left part of the tank, there are many drops the velocity field of which not captured. These water drops are mainly attached on the inner tank surface. The velocity of these water drops is relatively small to the uncertainty of BIV system and thus can not be captured by the algorithm.

(a) At time $t = 358$ ms and $t^* = 3.41$ (b) At time $t = 382$ ms and $t^* = 3.64$

Figure 7.14: BIV results example during the runup

7.3.3 Example in the reflection period

After the runup, the fluid is falling down. At time 646 ms, a breaking wave is generated and a vortex is detected, as shown in Fig. 7.15a. Due to the breaking wave advancing back, large mixed air-water area is generated. As shown in Fig. 7.15b, at time 752 ms, BIV technique detects velocity field including: falling water drops, bubbles, mixed air-water area and free surface.

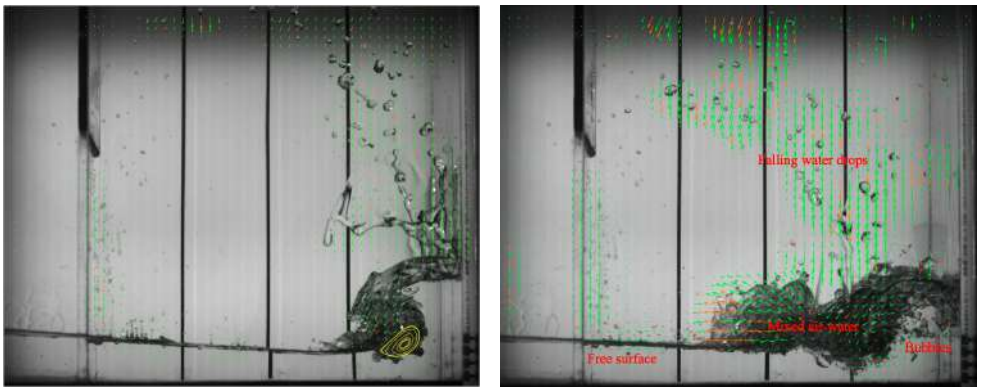

(a) At time $t = 646$ ms (b) At time $t = 752$ ms

Figure 7.15: BIV results example of the reflection wave

7.3.4 Notes on BIV technique application

It is should be noted that the original application of PIV/BIV is for the velocity fields for particles. However, it is found that the technique could be extended for falling water drops, bubbles, mixed air-water area and free surface as shown in Fig. 7.15b or even for dam gate releasing as shown in Fig. 7.10.

The reason of this extention may be explained as follows. According to HUANG *et al.* [92] and HUANG *et al.* [37], the cross-correlation algorithm of PIV is actually a image pattern matching technique. The image pattern is an image (of particles)

with a certain spatial distribution in a given space. This indicates that the cross-correlation algorithm is not only limited for small solid seeding particles but may also suitable for any certain distribution of objects. The object could be a group of deformable bubbles (or drops) and in a very short time (the time interval between a image pair) we assumes the deformation is neglectable, this yilds the BIV technique. The object could also be the shadow image of the mixed air-water area, the shadow image of a thin free surface or even the image of a moving gate.

Chapter 8

Conclusions and Future Work

8.1 Conclusions

The green water generated by extreme waves is primarily an air-water mixture, which includes a continuous phase and a dispersed phase. In this thesis, the continuous phase is mainly studied with the dam break model and the dispersed phase is mainly studied with the BIV technique.

8.1.1 Continuous phase

In the continuous phase, to introduce the bottom friction and the bed slope effects for shipping of water problem, the dam break model is explored by three main approaches, namely analytical, numerical and experimental.

- Analytically, an extended analytical dam break solution is proposed. The presented solution is a piecewise solution (PS) and consists of three parts: upstream part, downstream frictionless part and downstream wave tip part. PS assumes that incoming wave always comes horizontally and induces a horizontal dam in the upstream side. In the downstream side, PS assumes that the downstream elevation of a sloping bed case can be transformed from the elevation of the horizontal bed case.

- Numerically, the dam break simulations are based on the open source tool OpenFOAM version 2.3.0. The numerical dam break model solves the RANS equations with a $k - \varepsilon$ turbulence model.

- Experimentally, different dam break experiments were carried out, with one horizontal bed and four slope beds with different slope angles. Each bed was tested with two different water levels.

The acquired experimental data and the simulated numerical results agree well with the presented piecewise solution. Besides, based on the research presented in this thesis, the following conclusions seem to be justified:

- The initial stages of dam break is studied. The dam break period (before impact) could be divided into three different stages: the gate releasing stage, the transition stage and the later stage. The gate releasing stage is dominated by the vertical motion and this stage is better described with the Lagrangian Stoker solution; while the later stage of dam break wave is dominated by horizontal motion and this stage is better represented with the Eulerian Stoker solution. During the gate releasing stage, the "sudden dam break" concept is revised. The dam may be considered break suddenly when the dimensionless gate removal period is smaller than $\frac{3t_1^*}{5} \approx 0.63$.

- By introducing a time compensation factor $t_c^* = t_1^*/3$ into the PS, the tracking ability of downstream dam break wave front is greatly improved, where t_1 is the instant when the Eulerian and Lagrangian Stoker solutions have an intersection point at the dam section. The predicted downstream wave front by the PS agree well with experimental data on both wave front convex shape and the front location. Since t_c^* is introduced in the solution, the solution would not work for $t^* < t_c^*$. We recommend to use PS with t_c for time large than $\frac{3t_1^*}{5}$, that is after the "sudden dam break".

- To avoid the turbulent wakes induced by the wave probes in the downstream side, we introduced the virtual wave probes with a Water Level Detection (WLD) algorithm. A good agreement is found between the results of virtual wave probes and previously published data.

8.1.2 Dispersed phase

In the dispersed phase, the main goal is to evaluate the BIV technique. The special bubbles/drops characteristics about the BIV technique are evaluated. Mainly two characteristics of bubbles/drops are discussed: the particle density and the particle diameter. Based on the research presented in this thesis, the following conclusions seem to be justified:

- The density ratio (γ) between the particle and fluid affects the particle velocity response in fluid. The velocity response of bubbles/drops in the fluid is evaluated with the BBO equation. As shown in Fig. 7.9, in general, the velocity amplitude response between the particle and fluid is less than one for heavier particles ($\gamma \gg 1$, e.g. water drops in air), and larger than one for

lighter particles ($\gamma \ll 1$, e.g. air bubbles in water). Only when the Stokes number is sufficient small, the bubbles/drops can be regards as a good tracer of the fluid.

- The bubbles/drops diameter is another important factor for the BIV technique. By analyzing the shape regimes of bubbles/drops, it is found particles with the small diameter are closer to a spherical ideal tracer. Following the ITTC Recommended Procedures and Guidelines on PIV uncertainty analysis (PARK *et al.* [20]), it is found the bubble diameter is a very important factor which affects the uncertainty. What's more, the Stokes number is also a function of the particle diameter.

- The BIV technique is also applied to the dam break experiment. It is found that the technique could be used for the velocity measurement of falling water drops, bubbles, mixed air-water area and even gate releasing. For instance, the BIV technique can be used to measured wave front velocity. A good agreement is fount between BIV results and the numerical simulation data.

8.2 Future works

The relative motion between the ship and the incoming wave is an interesting but complicated topic. In the present work, the influence of the pitch motion is evaluated by a static pitch angle together with the dam break model. Further studies may consider more on the dynamic behavior of the pitch motion.

In the dam break model, the effects of the bottom friction are taking account with a constant friction factor. Although there are several empirical formulations to estimate the bottom friction factor, but these formulations works mainly for steady flow. For unsteady flow like the dam break wave, the investigation is not clear yet and requires further studies.

The classical PIV is applicable for the 2D velocity measurement. With the recent developments, the PIV technique now towards to the 3D measurement. There are various approaches developed to resolve the 3D velocity information. For instance, the defocusing PIV technique developed by PEREIRA *et al.* [93], PEREIRA and GHARIB [94], the synthetic aperture particle image velocimetry developed by BELDEN *et al.* [95], or the Tomographic PIV developed by ELSINGA *et al.* [96]. With the advances in the PIV technique, the BIV technique may also be extended into 3D velocity measurement.

Bibliography

[1] SCHØNBERG, T., RAINEY, R. "A hydrodynamic model of Green Water incidents", *Applied Ocean Research*, v. 24, n. 5, pp. 299 – 307, 2002. ISSN: 0141-1187.

[2] ERSDAL, G., KVITRUD, A., OTHERS. "Green water on Norwegian production ships". In: *The Tenth International Offshore and Polar Engineering Conference*. International Society of Offshore and Polar Engineers, 2000.

[3] LEONHARDSEN, R. L., ERSDAL, G., KVITRUD, A., et al. "Experience and Risk Assessment of FPSOs in Use on the Norwegian Continental Shelfi Descriptions of Events". In: *The Eleventh International Offshore and Polar Engineering Conference*. International Society of Offshore and Polar Engineers, 2001.

[4] MORRIS, W., MILLAR, J., BUCHNER, B. "Green water susceptibility of north sea FPSO/FSUs". In: *Proceedings of the 15th Conference on Floating Production Systems (FPS), London*, 2000.

[5] GODA, K., MIYAMOTO, T., YAMAMOTO, Y. "9. A Study of Shipping Water Pressure on Deck by Two-dimensional Ship Model Test", *Naval architecture and ocean engineering*, v. 17, pp. 120–135, 1979.

[6] BUCHNER, B. *Green Water on Ship-type Offshore Structures*. Doctoral thesis, Delft University of Technology, 2002.

[7] GRECO, M., FALTINSEN, O., LANDRINI, M. "Shipping of water on a two-dimensional structure", *Journal of Fluid Mechanics*, v. 525, pp. 309–332, 2005.

[8] RYU, Y., CHANG, K.-A., MERCIER, R. "Application of dam-break flow to green water prediction", *Applied Ocean Research*, v. 29, n. 3, pp. 128 – 136, 2007b. ISSN: 0141-1187.

[9] PHAM, X. P. *Green water and loading on high speed containerships*. Doctoral thesis, University of Glasgow, 2008.

[10] STOKER, J. J. *Water Waves*. Interscience Publishers, Inc., 1957.

[11] GRECO, M. *A two-dimensional study of green-water loading*. Doctoral thesis, 2001.

[12] STANSBY, P., CHEGINI, A., BARNES, T. "The initial stages of dam-break flow", *Journal of Fluid Mechanics*, v. 374, pp. 407–424, 1998.

[13] BUKREEV, V., GUSEV, A. "Initial stage of the generation of dam-break waves". In: *Doklady Physics*, v. 50, pp. 200–203. Springer, 2005.

[14] OERTEL, M., BUNG, D. B. "Initial stage of two-dimensional dam-break waves: Laboratory versus VOF", *Journal of Hydraulic Research*, v. 50, n. 1, pp. 89–97, 2012.

[15] RYU, Y., CHANG, K.-A., LIM, H.-J. "Use of bubble image velocimetry for measurement of plunging wave impinging on structure and associated greenwater", *Measurement Science and Technology*, v. 16, n. 10, pp. 1945, 2005a.

[16] RAFFEL, M., WILLERT, C., KOMPENHANS, J. *Particle Image Velocimetry: a practical guide*. Springer, 1998.

[17] LAUBER, G., HAGER, W. H. "Experiments to dambreak wave: Horizontal channel", *Journal of Hydraulic research*, v. 36, n. 3, pp. 291–307, 1998.

[18] WHITHAM, G. B. "The Effects of Hydraulic Resistance in the Dam-Break Problem", *Proceedings of the Royal Society of London. Series A. Mathematical and Physical Sciences*, v. 227, n. 1170, pp. 399–407, 1955.

[19] CHANSON, H. *Applications of the Saint-Venant Equations and Method of Characteristics to the Dam Break Wave Problem*. Relatório técnico, The University of Queensland, 2005.

[20] PARK, J., DERRANDJI-AOUAT, A., WU, B., et al. "Uncertainty analysis: particle imaging velocimetry". In: *ITTC Recommended Procedures and Guidelines, International Towing Tank Conference*, 2008.

[21] BUCHNER, B. "The impact of green water on FPSO design". In: *Offshore technology conference*. Offshore Technology Conference, 1995.

[22] HAMOUDI, B., VARYANI, K. "Significant load and green water on deck of offshore units/vessels", *Ocean Engineering*, v. 25, n. 8, pp. 715 – 731, 1998. ISSN: 0029-8018.

[23] STANSBERG, C., NIELSEN, F., OTHERS. "Nonlinear wave-structure interactions on floating production systems". In: *The Eleventh International Offshore and Polar Engineering Conference*. International Society of Offshore and Polar Engineers, 2001.

[24] GRECO, M., COLICCHIO, G., FALTINSEN, O. "Shipping of water on a two-dimensional structure. Part 2", *Journal of Fluid Mechanics*, v. 581, pp. 371–399, 2007.

[25] SUHARA, T., HIYAMA, H., KOGA, Y. "Shock pressure due to impact of water jet and response of elastic plates", *Trans W Jpn Soc Naval Archit*, v. 46, pp. 151–161, 1973.

[26] FONSECA, N., SOARES, C. G. "Experimental Investigation of the Shipping of Water on the Bow of a Containership", *Journal of Offshore Mechanics and Arctic Engineering*, v. 127, n. 4, pp. 322–330, 2005.

[27] ZHANG, S., YUE, D. K., TANIZAWA, K. "Simulation of plunging wave impact on a vertical wall", *Journal of Fluid Mechanics*, v. 327, pp. 221–254, 1996.

[28] WAGNER, H. "Über Stoss- und Gleitvergänge an der Oberfläche von Flüssigkeite", *Z. Angew. Mach. Mech.*, v. 12, n. 4, pp. 192–235, 1932.

[29] STANSBERG, C. T., HELLAN, O., HOFF, J., et al. "Green sea and water impact on FPSO: Numerical predictions validated against model tests". In: *ASME 2002 21st International Conference on Offshore Mechanics and Arctic Engineering*, pp. 801–808. American Society of Mechanical Engineers, 2002.

[30] STANSBERG, C. T., BERGET, K., HELLAN, O., et al. "Prediction of Green Sea Loads on FPSO in Random Seas". In: *The Fourteenth International Offshore and Polar Engineering Conference*. International Society of Offshore and Polar Engineers, 2004.

[31] DRESSLER, R. F. "Comparison of theories and experiments for the hydraulic dam-break wave", *Int. Ass. Sci. Hydrol. Publi.*, v. 38, n. 3, pp. 319–328, 1954.

[32] LOBOVSKỲ, L., BOTIA-VERA, E., CASTELLANA, F., et al. "Experimental investigation of dynamic pressure loads during dam break", *Journal of Fluids and Structures*, v. 48, pp. 407–434, 2014.

[33] ARIYARATHNE, K., CHANG, K.-A., MERCIER, R. "Green water impact pressure on a three-dimensional model structure", *Experiments in Fluids*, v. 53, n. 6, pp. 1879–1894, 2012. ISSN: 0723-4864.

[34] BUCHNER, B. "On the impact of green water loading on ship and offshore unit design". In: *The Sixth International Symposium on Practical Design of Ships and Mobile Units, Seoul*, pp. 1–430, 1995.

[35] OGAWA, Y., MINAMI, M., TANIZAWA, K., et al. "Shipping Water Load due to Deck Wetness". In: *Proceedings of The 20th International Offshore and Polar Engineering Conference*, 2002.

[36] MELLING, A. "Tracer particles and seeding for particle image velocimetry", *Measurement Science and Technology*, v. 8, n. 12, pp. 1406, 1997.

[37] HUANG, H., DABIRI, D., GHARIB, M. "On errors of digital particle image velocimetry", *Measurement Science and Technology*, v. 8, n. 12, pp. 1427, 1997.

[38] THIELICKE, W., STAMHUIS, E. "PIVlab–towards user-friendly, affordable and accurate digital particle image velocimetry in MATLAB", *Journal of Open Research Software*, v. 2, n. 1, 2014.

[39] BRÜCKER, C. "PIV in two-phase flows", *von Karman Institute for fluid dynamics, Lecture Series*, v. 1, 2000.

[40] DAVIS, G. E. "Scattering of light by an air bubble in water", *JOSA*, v. 45, n. 7, pp. 572–581, 1955.

[41] BRÖDER, D., SOMMERFELD, M. "A PIV/PTV system for analysing turbulent bubbly flows", v. 10, pp. 7, 2000.

[42] TOKUHIRO, A., MAEKAWA, M., IIZUKA, K., et al. "Turbulent flow past a bubble and an ellipsoid using shadow-image and PIV techniques", *International Journal of Multiphase Flow*, v. 24, n. 8, pp. 1383–1406, 1998.

[43] DIAS, I., REITHMULLER, M. "PIV in two-phase flows: simultaneous bubble sizing and liquid velocity measurements", pp. 71–85, 2000.

[44] LINDKEN, R., MERZKIRCH, W. "A novel PIV technique for measurements in multiphase flows and its application to two-phase bubbly flows", *Experiments in Fluids*, v. 33, n. 6, pp. 814–825, 2002. ISSN: 0723-4864.

[45] BRÖDER, D., SOMMERFELD, M. "Combined PIV/PTV-Measurements for the Analysis of Bubble Interactions and Coalescence in a Turbulent Flow", *The Canadian Journal of Chemical Engineering*, v. 81, n. 3-4, pp. 756–763, 2003.

[46] FUJIWARA, A., DANMOTO, Y., HISHIDA, K., et al. "Bubble deformation and flow structure measured by double shadow images and PIV/LIF", *Experiments in fluids*, v. 36, n. 1, pp. 157–165, 2004.

[47] SATHE, M. J., THAKER, I. H., STRAND, T. E., et al. "Advanced PIV/LIF and shadowgraphy system to visualize flow structure in two-phase bubbly flows", *Chemical Engineering Science*, v. 65, n. 8, pp. 2431–2442, 2010.

[48] RYU, Y., CHANG, K.-A., MERCIER, R. "Runup and green water velocities due to breaking wave impinging and overtopping", *Experiments in Fluids*, v. 43, n. 4, pp. 555–567, 2007a. ISSN: 0723-4864.

[49] RYU, Y., CHANG, K.-A. "Green water void fraction due to breaking wave impinging and overtopping", *Experiments in fluids*, v. 45, n. 5, pp. 883–898, 2008.

[50] YILMAZ, O., INCECIK, A., HAN, J. "Simulation of green water flow on deck using non-linear dam breaking theory", *Ocean Engineering*, v. 30, n. 5, pp. 601 – 610, 2003. ISSN: 0029-8018.

[51] DRESSLER, R. F. "Hydraulic resistance effect upom the dam-break functions", *Journal of Research of the National Bureau of Standards*, v. 49, n. 3, pp. 217–225, September 1952.

[52] HUNT, B. "Asymptotic solution for dam-break problem", *Journal of the Hydraulics Division*, v. 108, n. 1, pp. 115–126, 1982.

[53] CHANSON, H. *The Hydraulics of Open Channel flow: An Introduction*. Butterworth-Heinemann, 2004.

[54] JASAK, H., JEMCOV, A., TUKOVIC, Z. "OpenFOAM: A C++ library for complex physics simulations". In: *International workshop on coupled methods in numerical dynamics*, v. 1000, pp. 1–20, 2007.

[55] JASAK, H. "OpenFOAM: Open source CFD in research and industry", *International Journal of Naval Architecture and Ocean Engineering*, v. 1, n. 2, pp. 89–94, 2009.

[56] RUSCHE, H. *Computational fluid dynamics of dispersed two-phase flows at high phase fractions*. Doctoral thesis, Imperial College London (University of London), 2003.

[57] RHIE, C., CHOW, W. "Numerical study of the turbulent flow past an airfoil with trailing edge separation", *AIAA journal*, v. 21, n. 11, pp. 1525–1532, 1983.

[58] KÄRRHOLM, F. P. *Numerical modelling of diesel spray injection, turbulence interaction and combustion*. Doctoral thesis, Chalmers University of Technology Gothenburg, 2008.

[59] LAUNDER, B. E., SPALDING, D. "The numerical computation of turbulent flows", *Computer methods in applied mechanics and engineering*, v. 3, n. 2, pp. 269–289, 1974.

[60] HIRT, C. W., NICHOLS, B. D. "Volume of fluid (VOF) method for the dynamics of free boundaries", *Journal of computational physics*, v. 39, n. 1, pp. 201–225, 1981.

[61] BRACKBILL, J., KOTHE, D. B., ZEMACH, C. "A continuum method for modeling surface tension", *Journal of computational physics*, v. 100, n. 2, pp. 335–354, 1992.

[62] JASAK, H. *Error analysis and estimation for the finite volume method with applications to fluid flows*. Doctoral thesis, Imperial College London (University of London), 1996.

[63] GREENSHIELDS, C. J. "OpenFOAM® Programmers Guide", *foam. sourceforge. net/docs/Guidesa4/ProgrammersGuides. pdf*, 2015.

[64] FERZIGER, J. H., PERIĆ, M. *Computational methods for fluid dynamics*. Springer Berlin, 2002.

[65] ISSA, R. I. "Solution of the implicitly discretised fluid flow equations by operator-splitting", *Journal of computational physics*, v. 62, n. 1, pp. 40–65, 1986.

[66] ROACHE, P. J. "Perspective: a method for uniform reporting of grid refinement studies", *Transactions-American Society of Mechanical Engineers Journal of Fluids Engineering*, v. 116, pp. 405–405, 1994.

[67] ROACHE, P. J. "Quantification of uncertainty in computational fluid dynamics", *Annual review of fluid Mechanics*, v. 29, n. 1, pp. 123–160, 1997.

[68] RICHARDSON, L. F., GAUNT, J. A. "The deferred approach to the limit. Part I. Single lattice. Part II. Interpenetrating lattices", *Philosophical Transactions of the Royal Society of London. Series A, containing papers of a mathematical or physical character*, v. 226, pp. 299–361, 1927.

[69] STERN, F., WILSON, R. V., COLEMAN, H. W., et al. "Comprehensive approach to verification and validation of CFD simulations-Part 1: methodology and procedures", *Transactions-American Society of Mechanical Engineers Journal of Fluids Engineering*, v. 123, n. 4, pp. 793–802, 2001.

[70] LEE, T.-H., ZHOU, Z., CAO, Y. "Numerical simulations of hydraulic jumps in water sloshing and water impacting", *Journal of Fluids Engineering*, v. 124, n. 1, pp. 215–226, 2002.

[71] SOUTO-IGLESIAS, A., BOTIA-VERA, E., MARTÍN, A., et al. "A set of canonical problems in sloshing. Part 0: Experimental setup and data processing", *Ocean Engineering*, v. 38, n. 16, pp. 1823–1830, 2011.

[72] CHENG, W., MURAI, Y., SASAKI, T., et al. "Bubble velocity measurement with a recursive cross correlation {PIV} technique", *Flow Measurement and Instrumentation*, v. 16, n. 1, pp. 35 – 46, 2005. ISSN: 0955-5986.

[73] YEN, B. C. "Open channel flow resistance", *Journal of hydraulic engineering*, v. 128, n. 1, pp. 20–39, 2002.

[74] ROUSE, H. "Critical analysis of open-channel resistance", *Journal of the Hydraulics Division*, v. 91, n. 4, pp. 1–23, 1965.

[75] CHANSON, H. "Application of the method of characteristics to the dam break wave problem", *Journal of Hydraulic Research*, v. 47, n. 1, pp. 41–49, 2009.

[76] VASSILAKOS, G. J., STEGALL, D. E., TREADWAY, S. "Performance Evaluation of Pressure Transducers for Water Impacts". In: *28th Aerodynamic Measurement Technology, Ground Testing, and Flight Testing Conference including the Aerospace T&E Days Forum*, p. 3322, 2012.

[77] PISTANI, F., THIAGARAJAN, K. "Experimental measurements and data analysis of the impact pressures in a sloshing experiment", *Ocean Engineering*, v. 52, pp. 60–74, oct 2012. ISSN: 00298018.

[78] SCHNEIDER, C. A., RASBAND, W. S., ELICEIRI, K. W. "NIH Image to ImageJ: 25 years of image analysis", *Nature methods*, v. 9, n. 7, pp. 671, 2012.

[79] ADRIAN, R. J. "Dynamic ranges of velocity and spatial resolution of particle image velocimetry", *Measurement Science and Technology*, v. 8, n. 12, pp. 1393–1398, dec 1997. ISSN: 0957-0233.

[80] KEANE, R. D., ADRIAN, R. J. "Optimization of particle image velocimeters. I. Double pulsed systems", *Measurement science and technology*, v. 1, n. 11, pp. 1202, 1990.

[81] CLIFT, R., GRACE, J. R., WEBER, M. E. *Bubbles, drops, and particles*. Courier Corporation, 1978.

[82] AMAYA-BOWER, L., LEE, T. "Single bubble rising dynamics for moderate Reynolds number using Lattice Boltzmann Method", *Computers & Fluids*, v. 39, n. 7, pp. 1191–1207, aug 2010. ISSN: 00457930.

[83] CROWE, C. T., SCHWARZKOPF, J. D., SOMMERFELD, M., et al. *Multiphase flows with droplets and particles*. CRC press, 2011.

[84] HADAMARD, J. "Mouvement permanent lent dune sphere liquide et visqueuse dans un liquide visqueux", *CR Acad. Sci*, v. 152, n. 25, pp. 1735–1738, 1911.

[85] RYBCZYNSKI, W. "On the translatory motion of a fluid sphere in a viscous medium", *Bull. Acad. Sci., Cracow, Series A*, p. 40, 1911.

[86] MENDELSON, H. D. "The prediction of bubble terminal velocities from wave theory", *AIChE Journal*, v. 13, n. 2, pp. 250–253, 1967.

[87] DAVIES, R., TAYLOR, G. "The mechanics of large bubbles rising through extended liquids and through liquids in tubes". In: *Proceedings of the Royal Society of London A: Mathematical, Physical and Engineering Sciences*, v. 200, pp. 375–390. The Royal Society, 1950.

[88] MCKEON, B., COMTE-BELLOT, G., FOSS, J., et al. "Velocity, vorticity, and Mach number". In: *Springer Handbook of Experimental Fluid Mechanics*, Springer, pp. 215–471, 2007.

[89] HJELMFELT JR, A., MOCKROS, L. "Motion of discrete particles in a turbulent fluid", *Applied Scientific Research*, v. 16, n. 1, pp. 149–161, 1966.

[90] MEI, R. "Velocity fidelity of flow tracer particles", *Experiments in Fluids*, v. 22, n. 1, pp. 1–13, 1996.

[91] MARTIN, J., MOYCE, W. "Part IV. An experimental study of the collapse of liquid columns on a rigid horizontal plane", *Philosophical Transactions of the Royal Society of London A: Mathematical, Physical and Engineering Sciences*, v. 244, n. 882, pp. 312–324, 1952.

[92] HUANG, H., FIEDLER, H., WANG, J. "Limitation and improvement of PIV", *Experiments in Fluids*, v. 15, n. 3, pp. 168–174, 1993.

[93] PEREIRA, F., GHARIB, M., DABIRI, D., et al. "Defocusing digital particle image velocimetry: a 3-component 3-dimensional DPIV measurement technique. Application to bubbly flows", *Experiments in Fluids*, v. 29, n. 1, pp. S078–S084, 2000.

[94] PEREIRA, F., GHARIB, M. "Defocusing digital particle image velocimetry and the three-dimensional characterization of two-phase flows", *Measurement Science and Technology*, v. 13, n. 5, pp. 683, 2002.

[95] BELDEN, J., TRUSCOTT, T. T., AXIAK, M. C., et al. "Three-dimensional synthetic aperture particle image velocimetry", *Measurement Science and Technology*, v. 21, n. 12, pp. 125403, 2010.

[96] ELSINGA, G. E., SCARANO, F., WIENEKE, B., et al. "Tomographic particle image velocimetry", *Experiments in fluids*, v. 41, n. 6, pp. 933–947, 2006.

[97] BRADSKI, G., KAEHLER, A. "OpenCV", *Dr. Dobbs Journal of Software Tools*, 2000.

[98] BOUGUET, J.-Y. "Camera Calibration Toolbox for Matlab". .

[99] JÄHNE, B. *Digital image processing*. The Netherlands: Springer-Verlag, 2005.

[100] KATIYAR, S. K., ARUN, P. V. "Comparative analysis of common edge detection techniques in context of object extraction", *arXiv preprint arXiv:1405.6132*, v. 50, n. 11, pp. 68–78, feb 2014.

[101] BIPM, I., IFCC, I., IUPAC, I. "OIML. Evaluation of measurement data Guide to the expression of uncertainty in measurement JCGM 100: 2008 (GUM 1995 with minor corrections)". 2008.

Appendix A

Shallow Water Equations

A.1 Shallow Water Equations

The *Shallow Water Equations* (SWE) can be derived from equations of conservation of mass and conservation of momentum,the *Navier-Stokes Equations*.

$$\nabla \cdot \mathbf{u} = \mathbf{0} \tag{A.1}$$

$$\frac{\partial \mathbf{u}}{\partial t} + \mathbf{u} \cdot \nabla \mathbf{u} = \mathbf{g} - \frac{\nabla \mathbf{p}}{\rho} + \mu \nabla^{\mathbf{2}} \mathbf{u} \tag{A.2}$$

with the following assumption:

- Two-dimensional problem
- Newtonian in-compressible fluid
- Hydro-static pressure
- Body force only gravity
- Depth averaged velocity
- Viscous effects ignored

Conservation of mass

As shown in Fig. A.1,
$\xi = \xi(x, y, t)$ is the elevation of the free surface;
$b = b(x, y)$ is the bed slope,positive downward;
$h = h(x, y, t)$ is the total depth of the water.
Note that $h = \xi + b$.

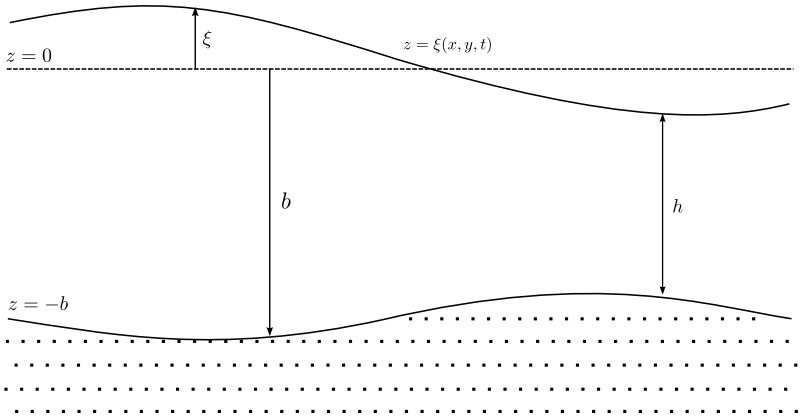

Figure A.1: A Typical Water Column

Now integrate the continuity Eq. A.1 from $z = -b$ to $z = \xi$. Since both b and ξ depend on t, x, and y, we apply the *Leibniz integral rule*: [1]

$$\begin{aligned} 0 &= \nabla \cdot \mathbf{v} \\ &= \int_{-b}^{\xi} (\frac{\partial u}{\partial x} + \frac{\partial v}{\partial y}) dz + w|_{z=\xi} - w|_{z=-b} \\ &= \frac{\partial}{\partial x} \int_{-b}^{\xi} u dz + \frac{\partial}{\partial y} \int_{-b}^{\xi} v dz - (u|_{z=\xi} \frac{\partial \xi}{\partial x} + u|_{z=-b} \frac{\partial b}{\partial x}) \\ &\quad - (v|_{z=\xi} \frac{\partial \xi}{\partial y} + v|_{z=-b} \frac{\partial b}{\partial y}) + w|_{z=\xi} - w|_{z=-b} \end{aligned} \tag{A.3}$$

Defining depth-averaged velocities as:

$$\bar{u} = \frac{1}{h} \int_{-b}^{\xi} u \mathrm{d}z, \quad \bar{v} = \frac{1}{h} \int_{-b}^{\xi} v \mathrm{d}z \tag{A.4}$$

Applying *Boundary Conditions* to get rid of the boundary terms.
at the free surface,

$$w = \frac{\partial \xi}{\partial t} + u \frac{\partial \xi}{\partial x} + v \frac{\partial \xi}{\partial y} \tag{A.5}$$

at the bottom,no slip condition,

$$u = v = w = 0 \tag{A.6}$$

So the depth-averaged continuity equation is:

$$\frac{\partial \xi}{\partial t} + \frac{\partial h\bar{u}}{\partial x} + \frac{\partial h\bar{v}}{\partial y} = 0 \tag{A.7}$$

[1] Let $f(x, \theta)$ be a function such that $f_\theta(x, \theta)$ exists, and is continuous.Then, $\frac{\mathrm{d}}{\mathrm{d}\theta} \left(\int_{a(\theta)}^{b(\theta)} f(x, \theta) \, \mathrm{d}x \right) = \int_{a(\theta)}^{b(\theta)} \partial_\theta f(x, \theta) \, \mathrm{d}x + f(b(\theta), \theta) b'(\theta) - f(a(\theta), \theta) a'(\theta)$

With the horizontal bottom, Eq. A.7 could be written as,

$$\frac{\partial h}{\partial t} + \frac{\partial h\bar{u}}{\partial x} + \frac{\partial h\bar{v}}{\partial y} = 0 \tag{A.8}$$

Conservation of momentum

Momentum Eq. A.2 in x direction could be written as,where τ_{vis} represents the viscous terms,

$$\frac{\partial u}{\partial t} + u\frac{\partial u}{\partial x} + v\frac{\partial u}{\partial y} = -\frac{1}{\rho}\frac{\partial p}{\partial x} + \tau_{vis} \tag{A.9}$$

Integrating the left-hand side of the x-momentum equation over depth, we get:

$$\int_{-b}^{\xi}[\frac{\partial u}{\partial t} + \frac{\partial u^2}{\partial x} + \frac{\partial uv}{\partial y}]\mathrm{d}z = \frac{\partial h\bar{u}}{\partial t} + \frac{\partial h\bar{u}^2}{\partial x} + \frac{\partial h\bar{u}\bar{v}}{\partial y} + \{dif.adv.terms\} \tag{A.10}$$

The differential advection terms account for the fact that the average of the product of two functions is not the product of the averages.($\overline{uv} \neq \bar{u}\bar{v}$)

Integrating the right-hand side of the x-momentum equation over depth, and assuming hydrostatic pressure $p = \rho g h$, we get:

$$\int_{-b}^{\xi}(-\frac{1}{\rho}\frac{\partial p}{\partial x} + \tau_{vis})\mathrm{d}z = -gh\frac{\partial h}{\partial x} + \int_{-b}^{\xi}\tau_{vis}\mathrm{d}z \tag{A.11}$$

Combining the LHS and RHS of the depth-integrated x-momentum equation,ignoring the differential advection terms and the viscous terms, we get:

$$\frac{\partial h\bar{u}}{\partial t} + \frac{\partial h\bar{u}^2}{\partial x} + \frac{\partial h\bar{u}\bar{v}}{\partial y} = -gh\frac{\partial h}{\partial x} \tag{A.12}$$

The result for y-momentum equation is similar,

$$\frac{\partial h\bar{v}}{\partial t} + \frac{\partial h\bar{u}\bar{v}}{\partial x} + \frac{\partial h\bar{v}^2}{\partial y} = -gh\frac{\partial h}{\partial y} \tag{A.13}$$

Combining the depth-integrated continuity Eq. A.8 with the depth-integrated x-momentum and y-momentum equations, the 2-D (nonlinear) *Shallow Water Equations* in non-conservative form are:

$$\begin{aligned}
&\frac{\partial h}{\partial t} + \frac{\partial h\bar{u}}{\partial x} + \frac{\partial h\bar{v}}{\partial y} = 0 \\
&\frac{\partial \bar{u}}{\partial t} + \bar{u}\frac{\partial \bar{u}}{\partial x} + \bar{v}\frac{\partial \bar{u}}{\partial y} = -g\frac{\partial h}{\partial x} \\
&\frac{\partial \bar{v}}{\partial t} + \bar{u}\frac{\partial \bar{v}}{\partial x} + \bar{v}\frac{\partial \bar{v}}{\partial y} = -g\frac{\partial h}{\partial y}
\end{aligned} \tag{A.14}$$

A.1.1 Saint Venant Equations

The 1-D form of *Shallow Water Equations* is also known as *Saint Venant Equations* (SVE). Where,the viscous term represents by the friction slope factor S_f, and gravity body force represents by the bottom slope factor S_0 ($S_0 = \sin\theta$):

$$\frac{\partial h}{\partial t} + \frac{\partial h\bar{u}}{\partial x} = 0 \tag{A.15}$$

$$\frac{\partial \bar{u}}{\partial t} + \bar{u}\frac{\partial \bar{u}}{\partial x} + g\frac{\partial h}{\partial x} = g(S_0 - S_f) \tag{A.16}$$

A.1.2 Method of Characteristics

A mathematical technique to solve the SVE is the method of characteristics. By introducing the propagation speed $c = \sqrt{gh}$, the SVE could be written as,

$$\begin{aligned} 2c_t + 2uc_x + cu_x &= 0 \\ u_t + uu_x + 2cc_x &= g(S_0 - S_f) \end{aligned} \tag{A.17}$$

The subtraction and addition of the partial differential Equations A.17 yields to ordinary differential equations called the *Characteristic Differential Equations*,

$$\begin{aligned} [\frac{\partial}{\partial t} + (u-c)\frac{\partial}{\partial x}] \cdot [u - 2c - g(S_0 - S_f)t] = 0 \\ [\frac{\partial}{\partial t} + (u+c)\frac{\partial}{\partial x}] \cdot [u + 2c - g(S_0 - S_f)t] = 0 \end{aligned} \tag{A.18}$$

Which leads to a characteristic system of two families: characteristic C_1 and characteristic C_2,

$$\begin{aligned} C_1 : \frac{\mathrm{d}x}{\mathrm{d}t} &= u + c \\ C_2 : \frac{\mathrm{d}x}{\mathrm{d}t} &= u - c \end{aligned} \tag{A.19}$$

along with the relations,

$$\begin{aligned} u + 2c - g(S_0 - S_f)t &= \text{const. along curve } C_1 \\ u - 2c - g(S_0 - S_f)t &= \text{const. along curve } C_2 \end{aligned} \tag{A.20}$$

The solution can be integrated from this characteristic system with the initial data.

Appendix B

Camera Calibration

B.1 camera calibration

In the present work, the camera was calibrated with a checkerboard pattern with square size equal to 40 mm. A set of calibration images with the checkerboard in different locations was recorded and one is shown in Fig. B.1a.

The calibration code developed for the present work was based on the OpenCV Toolbox by BRADSKI and KAEHLER [97]. The code first detects the checkerboard in the images and then calculates reprojection errors by projecting the checkerboard points from world coordinates (defined by the checkerboard) into image coordinates. The detected checkerboard points are represented in green circles while the red cross indicates the reprojected points, as shown in Fig. B.1b. The camera calibration accuracy can be examined by the reprojection errors.

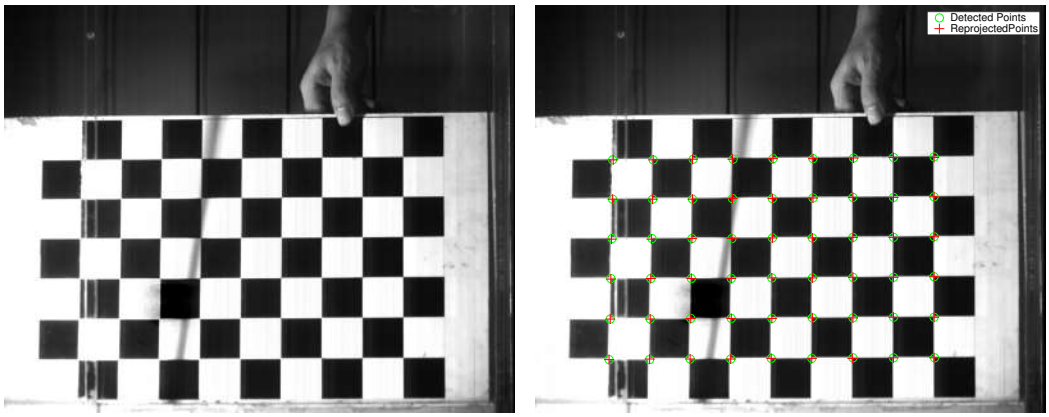

(a) original image (b) reprojected image

Figure B.1: camera calibration image example

The reprojection errors are the distances in pixels between the detected and the reprojected points. Reprojection errors provide a qualitative measure of accuracy. As a general rule, reprojection errors of less than one pixel are acceptable. As shown

in Fig. B.2, the mean reprojection error here is 0.27 pixel, considered to be small.

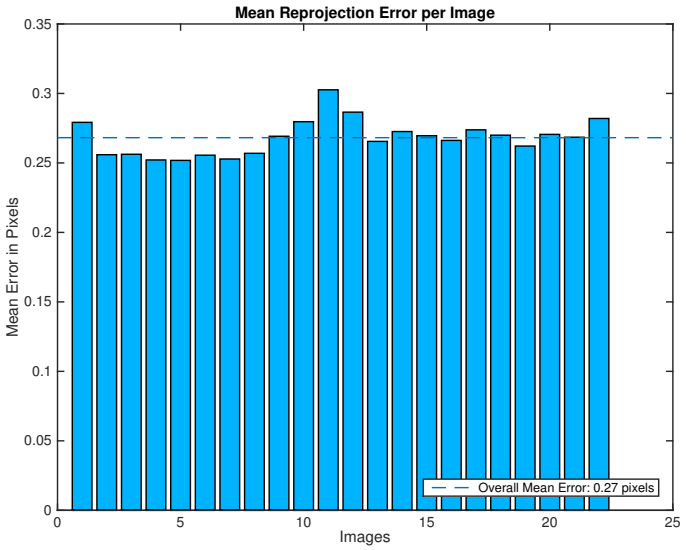

Figure B.2: camera calibration mean error

The relative positions between the camera and the checkerboard in the used calibration image sets are shown in Fig. B.3.

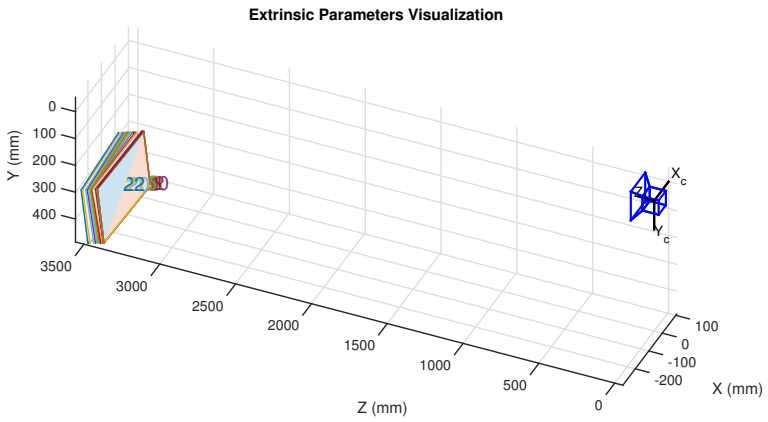

Figure B.3: camera calibration mean error

It is also important to note the calibration algorithm uses the camera model proposed by BOUGUET [98] which includes the radial and tangential lens distortion. The radial distortion occurs when light rays bend more near the edges of a lens than they do at its optical center. The smaller the lens, the greater the radial distortion. Tangential distortion occurs when the lens and the image plane are not parallel.

After calibration, all the images have been corrected for lens distortion. With the calibration results, the transformation from physical coordinates to the image coordinates was built. This allows further processing, for instance, plotting analytical solutions or numerical results over the experimental images.

Appendix C

Water Level Dectection

C.1 Algorithm for water level detection

The image processing of water level dectection is done with Computer Vision System Toolbox in Matlab version 2014 b. The algorithm mainly includes the following steps:

1. Image undistortion
2. Convert image to grayscale level
3. Edge detection
4. Increase the thickness of the dectected edge to enhance the performance of the Hough transformation
5. Find the longest line with Hough transformation in the edge image

First the image is undistorted based on the camera calibration as shown in Section B.1 and then converted to the grayscale level if necessary. The As shown in Fig. C.1, due to using the "AF DC-NIKKOR 105mm f/2D" lens, the image undistortion is quite small in this project. It can also be observed that in the downstream side, there are three black thin markers, which are called virtual wave probe in Section 5.3.1.

To dectect the water level at the given location, where the virtual wave probes located, the key is to identify the water level between the edge of the free surface and virtual wave probe. The edge dectection method is therefore applied. According to JÄHNE [99], mathematically speaking, an ideal edge is a discontinuity of the spatial gray value function $g(x)$ of the image plane. Edges characterize boundaries and are a problem of fundamental importance in image processing and particularly in automatic feature extraction. There are various edge detection algorithms. The

(a) Original Image (b) Undistorted Image

Figure C.1: Original

comparison between commonly used edge detection algorithms such as Sobel, Canny, Prewitt, Roberts, Laplacian and Zero Crossing could be found in KATIYAR and ARUN [100]. In general, Canny method performance better but its computational complexity is higher. The Sobel method also detects various features as Canny method but computationally more efficient. The other algorithms as Robert and Prewitt also detect the various features but fails in case of smaller features and the range of usable threshold is very low. Therefore, the Sobel method is choosed as the edge detection algorithm.

Figure C.2: Edge dectected with Sobel method

The results of Soble method is shown in Fig. C.2, the main edges features have been captured. It is also clealy observed that the virtual wave probes lines break at the free surface. It is possible to measure the water level based on the wave probe line length. To identify those virtual wave probe lines, the Standard Houth transform (SHT) is applied. To improve the performance of SHT, the egde thickness

is dilated before the SHT algorithm, as shown in Fig. C.3

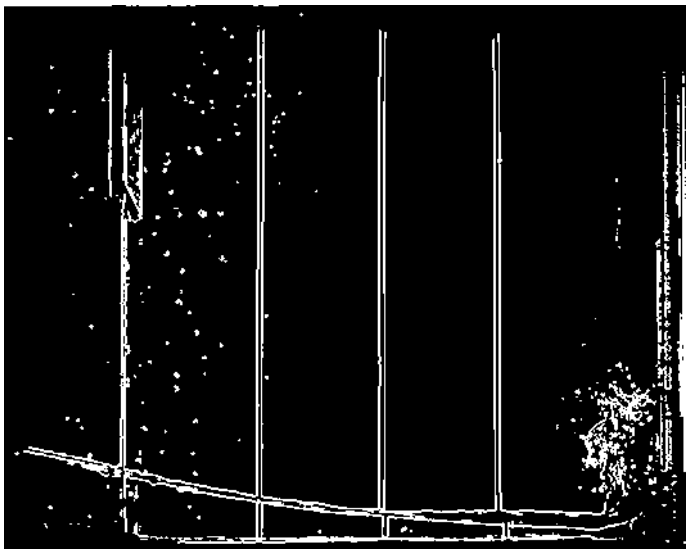

Figure C.3: Edge thickness dilated

The SHT uses the parametric representation of a line:

$$\rho = x\cos(\theta) + y\sin(\theta) \tag{C.1}$$

The variable ρ is the distance from the origin to the line along a vector perpendicular to the line. θ is the angle of the perpendicular projection from the origin to the line measured in degrees clockwise from the positive x-axis. The range of theta is $90° \leq \theta < 90°$. The angle of the line itself is $\theta + 90°$, also measured clockwise with respect to the positive x-axis.

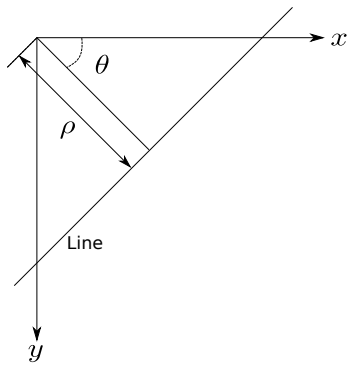

Figure C.4: Hough transform for straight lines

The SHT is a parameter space matrix whose rows and columns correspond to ρ and θ values respectively. The elements in the SHT represent accumulator cells. Initially, the value in each cell is zero. Then, for every non-background point in the image, ρ is calculated for every θ. ρ is rounded off to the nearest allowed row in SHT. That accumulator cell is incremented. At the end of this procedure, a value

of Q in SHT(r,c) means that Q points in the xy-plane lie on the line specified by θ(c) and ρ(r). Peak values in the SHT represent potential lines in the input image. More information about the SHT is referred to JÄHNE [99].

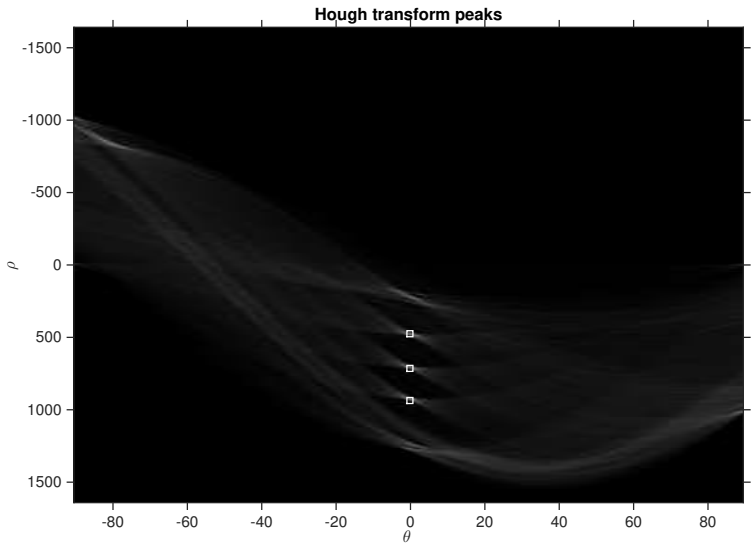

Figure C.5: Hough transform peaks

In Fig. C.5, the white square shows the identified three peaks in SHT, which represent three longest lines dectected as shown in Fig. C.6.

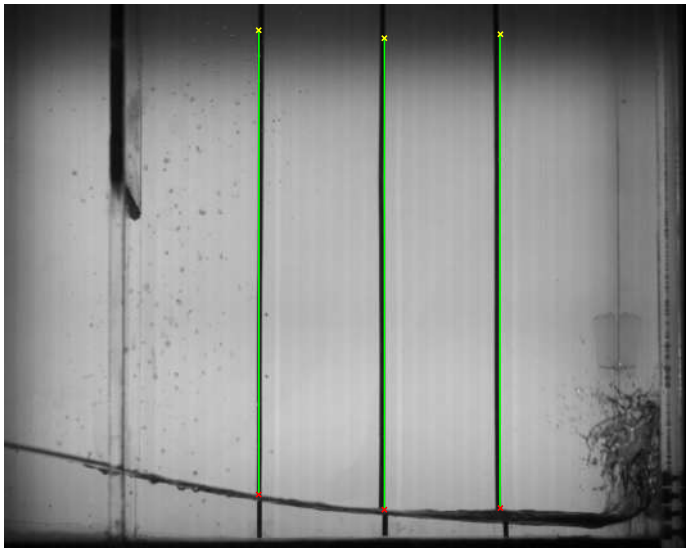

Figure C.6: Dectected top three longest line

The water level information is carried by the bottom point of these dectected lines. As shown in Fig. C.7, the water level now could be extracted from the distance in pixels between the detected bottom point and the base line. The distance in pixels can finnaly be converted to meter based on camera calibration.

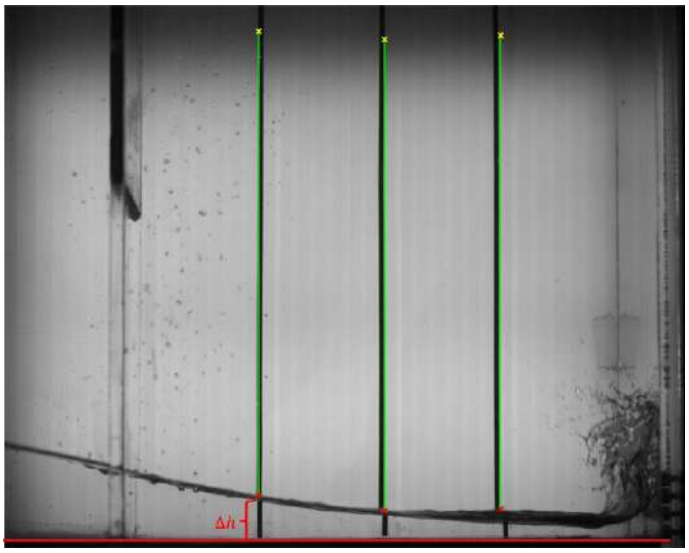

Figure C.7: Calculate the detected water level

Appendix D

Uncertainty Analysis of BIV

D.1 Uncertainty analysis of BIV

The uncertainty analysis for a PIV system is referred to ITTC Recommended Procedures and Guidelines (PARK *et al.* [20]). Since BIV is a direct adoption of the PIV technique, the uncertainty analysis for a BIV system could be similarly evaluated.

Following the ISO *Evaluation of measurement data Guide to the expression of uncertainty in measurement* (BIPM *et al.* [101]), if an experimental result is given by the data reduction equation $f = f(x_1, x_2, \cdots, x_N)$, the combined standard uncertainty of the estimate f is denoted by $u_c(f)$ and given as,

$$u_f^2 = \sum_{i=1}^{N} (\frac{\partial f}{\partial x_i})^2 u(x_i)^2 \tag{D.1}$$

where x_i is the independent error source of f and $u(x_i)$ is the uncertainty of x_i.

The principle of the BIV measurement on flow velocity u could be described as,

$$u = \alpha \frac{\Delta X}{\Delta t} + \delta u \tag{D.2}$$

where, α is a magnification factor between physical coordinates (in mm) and image coordinates (in pixel) and α can be identified through the calibration procedure; ΔX is the displacement of particle in images (in pixel); Δt is time interval and δu represents the uncertainty factors of flow visualization. From Eq. (D.2), to evaluate the uncertainty on u, the uncertainty on the α, ΔX, Δt, and δu should be evaluated first.

The calibration was done by using a calibration board. The distance of the reference point l_r and its distance on the image plane L_r were used to determine the magnification factor, α, as

$$\alpha = \frac{l_r}{L_r} cos\theta \approx \frac{l_r}{L_r}(1 - \frac{\theta^2}{2}) \tag{D.3}$$

where θ is a small angle between the object plane and the calibration board.

Following PARK *et al.* [20], the error sources and its uncertainty analysis on θ are summarized in Table D.1. The distance of the reference points (L_r) were measured on the image plane. If the position of the reference points were detected from a single point of image, the uncertainty will be 0.5 pixel. Since the distance is determined by two points, the total amount of uncertainty will be $0.5\sqrt{2} = 0.7$ pixel. The uncertainties of the physical length of the reference points affect the accuracy of the magnification factor. Using a well-controlled calibration board, the uncertainty on l_r can be assumed as 20 μm. The image could be distorted by the aberration of lenses. The distortion of the image affects the error of magnification factor. The distortion of the image could assumed be as 0.5% of L_r. The uncertainty band caused by the accuracy of CCD is usually small, and it can be neglected. The position of the calibration board and the object plane could be different and this difference is assumed less than 0.5 mm. Ideally, the calibration board should be parallel to the object plane for visualization. The error due to non-parallel could assumed to be 2 degree.

Table D.1: Evaluate the uncertainty on α

Error Sources	$u(x_i)$	$\frac{\partial f}{\partial x_i}$
L_r in pixel	$0.5\sqrt{2} = 0.7$ pixel	$\frac{\partial \alpha}{\partial L_r} = -\frac{l_r}{L_r^2}$
l_r in mm	about 20 μm	$\frac{\partial \alpha}{\partial l_r} = \frac{1}{L_r}$
distortion by lens	$\leq 0.5\% L_r$	$\frac{\partial \alpha}{\partial L_r} = -\frac{l_r}{L_r^2}$
distortion by CCD	neglected	$\frac{\partial \alpha}{\partial L_r}$
Board position l_t	0.5 mm	$\frac{\partial \alpha}{\partial l_t} = -\frac{l_r}{L_r l_t}$
Parallel board θ	$2^\circ = 0.035\ rad$	$\frac{\partial \alpha}{\partial \theta} = -\frac{l_r}{L_r}\theta$
combined uncertainty	$u_c(\alpha)$	

The measurement position and time are defined by Eq. D.4 and D.5. Eq. D.4, X_0 indicates the location of origin on the image plane, and X_s and X_e show the starting and ending position of correlation area. The physical location can be obtained by transferring it with magnification factor α.

$$x = \alpha(\frac{X_s + X_e}{2} - X_0) \tag{D.4}$$

$$t = \frac{t_s + t_e}{2} \tag{D.5}$$

The error sources and the uncertainty analysis on image displacement x are summarized in Table D.2. The spatial and temporal fluctuation of light power could affect on the detection of particle image position directly. This error is assumed to be 1/10 of particle diameter d_p. The amount of error from camera distortion could be estimated as 0.0056 pixels. The normal or perpendicular view angle to the illumination plane could affect the uncertainty of the displacement. The angle could be estimated as 2 degree. In the pixel unit analysis, mis-matching of pair particle images could happen and its uncertainty could be estimated as 0.2 pixel. The uncertainties of sub-pixel analysis depend on many factors such as the diameter of tracer particle, noise level of the image, and particle concentration. Here, it is estimated as 0.03 pixel.

Table D.2: Evaluate the uncertainty on image displacement ΔX

Error Sources	$u(x_i)$	$\frac{\partial f}{\partial x_i}$
Light power fluctuation	$\frac{1}{10}\sqrt{2}d_p$	$\frac{\partial X}{\partial x} = \frac{1}{\alpha}$
Image distortion by camera	0.0056 pix	$\frac{\partial x}{\partial X} = \alpha$
Normal view angle	$2^\circ = 0.035\ rad$	$\frac{\partial \alpha}{\partial \theta} = -\frac{l_r}{L_r}\theta$
Mis-matching error	0.2 pix	1.0
Sub-pixel analysis	0.03 pix	1.0
combined uncertainty	$u_c(\Delta X)$	

The error sources and the uncertainty analysis on δu are summarized in Table D.3. The error source of particle trajectory is related to the velocity lag. The error from velocity lag is assumed to be 0.01% of the total velocity. The error sources of three-dimensional effects come from the perspective of out-of-plane velocity component and assumed as 1.0% of the flow velocity.

Table D.3: Evaluate the uncertainty on δu

Error Sources	$u(x_i)$	$\frac{\partial f}{\partial x_i}$
Particle trajectory	$0.01\%u$	1.0
3-D effects	$1\%utan\beta$	1.0
combined uncertainty	$u_c(\delta u)$	

The error sources and the uncertainty analysis on Δt are summarized in Table D.4. The fluctuation of pulse time could be an error source of measurement from the time series analysis. The uncertainty for it could be 5 ns.

From the calculated combined uncertainty in Table D.1 to Table D.4 and with Eq. D.2, the uncertainty on u are summarized in Table D.5.

Table D.4: Evaluate the uncertainty on Δt

Error Sources	$u(x_i)$	$\frac{\partial f}{\partial x_i}$
pulse timing accuracy	5 ns	1.0
combined uncertainty	$u_c(\Delta t)$	

Table D.5: Evaluate the uncertainty on u

Error Sources	$u(x_i)$	$\frac{\partial f}{\partial x_i}$
α	$u_c(\alpha)$	$\frac{\Delta X}{\Delta t}$
ΔX	$u_c(\Delta X)$	$\frac{\alpha}{\Delta t}$
Δt	$u_c(\Delta t)$	$-\frac{\alpha \Delta X}{2\Delta t^2}$
δu	$u_c(\delta u)$	1.0
combined uncertainty	$u_c(u)$	

D.1.1 Optimize magnification factor

To use the BIV technique, one important consideration is to match the size of a typical particle image diameter d_τ with the resolution of recording medium. The resolution elements of a video graphic device are the pixel elements and the resolution is characterized by their spacing. These pixel elements can be considered as discrete sampling points in the image. If particle image diameter is too small, the image is under-sampled according to Nyquists criterion and information might be lost. As demonstrated in RAFFEL *et al.* [16], the so-called "peak locking" effects is introduced when the particle image diameter is too small, which means the bias error of the system is increased due to under-sampling. On the other hand, if the image is too large, the system wastes the information capacity by sampling more often than needed to specify the image.

ADRIAN [79] gived one formulation to optimize the magnification factor by estimating the depth of field (DOF). Noticing the formulation for calculating DOF in ADRIAN [79] is different as the formulation used in RYU *et al.* [15]. To avoid the mis-understanding in DOF, here we introduce a new way to optimize the magnification factor more directly without calculating the DOF.

According to RAFFEL *et al.* [16], if lens aberrations can be neglected the particle image diameter can be estimated as,

$$d_\tau = \sqrt{(Md_p)^2 + d_{diff}^2} \tag{D.6}$$

where d_p is the particle diameter and d_{diff} is diffraction limited imaging diameter

which could be estimated as

$$d_{diff} = 2.44(1 + M)f^{\#}\lambda \tag{D.7}$$

where $f^{\#}$ is the so-called f-number, defined as the ratio of the focal length of a camera lens to the diameter of the aperture and λ is the wavelength of the light source.

Assuming d_τ can be approximately by,

$$d_\tau = c_r d_r \tag{D.8}$$

where c_r donates the number of pixels per particle diameter and d_r donates the size of one pixel. According to ADRIAN [79], the bias error of discrete sampling may be considered negligible if c_r is greater than one to three pixels per diameter, for reference we shall take $c_r = 3$.

By combining Eq. (D.6), Eq. (D.7) and Eq. (D.8), it follows,

$$(Md_p)^2 + (2.44f^{\#}\lambda)^2(1 + M)^2 = (c_r d_r)^2 \tag{D.9}$$

Solving Eq. (D.9) and ignoring the negative solution yields the optimized magnification factor,

$$M_{opt} = \frac{-(2.44f^{\#}\lambda)^2 + \sqrt{((2.44f^{\#}\lambda)^2 + d_p^2)(c_r d_r)^2 - (2.44f^{\#}\lambda)^2 d_p^2}}{(2.44f^{\#}\lambda)^2 + d_p^2} \tag{D.10}$$

It could be seen that $f^{\#}$ and d_r are constants related to camera properties and λ is referred to light source. Once the camera and the light source are selected for the system, the mean particle diameter would be the main consideration for optimizing the magnification factor.